

**Some pages of this thesis may have been removed for copyright restrictions.**

If you have discovered material in Aston Research Explorer which is unlawful e.g. breaches copyright, (either yours or that of a third party) or any other law, including but not limited to those relating to patent, trademark, confidentiality, data protection, obscenity, defamation, libel, then please read our [Takedown policy](#) and contact the service immediately (openaccess@aston.ac.uk)

**IMMUNOLOGICAL SYNAPSE: A MATHEMATICAL  
MODEL OF THE BOND FORMATION PROCESS**

**Mathematical modelling of the immature synapse**

**DANIEL ROBERT BUSH**

Doctor of Philosophy (by Research)

ASTON UNIVERSITY

Aug 2015

©Daniel Robert Bush, 2015

Daniel Robert Bush asserts his moral right to be identified as the author of this thesis.

This copy of the thesis has been supplied on condition that anyone who consults it is understood to recognise that its copyright rests with its author and that no quotation from the thesis and no information derived from it may be published without appropriate permission or acknowledgement.

# IMMUNOLOGICAL SYNAPSE: A MATHEMATICAL MODEL OF THE BOND FORMATION PROCESS

## Mathematical modelling of the immature synapse

Daniel Robert Bush

Doctor of Philosophy (by Research), 2015

### Thesis Summary

The cell:cell bond between an immune cell and an antigen presenting cell is a necessary event in the activation of the adaptive immune response. At the juncture between the cells, cell surface molecules on the opposing cells form non-covalent bonds and a distinct patterning is observed that is termed the immunological synapse. An important binding molecule in the synapse is the T-cell receptor (TCR), that is responsible for antigen recognition through its binding with a major-histocompatibility complex with bound peptide (pMHC). This bond leads to intracellular signalling events that culminate in the activation of the T-cell, and ultimately leads to the expression of the immune effector function. The temporal analysis of the TCR bonds during the formation of the immunological synapse presents a problem to biologists, due to the spatio-temporal scales (nanometers and picoseconds) that compare with experimental uncertainty limits.

In this study, a linear stochastic model, derived from a nonlinear model of the synapse, is used to analyse the temporal dynamics of the bond attachments for the TCR. Mathematical analysis and numerical methods are employed to analyse the qualitative dynamics of the non-equilibrium membrane dynamics, with the specific aim of calculating the average persistence time for the TCR:pMHC bond. A single-threshold method, that has been previously used to successfully calculate the TCR:pMHC contact path sizes in the synapse, is applied to produce results for the average contact times of the TCR:pMHC bonds. This method is extended through the development of a two-threshold method, that produces results suggesting the average time persistence for the TCR:pMHC bond is in the order of 2-4 seconds, values that agree with experimental evidence for TCR signalling. The study reveals two distinct scaling regimes in the time persistent survival probability density profile of these bonds, one dominated by thermal fluctuations and the other associated with the TCR signalling. Analysis of the thermal fluctuation regime reveals a minimal contribution to the average time persistence calculation, that has an important biological implication when comparing the probabilistic models to experimental evidence. In cases where only a few statistics can be gathered from experimental conditions, the results are unlikely to match the probabilistic predictions. The results also identify a rescaling relationship between the thermal noise and the bond length, suggesting a recalibration of the experimental conditions, to adhere to this scaling relationship, will enable biologists to identify the start of the signalling regime for previously unobserved receptor:ligand bonds. Also, the regime associated with TCR signalling exhibits a universal decay rate for the persistence probability, that is independent of the bond length.

Keywords: TCR bond persistence, stochastic differential equation modelling, survival probability scaling exponent

# Publications

- Bush, D. R. and Chattopadhyay, A. K. (2014). Contact time periods in immunological synapse. *Physical Review E*, 90 (4), 042706. doi: 10.1103.PhysRevE.90.042706
- Bush, D. R. and Chattopadhyay, A. K. (2015). Temporal dynamics in immunological synapse: Role of thermal fluctuations in signaling. *Physical Review E*, 92, 012706. doi: 10.1103.PhysRevE.92.012706
- Bush, D. R. and Chattopadhyay, A. K. (2016). Asymptotic analysis of the immunological synapse dynamics: A saddle point method based approach. *Manuscript under preparation*.

# Acknowledgements

First and foremost, I'd like to thank Amit Chattopadhyay for providing me the opportunity to undertake this study. His enthusiasm for applied physics, and research in general, was evident from our first meeting and continued throughout the entire course. Amit was always available to discuss ideas and proved an exceptional driving force when my energy levels dropped.

Secondly, I would like to thank Alex Brulo. He ensured the cluster servers, required for the numerical simulations, were maintained and readily available throughout the course of this study. His knowledge and support have helped immeasurably toward the development of a codebase, that I hope will be of use to others in future academic work.

I'd also like to thank Ben Toucher, Jan Duracz, Richard Jones, Diar Nasiev, Raje Matam, Vladimir Mezentsev and Harry Goldingay, for their insightful discussions and words of encouragement. They helped maintain my momentum and ensured my visits to the university were enjoyable. And to the many members of the wider NCRG department, especially David Saad and David Lowe, it has been a joy to pass through this vibrant research department.

Also, my sincere thanks goes to my friends and family for their support. All have endured my unintelligible ramblings at some point, and I thank you for your patience and support. Especially, Teresa Bush and Leonard Bush (mum and dad), who have been a trusted sounding board, providing measured advice throughout my studies, indeed throughout my life. I can't thank you enough for your support and encouragement.

Finally, I'd like to thank Liza. The addition of three children during this study has provided many challenges. Your perseverance in the face of complicated pregnancies, screaming babies and sleepless nights has been amazing. Thank you for helping me see it through to fruition.

And to Lelia, Ebony and Otto, I couldn't have asked for better distractions.

# Contents

<b>1</b>	<b>Introduction</b>	<b>1</b>
1.1	The Human Immune System . . . . .	1
1.1.1	The Innate System . . . . .	2
1.1.2	The Adaptive System . . . . .	2
1.2	The Immunological Synapse . . . . .	5
1.2.1	Cell Surface Molecules . . . . .	5
1.2.2	Synapse Formation . . . . .	8
1.2.3	Intracellular Signalling . . . . .	12
1.2.4	TCR Triggering Models . . . . .	14
1.3	Mathematical Modelling of the Immunological Synapse . . . . .	15
1.4	Research Questions . . . . .	17
1.5	Thesis Organisation . . . . .	18
<b>2</b>	<b>Membrane Model</b>	<b>19</b>
2.1	Synapse Assembly Model . . . . .	19
2.2	Steady State Linearized Membrane Separation Distance Model . . . . .	24
2.2.1	Chattopadhyay and Burroughs Model . . . . .	25
<b>3</b>	<b>Theoretical Methods</b>	<b>27</b>
3.1	Analytical Methods . . . . .	27
3.1.1	Integral Equation Solution of the Langevin Equation . . . . .	28
3.1.2	Fokker-Planck Equation for the Steady State Probability Distribution . . . . .	29
3.1.3	Temporal Two Point Correlation Function . . . . .	30
3.1.4	Scaling Approach . . . . .	31
3.1.5	Independent Interval Approximation . . . . .	33
3.1.6	Single-Threshold Model . . . . .	34
3.2	Numerical Methods . . . . .	36
3.2.1	Discretisation . . . . .	37
3.2.2	Finite Difference Approximations and Time Evolution . . . . .	38

3.2.3	Numerical Simulation of the Single-Threshold Model . . . . .	40
<b>4</b>	<b>Asymptotic Analysis Applied to the Temporal Correlation Function</b>	<b>45</b>
4.1	Laplace’s Method . . . . .	45
4.2	Saddle Point Method . . . . .	47
<b>5</b>	<b>Contact Time Periods in Immunological Synapse</b>	<b>54</b>
5.1	Introduction . . . . .	54
5.2	The Two-Threshold Model . . . . .	55
5.3	Average Close Contact Time Persistence . . . . .	57
5.4	Persistence Probability Density of Close Contact Time . . . . .	60
5.5	Discussion . . . . .	61
<b>6</b>	<b>Temporal dynamics in immunological synapse: Role of thermal fluctuations in signalling</b>	<b>63</b>
6.1	Close Contact Survival Statistics . . . . .	64
6.2	The Small- $\tau$ Phase: The “Thermal Fluctuations” regime . . . . .	66
6.3	The Large- $\tau$ Phase: The “Signalling” regime . . . . .	69
6.4	Extremal Value Statistics . . . . .	73
6.5	Discussion . . . . .	75
<b>7</b>	<b>Conclusion and Discussion</b>	<b>76</b>
7.1	Average persistence time for the TCR:pMHC bond . . . . .	77
7.2	The effect of thermal fluctuations on the average persistence time for the TCR:pMHC bond . . . . .	78
7.3	Future Work . . . . .	78
<b>A</b>	<b>Linearised Steady State Model Derivation</b>	<b>81</b>
<b>B</b>	<b>Integral Equation Solution to the Langevin Equation</b>	<b>85</b>
<b>C</b>	<b>Temporal Correlation Function</b>	<b>88</b>
C.1	Temporal Correlation of the Membrane Separation Distance . . . . .	88
C.2	Spatial Langevin Force in the $k$ -space . . . . .	91
<b>D</b>	<b>Residue Theorem “Null” Solution of the Temporal Correlation Function</b>	<b>92</b>
<b>E</b>	<b>Clipped Correlator For a Gaussian Stationary Process</b>	<b>95</b>
E.1	Calculate Normalisation Constant . . . . .	96
E.2	Clipped Correlator . . . . .	97

<b>F</b>	<b>Clipped Correlator Derivation</b>	<b>99</b>
F.1	Calculate Normalisation Constant . . . . .	100
F.2	Clipped Correlator . . . . .	100
F.2.1	$\frac{\partial A(\tau)}{\partial \tau}$ Calculation . . . . .	101
<b>G</b>	<b>Steady State Fokker-Planck Equation</b>	<b>104</b>
G.1	Langevin Equation to Steady State Fokker-Planck Equation . . . . .	104
G.2	Relation to $P(z(\mathbf{x}, t), \mathbf{x}, t)$ . . . . .	106

# Acronyms

**AP-1** activator protein-1. 13

**APC** antigen presenting cell. xii, xiii, 1–3, 5, 6, 8, 17, 18, 22, 55

**B-cell** B lymphocyte. 2–5, 8

**BCR** B-cell antigen receptor. 2, 3

**Ca<sup>2+</sup>** calcium. 9, 12–14, 20, 61

**CD2** cluster of differentiation 2. 7, 9, 13, 23, 80

**CD28** cluster of differentiation 28. 5, 7, 9–11, 13, 80

**CD28:CD80** the bond formed between CD28 and CD80 molecules. 13–15, 21

**CD2:CD48** the bond formed between CD2 and CD48 molecules. 14

**CD2:CD58** the bond formed between CD2 and CD58 molecules. 21

**CD3** CD3. 7

**CD4** cluster of differentiation 4. 3, 7, 9, 12, 80

**CD43** leukosialin. 5, 7, 9–11, 80

**CD45** leucocyte common antigen. 5, 7, 9, 10, 12, 14, 80

**CD48** CD48. 14

**CD58** LFA-3. 5

**CD8** cluster of differentiation 8. 3, 7, 80

**CD80** B7-1. 7

**CD86** B7-2. 7

**CRAC** Ca<sup>2+</sup>-release-activated Ca<sup>2+</sup>. 12, 20

**cSMAC** central supramolecular activation cluster. 9–14, 21, 22, 54, 55, 80

**DAG** diacyl-glycerol. 12

**DC** dendritic cell. 2, 3, 5, 8, 10

**DNA** deoxyribonucleic acid. 3, 13

**dSMAC** distal supramolecular activation cluster. 9, 11

**ER** endoplasmic reticulum. 8

**ERM** ezrin-radixin-moesin. 11

**Fyn** protein tyrosine kinase. 12

**Grb2** growth factor rector-bound protein 2. 12

**HIV** human immunodeficiency virus. 7

**ICAM-1** intercellular adhesion molecule-1. 5, 7, 8, 19

**IL-2** interleukin 2. 10, 12, 13

**IP3** inositol triphosphate. 12

**IS** immunological synapse. xiii, 5, 7–11, 14, 17, 19, 23, 26, 27, 29, 32, 38, 47, 54–56, 77

**ITAM** immunoreceptor tyrosine-based activation motif. 12, 13

**KS** Kinetic Segregation. 14, 17

**LAT** linker for activated T cells. 12, 13

**Lck** lymphoid cell kinase. 12–14

**LFA-1** lymphocyte function-associated antigen 1. 5, 7–11, 14, 15, 19, 23

**LFA-1:ICAM-1** the bond formed between the LFA-1 and ICAM-1 molecules. 8, 9, 14, 19–21, 23, 25, 55, 58, 61, 74, 76–78, 80

**MAPK** mitogen-activated protein kinase. 12

**MHC** major histocompatibility complex. 3, 7, 8, 15, 23

**MTOC** microtubule organising centre. 5, 9

**NFAT** nuclear factor of activated T-cells. 13

**PKC $\theta$**  protein kinase C- $\theta$ . 8, 9, 13

**PLC $\gamma$ 1** phospholipase C  $\gamma$  1. 12

**pMHC** major histocompatibility complex with bound antigenic peptide. 5, 7, 12, 14, 15, 19–21, 54, 55

**pSMAC** peripheral supramolecular activation cluster. 9–14, 23, 25, 54, 55, 77, 80

**PTPase** phosphotyrosine phosphatase. 7

**Rap1** Rap1. 13

**SA** synapse assembly. 15–17, 19, 20, 22–25, 79, 80

**self-pMHC** major histocompatibility complex with bound self-peptide. 80

**SLP-76** SH2-domain-containing leukocyte-specific phosphoprotein of 76 kDa. 12

**SMAC** supramolecular activation cluster. 9, 13, 14

**T<sub>Cyt</sub>-cell** cytotoxic T-Cell. 3–5, 7

**T<sub>H</sub>-cell** helper T-Cell. xiii, 3–7

**T-cell** T lymphocyte. xii, 1–5, 7, 8, 10–15, 17–19, 22, 23, 55, 70

**TCR** T-cell antigen receptor. v, xiii, 3, 5, 7–15, 17, 19–23, 25, 54, 55, 77, 79, 80

**TCR:pMHC** the bond formed between the TCR and pMHC molecules. vi, 7–9, 14–17, 19, 21–23, 25, 34, 55, 58, 61, 63, 64, 70, 74, 76–80

**WASP** Wiscott Aldrich Syndrome protein. 12, 13

**ZAP-70**  $\zeta$ -associated protein of 70 kDa. 12, 13

# List of Tables

1.1	Membrane spanning molecules on the T-cell. . . . .	7
1.2	Membrane spanning molecules on an APC. . . . .	8
1.3	Biological measurements for intracellular signalling Src kinase phosphorylation events. . . . .	13
2.1	Synapse Assembly membrane model variables. . . . .	20
2.2	Steady state membrane separation distance model parameters. . . . .	25
6.1	Linear fit parameters for $\theta_S$ . . . . .	68
6.2	First passage probability frequencies for transient bonding. . . . .	74

# List of Figures

1.1	T <sub>H</sub> -cell and APC cell surface molecules. . . . .	6
1.2	Schematic of bonds formed in the synaptic junction. . . . .	6
1.3	Cell surface molecule movements during IS formation: early visualisations. . .	9
1.4	The mature IS formation highlighting the spatial distribution and movements of TCR microclusters over time. . . . .	11
3.1	The large time Gaussian stationary process temporal correlation length. . . .	32
3.2	$\langle \tau \rangle$ plotted against $\Delta$ . . . . .	37
3.3	The simulated time evolution of the local membrane separation distance. . . .	40
3.4	The probability density of the local membrane separation distance, extracted from numerical simulations using three different thermal noise strengths. . . .	41
3.5	The simulated solution for the separation distance and the time persistence definition . . . . .	43
4.1	Integral and asymptotic solution comparison for the temporal correlation function as $\tau \rightarrow \infty$ . . . . .	48
4.2	Log comparison of the integral and asymptotic temporal correlation functions. . . . .	48
5.1	Schematic for the identification of the different time persistence domains for the fluctuating membrane in the IS, using the two-threshold model. . . . .	56
5.2	Time persistence above the $\Delta_i$ threshold, $\langle \tau^+ \rangle$ vs $\Delta_i$ . . . . .	59
5.3	Time persistence between two thresholds, $\langle \tau_\delta \rangle$ vs $\delta$ . . . . .	60
5.4	Probability density, $p(\tau)$ between two thresholds. . . . .	61
5.5	Comparison of the probability density for $p(\tau_{12})$ and $p(\tau_{11})$ as $\delta$ varies. . . . .	62
6.1	Average number of cases per system run for $d = 2 + 1$ . . . . .	64
6.2	The probability density distribution, $W_\Delta(\tau)$ , for the time persistence above $\Delta = 0$ nm. . . . .	65
6.3	Log:Log plot for the survival probability $P_{\Delta(=0)}(\tau)$ . . . . .	66
6.4	The small $\tau$ regime time exponent. . . . .	67
6.5	The $\alpha$ dependence on $D$ . . . . .	68

6.6	Schematic illustration of the time-dependent rescaling used in the large $\tau$ regime.	71
6.7	The rescaling functions, $\Omega$ and $\Psi$ , along with the rescaled large $\tau$ regime. . .	72
6.8	Contribution of the extremal values to the average time persistence calculation.	74

# Chapter 1

## Introduction

This chapter focuses on a core biological description of the key components of the human immune system, with a detailed description of the immunological synapse that forms during an immune response. Studies using mathematical modelling techniques to describe the different components of the immunological synapse are reviewed, leading to the identification of the research questions addressed in this thesis. The layout of this chapter is as follows: section 1.1 describes the human immune system, introducing the cells belonging to the adaptive immune system, along with a discussion of their roles in coordinating immune functions during an immune response. In section 1.2, the immunological synapse that forms during various stages of the adaptive immune response is described, specifically concentrating on the synapse developed between a T lymphocyte (T-cell) and an antigen presenting cell (APC). Some of the important cell surface molecules involved in the formation of the immunological synapse are introduced, along with details concerning the formation, function and activation models for the synapse. In section 1.3, the mathematical modelling undertakings used to analyse the dynamics involved at the synaptic junction are outlined. Analysis of this literature leads to the research questions defined in section 1.4 and finally, section 1.5 shows the organisation of the remainder of the thesis.

### 1.1 The Human Immune System

The human immune system has evolved to provide a complex defence system against a wide range of pathogens, both bacterial and viral. Bacterial pathogens are single-celled organisms that are able to reproduce on their own, often infecting areas through attachment to host cell surfaces. Viral pathogens are much smaller and are not able to reproduce on their own, they require entry to a host cell, where they appropriate the internal organelles in order to reproduce, often killing the host cell in the process. The immune system is comprised of three different components (subsystems) that compliment each other during an immune

response, these include a physical barrier, the innate system and the adaptive system. The physical barrier is the initial gateway of interaction for a foreign pathogen, in the form of skin tissue and the mucousal lining. When the physical barrier is compromised, cells belonging to the innate system in the surrounding tissue are the first to react, followed by cells from the adaptive system. The cellular interactions between these different cell types is central to this study, so a brief overview of the innate and adaptive systems is given in the subsections below.

### **1.1.1 The Innate System**

Cells of the innate system include neutrophils, eosinophils, basophils, mast cells and macrophages. These cells constantly migrate throughout the blood and host tissue, enabling the capability to produce a timely response to pathogenic material, through direct contact. In general, this involves phagocytosis, where the foreign body is engulfed by the immune cell membrane. The membrane folds around the pathogen to form an intracellular pocket, that detaches from the main membrane layer, free to migrate through the cytosol as an intracellular vesicle. Once the pathogen is held within the vesicle, the threat to surrounding healthy cells is eliminated (Murphy, Travers and Walport, 2008). The innate cells are capable of responding to a broad range of pathogens, but the response is non-specific and does not provide lasting immunity. Upon ingestion of the pathogenic substance, the immune cell secretes cytokines and chemokines that create an inflammatory response, effectively setting up a gradient to attract additional immune cells to the site of infection. The innate system also includes dendritic cells (DCs), that form a link between the innate and adaptive immune systems. These cells are a type of professional APC, designed to present antigenic material to the adaptive immune cells. This is accomplished through the ingestion and decomposition of the antigen into small peptide fragments, enabling external presentation of these fragments on the DC surface. Following uptake of the antigenic material, mature DCs migrate from the site of infection, through lymphatic vessels, toward the lymph nodes. Here, they mix with a constant stream of lymphocytes, circulating the lymphatic system. The fragments on the DC surface come in to direct contact with the antigen recognition receptors diffusing throughout the immune cell surface. Positive recognition by the antigen recognition receptor is one of the initiating event toward an immune response from the adaptive system.

### **1.1.2 The Adaptive System**

Two important cells of the adaptive system are the T-cell and B lymphocyte (B-cell), with both cells beginning life in the bone marrow. B-cells remain in the in the bone marrow, where they continue to evolve in to mature B-cells that exhibit antigen recognition receptors,

the B-cell antigen receptor (BCR), on the cell surface. Once they have matured, the B-cell migrates to the peripheral lymph organs, where they begin to circulate within the lymphatic system. B-cells use BCRs to recognise and bind to antigens on infected cells and when the complimentary antigen is identified they proliferate and secrete antibodies, with some of the cells evolving in to memory cells that are capable of producing a rapid response upon subsequent encounters with antigens (Murphy, Travers and Walport, 2008).

Although T-cells also begin life in the bone marrow, at an early stage of their development they migrate to the thymus where they mature through a series of positive and negative selection processes. During this maturation process, the T-cells differentiate in to helper T-Cells ( $T_H$ -cells) or cytotoxic T-Cells ( $T_{Cyt}$ -cells). These two cell types express a different distinct coreceptor molecule on their cell surface. The  $T_H$ -cells are identified through the presence of the cluster of differentiation 4 (CD4) coreceptor molecule, whereas  $T_{Cyt}$ -cells express the cluster of differentiation 8 (CD8) coreceptor molecule. Both coreceptor molecules are present on the immature T-cell, but the process of positive and negative selection ensures the presence of only one of these coreceptor molecules on the mature T-cell.

Like the B-cell, the T-cell bears an antigen recognition molecule on the cell surface, the T-cell antigen receptor (TCR). The TCR has an  $\alpha$  and  $\beta$  chain that are constructed using a random recombination of certain sections of the deoxyribonucleic acid (DNA) sequence, denoted V, J and D. This random recombination is capable of producing somewhere in the order of  $\sim 10^{18}$  distinct receptors, with each T-cell bearing a set of identical antigen receptors (approx. 30,000 per cell), that diffuse freely throughout the cell surface (Murphy, Travers and Walport, 2008).

The TCR recognises antigenic material presented in the cleft of molecules synthesised from the major histocompatibility complex (MHC) gene, that are expressed on the cell surface of an APC. The two chains of the TCR contain binding sites, determined by the random recombination of gene segments, that describe the specificity of the receptor. When the receptor comes in to close contact with the MHC molecule on the APC, binding occurs when the specific sites on the TCR match the structure of the antigenic material held in the cleft of the MHC molecule.

There are two types of MHC molecules called class I and class II molecules. The TCRs on  $T_H$ -cells bind exclusively to the MHC class II molecules, while the  $T_{Cyt}$ -cell binds exclusively to the MHC class I molecules (Murphy, Travers and Walport, 2008). Once maturation is complete, single positive T-cells migrate toward the lymph organs and begin circulating within the lymphatic system. As the T-cells migrate within the lymphatic system they come in to contact with the DCs expressing antigenic material on their cell surface. Upon successful recognition and binding of their specific antigenic peptide on a DC, the T-cell rapidly proliferates and differentiates into antigen-specific clones that express the same TCR

specificity. The new cells may be direct clones that increase the immediate immune response, suppressor T-cells that inhibit the immune response, or memory T-cells that provide a rapid response to repeat infections (Murphy, Travers and Walport, 2008).

In addition to the difference in coreceptor molecules, the  $T_H$ -cells and the  $T_{Cyt}$ -cell produce different immune function responses. The  $T_H$ -cells work in conjunction with cells from the innate system and B-cells. Interaction between macrophages and activated  $T_H$ -cells cause the macrophage to degrade pathogenic material stored in intracellular vesicles, disposing of the degraded material in to the cytosol, an important mechanism for combating leprosy. Activated  $T_H$ -cells may also engage with B-cells, inducing antibody production and secretion by the B-cell. The secreted antibodies are then able to bind to the specific antigenic material and neutralise it (Murphy, Travers and Walport, 2008). In contrast, the  $T_{Cyt}$ -cell interacts directly with infected cells and prolonged engagement results in the release of cytotoxic granules on to the infected cell surface, causing cell death through apoptosis. Thus, the adaptive immune system provides a number of functions that both compliment the innate system and directly target infected cells.

Four decades ago, Lipsky and Rosenthal (1975) studied the immune response in guinea pig lymph nodes, leading them to conclude that direct cell contact is required for antigen presentation and recognition. Since then, advances in molecular biology and medical imaging technology have supported this view and now allow the spatial tracking of individual cellular molecules through time, enabling the observation of the molecular interplay during cell to cell contact. Experimental work has been conducted *in vitro* (on lipid bilayers), *in vivo* and *ex vivo* (Day *et al.*, 2003), using a range of imaging techniques such as electro-spectroscopy, fluorescence imaging, interference reflection microscopy, and more recently two-photon microscopy. Antigen receptors, adhesion molecules and co-stimulatory molecules were among the first to be analysed (Norcross, Smith and Shimizu, 1984; Meuer *et al.*, 1984; Springer, Dustin, Kishimoto and Marlin, 1987; Dustin, Sanders, Shaw and Springer, 1987; Selvaraj *et al.*, 1987; Poo, Conrad and Janeway, 1988), then the intracellular signalling pathways were explored (Rosenstein *et al.*, 1991; Shiroo, Goff, Biffen, Shivnan and Alexander, 1992; Valitutti, Müller, Cella, Padovan and Lanzavecchia, 1995; Manjunath, Correa, Ardman and Ardman, 1995; Dustin, Bromley, Kan, Peterson and Unanue, 1997; Dustin *et al.*, 1998; Davis and van der Merwe, 2011). Work through the 1990's culminated in the first images of the molecular spatial patterns formed in the inter-membrane junction during cell to cell contact (Monks *et al.*, 1998; Grakoui *et al.*, 1999). The contact region between the cells was termed the *immunological synapse* and a significant amount of work has been undertaken by numerous labs to explore the synapse under various conditions ever since.

## 1.2 The Immunological Synapse

The immunological synapse (IS) is formed through non-covalent bonds between receptor-ligand pairs across the membrane junction between a T-cell and APC. These bonds form a tight adhesion zone, that maintain cell engagement for periods of hours, facilitating extracellular signalling that can lead to the activation of the immune cell, and ultimately an immune response. The receptor-ligand bonds create patches of membrane that are tightly apposed, with a diameter in the region of  $10\mu\text{m}$  (Grakoui *et al.*, 1999). The IS forms under many scenarios during the immune cell life-cycle, including early T-cell differentiation in the thymus (Bhakta, Oh and Lewis, 2005; Falahati and Leitenberg, 2008), engagement of T-cells with DCs in the lymph nodes (Stoll, Delon, Brotz and Germain, 2002; Zheng *et al.*, 2008; Henrikson *et al.*, 2008), activation of B-cells by  $T_H$ -cells (Poo *et al.*, 1988), homotypic synapses where activated T-cells engage with each other in the lymph nodes (Sabatos *et al.*, 2008) and during a cytotoxic attack directed toward an infected cell by a mature  $T_{Cyt}$ -cell (Kuhn and Poenie, 2002; Stinchcombe, Bossi, Booth and Griffiths, 2001). In it's simplest form, a single T-cell creates a synapse with a single APC. However, cases where multiple APCs are attached to a single  $T_{Cyt}$ -cell have been recorded (Poenie, Kuhn and Combs, 2004) and *in vivo* studies in the lymph nodes have shown multiple T-cells engaged with a single DC (Ingulli, Mondino, Khoruts and Jenkins, 1997). Each type of synapse often has a particular nuance concerning the synapse formation and/or signalling properties, depending on the maturation stage and the surrounding environmental conditions. But, there are many similarities, such as the binding of specific receptor-ligand pairs, the stopping of T-cell migration and the re-orientation of the intracellular organelles (Golgi apparatus, nucleus, microtubule organising centre (MTOC)). In this thesis a single T-cell:APC interaction is considered, as these are more readily studied under laboratory conditions and the mathematical modelling of the single membrane:membrane system is significantly simpler than the multi-membrane:membrane interactions.

### 1.2.1 Cell Surface Molecules

As mentioned above the IS is described by the bonding of a number of receptor-ligand pairs in the intermembrane junction between the cells. Figure 1.1 shows a  $T_H$ -cell and an APC with some of the many cell surface molecules that are implicated in the formation of the IS.

Some of these molecules are functionally related to cell adhesion (lymphocyte function-associated antigen 1 (LFA-1), intercellular adhesion molecule-1 (ICAM-1) and leukosialin (CD43) (Allenspach *et al.*, 2001)), some are necessary for specific antigen recognition (TCR and major histocompatibility complex with bound antigenic peptide (pMHC)), while others form coreceptor pairs capable of intracellular signalling (cluster of differentiation 28 (CD28),

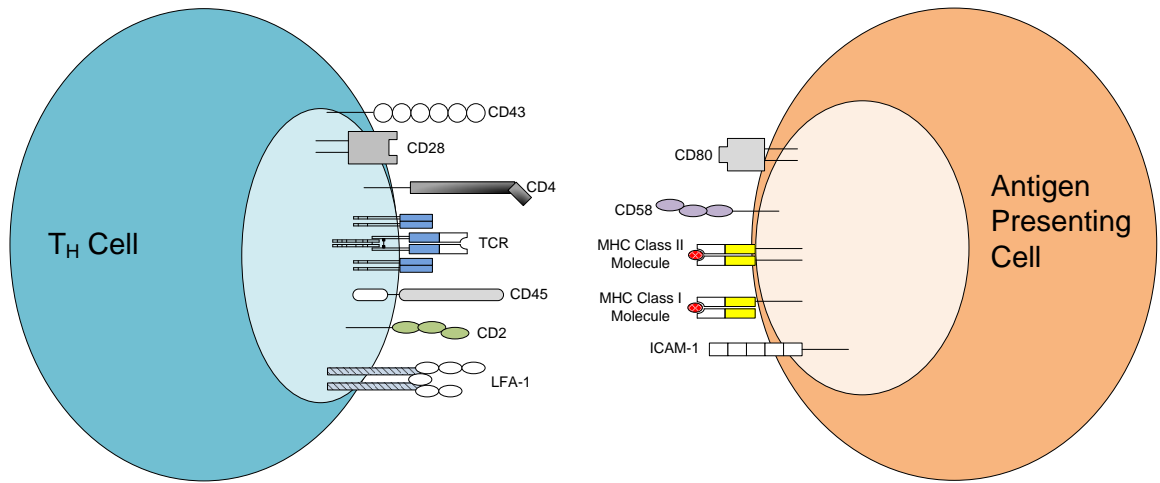


Figure 1.1:  $T_H$ -cell and APC cell surface molecules.

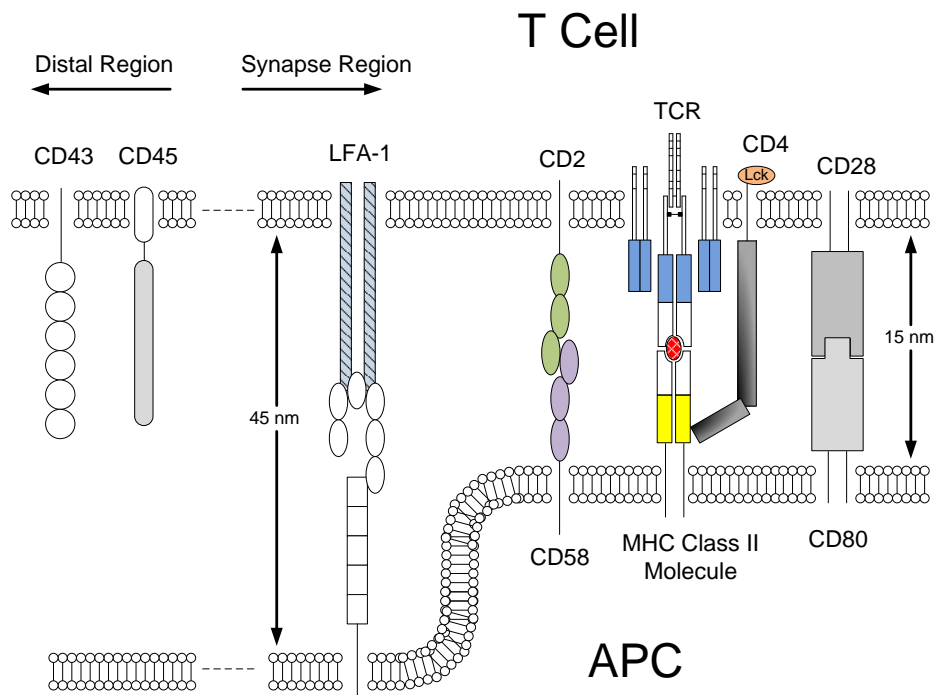


Figure 1.2: Schematic of bonds formed in the synaptic junction.

LFA-3 (CD58), leucocyte common antigen (CD45)), aiding the promotion of T-cell activation. These cell surface molecules are briefly described in tables 1.1 and 1.2.

<b>Molecule</b>	<b>Description</b>
TCR	The antigen recognition receptor is a complex containing two variable polypeptide chains, an $\alpha$ and $\beta$ chain, along with 4 associated CD3 subunits. The $\alpha$ and $\beta$ chains are synthesised through recombination of 3 major gene segments (the $\alpha$ chain only uses two of the segments), capable of producing $\sim 10^{18}$ different TCR configurations, with $\sim 30,000$ identical receptors on the surface of each T-cell (Murphy, Travers and Walport, 2008).
LFA-1	The LFA-1 integrin is an abundant adhesion molecule expressed on all leukocytes (with a few macrophage exceptions), and has a natural ligand in ICAM-1 (Miller <i>et al.</i> , 1995; Springer, Dustin, Kishimoto and Marlin, 1987).
CD2	One of the first processes relating to a receptor-ligand pair to be studied was the interaction between CD2 and LFA-3 (CD48/CD58) (Selvaraj <i>et al.</i> , 1987; Dustin, Sanders, Shaw and Springer, 1987). CD2 is implicated in T-cell activation and proliferation, through intracellular signalling pathways (Meuer <i>et al.</i> , 1984).
CD28	This co-stimulatory molecule is expressed on all T-cells and binds with low affinity to B7-1 (CD80) and B7-2 (CD86) (van der Merwe <i>et al.</i> , 1997).
CD4 (T <sub>H</sub> -cell only)	This coreceptor molecule is expressed on T <sub>H</sub> -cells and has been identified in receptor-mediated virus entry for human immunodeficiency virus (HIV) (Littman, 1996). Extracellular domains on CD4 binds to class II MHC molecules and TCR signalling is increased through this binding (Murphy, Travers and Walport, 2008).
CD8 (T <sub>Cyt</sub> -cell only)	This coreceptor molecule is expressed on T <sub>Cyt</sub> -cell and is only functionally significant when recruited to a TCR:pMHC complex (Wyer <i>et al.</i> , 1999). Extracellular domains on CD8 bind to class I MHC molecules with low affinity and can increase the sensitivity of a T-cell to pMHC one-million fold (Stone and Kranz, 2013).
CD45	CD45 has a large extracellular domain with from 391 to 552 amino acids and a large cytoplasmic domain containing two phosphotyrosine phosphatase (PTPase) (Barclay <i>et al.</i> , 1997). CD45 is able to dephosphorylate and activate Src-family kinases Lck and Fyn (Shiroo <i>et al.</i> , 1992; Johnson, Bromley, Dustin and Thomas, 2000).
CD43	CD43 has a large extracellular domain spanning 45nm and is implicated in inhibiting cell adhesion (Cyster, Shotton and Williams, 1991; Manjunath, Correa, Ardman and Ardman, 1995).

Table 1.1: **Membrane spanning molecules on the T-cell.** The molecules listed have an intracellular portion, an extracellular portion and a section that passes through the lipid bilayer membrane. These transmembrane molecules are capable of sensing extracellular signals and carrying them across the membrane, where they are represented through intracellular signalling cascades.

In the junction between the cells, the cell surface molecules form non-covalent bonds, as shown in figure 1.2. The TCR binds to pMHC class I or class II complex, and has bond length of  $\sim 15$  nm (Barclay *et al.*, 1997). Other coreceptor bonds present in the IS with a similar

Molecule	Description
MHC	There are two types of MHC molecules known as MHC class I and MHC class II molecules. The two different MHC molecules have different pathways to peptide expression at the cell surface. Both types of molecule are formed in the lumen of the endoplasmic reticulum (ER), but the class II molecule leaves the ER in vesicles and the class I molecule remains in the ER. Viral pathogens that enter the cytosol can be broken down in to peptide fragments by proteasomes, after which they are transported to the ER through TAP structures. Once in the ER the peptide fragment can be loaded in the binding cleft of the MHC class I molecule, whereupon the MHC molecule migrates to the cell surface. Peptide loading for the MHC class II molecule is a little different. Pathogens engulfed at the membrane surface reside in endosomes, and these endosomes can fuse with the vesicles containing the MHC class II proteins. Once the MHC class II molecule is in the endosome, it is able to bind peptide fragments from the pathogen contained therein, and following successful loading of the peptide the MHC molecule migrates to the cell surface (Murphy, Travers and Walport, 2008).
ICAM-1	Otherwise known as CD54, ICAM-1 is a natural ligand for LFA-1. The binding affinity of $K_d = 500\text{nm}$ and slow dissociation rate of $0.1\text{s}^{-1}$ suggests a potential mechanism for firm adhesion (Tominaga <i>et al.</i> , 1998).
CD58	Originally called LFA-3, CD58 (CD48 in mouse/rat) is expressed in high quantities on memory T-cells and DCs (Freudenthal and Steinman, 1990). It has been identified as a natural ligand for CD2, with an association rate comparable to that of antibodies to antigens and has a very fast dissociation rate ( $k_{\text{off}} \geq 4\text{s}^{-1}$ ) (Selvaraj <i>et al.</i> , 1987; Davis and van der Merwe, 1996).
CD80	CD80 provides a natural ligand for CD28 and is upregulated upon activation of B-cells (Nabavi <i>et al.</i> , 1992).

Table 1.2: **Membrane spanning molecules on an APC.**

bond length include the CD2:CD58 and the CD28:CD80 bonds (also shown). However, the bond formed between the LFA-1 and ICAM-1 molecules (LFA-1:ICAM-1) is significantly larger at  $\sim 45\text{nm}$ . When two different bond lengths are in close apposition, there is a higher energy cost than compared to the case where the same size bonds are present, as a result of membrane bending. As is subsequently shown, these two length scales play a significant role in the qualitative dynamics during IS formation.

### 1.2.2 Synapse Formation

When a T-cell and an APC engage, an intercellular junction is created containing close contact patches, where the cell surface molecules are able to form bonds with their appropriate conjugates. The first pictures of the dynamic formation of the synapse, between T-cell and a supported membrane containing fluorescent stained APC-like proteins, were produced by Monks *et al.* (1998) and Grakoui *et al.* (1999). They tracked the movements of TCR, LFA-1, talin, and protein kinase C- $\theta$  (PKC $\theta$ ) in the synaptic junction. Immediately following

cell to cell contact, they observed segregation between the shorter bound conjugates (the bond formed between the TCR and pMHC molecules (TCR:pMHC)) and the longer bonds (LFA-1:ICAM-1), creating segregated clusters of TCR and LFA-1 in the synaptic junction. Figure 1.3 shows a diagrammatic representation of the synapse formation over time, where the TCR:pMHC bonds are depicted as green circles and the LFA-1:ICAM-1 bonds are shown as red circles. The left panel shows the initial contact, where the LFA-1:ICAM-1 bonds form



Figure 1.3: **Cell surface molecule movements during IS formation: early visualisations.** During the initial contact period the LFA-1 molecules (red circles) are present at the centre of the contact zone (left panel). The contact area increases over the first 2 minutes, after which a contraction stage occurs. During this period the TCR and LFA-1 molecules mix (centre panel). After  $\sim 10$  mins the synapse begins to stabilise, showing a central accumulation of TCR surrounded by a peripheral accumulation of LFA-1 molecules (right panel) (Monks *et al.*, 1998; Grakoui *et al.*, 1999).

at the centre of the junction with the TCR:pMHC bonds forming in the periphery. During the first 2 minutes after the initial contact, intracellular signalling is detected in the form of calcium ( $\text{Ca}^{2+}$ ) upregulation in the cytosol, the contact area spreads and polarisation of the cytoskeleton and MTOC is observed (Bunnell *et al.*, 2002; Huse *et al.*, 2007; Yokosuka *et al.*, 2008). Over the next 2-10 minutes the contact area spreads and then contracts, during which the two sets of bonds become mixed (centre panel). This phase is termed as the *immature* synapse, characterised by a dynamic reorganisation of the surface proteins, polarisation of the cytoskeleton and the initiation of intracellular signalling. The final phase (right panel) is characterised by the inversion of the TCR and LFA-1 regions, where a stable conjugate is formed and is sustained for periods of several hours. This stable synapse is termed the *mature* synapse and is synonymous with the bullseye pattern observed.

Monks *et al.* (1998) used the term supramolecular activation cluster (SMAC) to describe the spatial pattern, consisting a central supramolecular activation cluster (cSMAC), a peripheral supramolecular activation cluster (pSMAC) and a distal supramolecular activation cluster (dSMAC). The cSMAC has a diameter of 1-3  $\mu\text{m}$  and contains small cell-surface molecules such as TCR,  $\text{PKC}\theta$ , CD28 and cluster of differentiation 2 (CD2). The pSMAC

contains LFA-1, CD4 and talin, while the distal region contains the larger CD43 and CD45 molecules.

In vivo experiments conducted by Stoll, Delon, Brotz and Germain (2002) used explanted lymph nodes to analyse the interactions of T-cells with DCs, showing the IS was sustained for hours (>15 hrs) before T-cell proliferation began. Their results agree with experimental data in vitro (Lipsky and Rosenthal, 1975), but do not agree with experimental results in 3D collagen matrices (Gunzer *et al.*, 2000), where the T-cells were activated through a series of short (< 15 min) interactions. Dustin (2007, 2008) has coined the word ‘kinapse’ to describe these short-lived T cell:APC interactions that promote activation. These do not have the stable, symmetrical properties of the mature synapse, but rather the T-cells remain highly motile leading to asymmetry in the engaged membrane, promoting short-lived interactions (Brossard *et al.*, 2005; Beemiller, Jacobi and Krummel, 2012). At present there have been few articles discussing short-contact-time activation mechanisms, and this is expected to be a fruitful area for future research.

Work by Mempel, Hendrickson and von Andrian (2004) identified three distinct phases of T-cell and DC interactions in lymph nodes during an immune response. The first phase, less than 8 hrs after the introduction of T-cells in the lymph node, showed short lived contacts with DCs and an average interaction time of 6 minutes. During the second phase, the T-cells became less motile and interactions with DCs persisted for over 60 minutes, resulting in upregulation of interleukin 2 (IL-2). After approximately 1 day, the T-cells became more motile and the short-lived contact times returned, although there was still evidence of some long-lived interactions.

More recently, the identification of TCR microclusters have been observed and studied (Krummel, Sjaastad, Wülfing and Davis, 2000; Douglass and Vale, 2005; Saito and Yokosuka, 2006; Yokosuka *et al.*, 2008). These microclusters contain TCR and CD28, along with kinase and adaptor proteins required for signalling, and are present throughout the contact duration (Campi, Varma and Dustin, 2005). Initially they appear uniformly throughout the contact zone, but as the synapse stabilises they are continually generated at the pSMAC and then migrate toward the cSMAC over time. Defects in microcluster assembly result in defects in T-cell activation, therefore suggesting a central role for TCR microclusters in synapse formation and T-cell activation (Bunnell *et al.*, 2006).

Figure 1.4 shows a schematic view of the synapse formation, derived from diagrams produced by Saito and Yokosuka (2006, 2010). Information relating to LFA-1 (Grakoui *et al.*, 1999), CD43 (Manjunath, Correa, Ardman and Ardman, 1995; Sperling *et al.*, 1998; Delon, Kaibuchi and Germain, 2001) and CD45 (Varma *et al.*, 2006) is also included. The initial contact (left panel) is characterised by a central accumulation of adhesion bonds, with TCR microclusters dispersed throughout the contact region and CD45 excluded from the contact

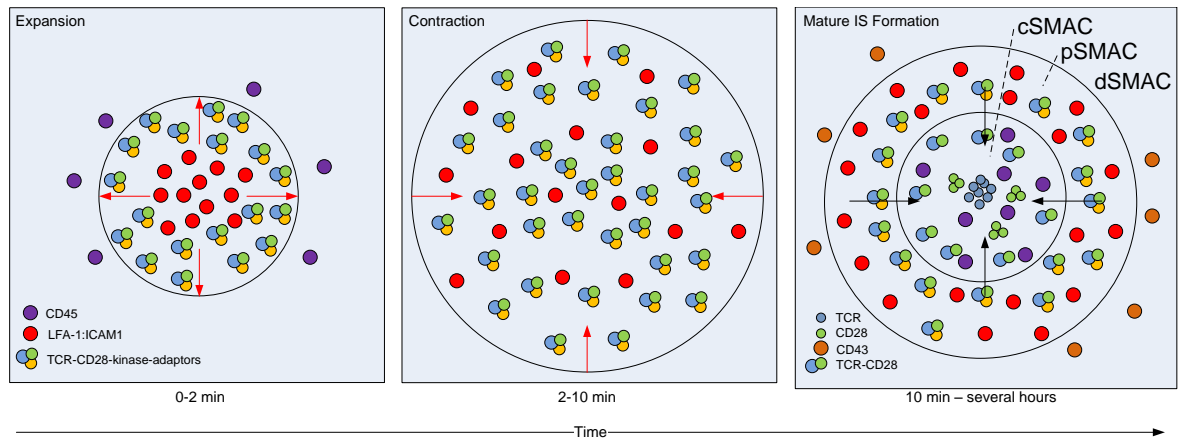


Figure 1.4: **The mature IS formation highlighting the spatial distribution and movements of TCR microclusters over time.** The figure is derived from diagrams produced by Saito and Yokosuka (2006, 2010), overlaying the LFA-1 movements from Grakoui *et al.*, 1999. The left panel shows the initial expansion stage, followed by the contraction phase (centre panel) and finally the mature synapse formation (right panel). The TCR microclusters are continually generated in the pSMAC, where signalling is greatest, and they migrate toward the cSMAC, detaching from the Src-kinase signalling components in the process.

zone. During the first 2 minutes after the initial contact the contact area undergoes an expansion phase, as indicated by the red arrows, where lamellipodia exist at the leading edge in all directions. The second stage is characterised by a contraction phase, where the contact interface stabilises moving toward the mature synapse pattern. During this phase (centre panel), the TCR microclusters and adhesion molecules mix in the contact interface. Finally, around 10 minutes the contact zone exhibits the mature synapse pattern including the cSMAC, pSMAC and dSMAC (right panel). It has been shown that cytoplasmic phosphorylated tyrosine residues associated with TCR signalling is maintained at high levels in the pSMAC and diminishes as TCR microclusters translocate toward the cSMAC (indicated by the black lines), where the the kinase and adaptor proteins dissociate from the microclusters (Mossman, Campi, Groves and Dustin, 2005; Yokosuka *et al.*, 2005). After the TCR-CD28 clusters enter the cSMAC they dissociate and 2 distinct domains appear, with the TCRs accumulating at the centre of the cSMAC, surrounded by CD28 aggregations (Yokosuka *et al.*, 2008; Kaizuka *et al.*, 2009). These results concerning microclusters contradict earlier speculation regarding the synapse function aided TCR signalling through the cSMAC. However, Čemerski *et al.* (2008) have reported that while signalling is initially concentrated in the pSMAC, at late times signalling occurs in the cSMAC and can increase the stimulatory potency of weak agonists for the TCR.

CD43 is excluded from the synapse region through ezrin-radixin-moesin (ERM) interactions (Allenspach *et al.*, 2001; Delon, Kaibuchi and Germain, 2001) and has a functional role inhibiting adhesion, thereby increasing the threshold for T-cell activation (Manjunath, Correa, Ardman and Ardman, 1995). It was felt that the exclusion of CD43 was necessary

to maintain strong TCR signalling in the contact zone (Davis and van der Merwe, 1996). However, Savage *et al.* (2002) have shown that inhibiting the ERM binding site, allowing CD43 to enter the central contact zone, has no effect on the activation of T-cells.

Varma *et al.* (2006) have also shown that CD45 concentration in the cSMAC is greater than the concentration of TCR microclusters and the area is enriched with lysobisphosphatidic acid, used to degrade membrane proteins. Since CD45 is a phosphatase, this action supports the reduced signalling observed in the cSMAC, but contradicts earlier postulation that larger molecules are excluded from the cSMAC (Davis and van der Merwe, 1996). The presence of lysobisphosphatidic acid supports the finding that TCRs are down-regulated in the cSMAC, with 40% of TCRs being down-regulated in the first 7 minutes and 90% down-regulated within an hour (Favier, Burroughs, Wedderburn and Valitutti, 2001).

The CD4 coreceptor molecule (not shown in figure 1.4) initially collocates with the TCR microclusters, but then moves to the periphery as the synapse stabilises. Early interpretation of this information was that CD4 helped boost the initial TCR signal through its cytoplasmic association with lymphoid cell kinase (Lck), but was not required once the synapse stabilised (Krummel, Sjaastad, Wülfing and Davis, 2000). However, with a view to the prolonged microcluster signalling in the pSMAC, the role of CD4 aiding TCR signalling throughout the synapse duration can not be discounted.

### 1.2.3 Intracellular Signalling

Engagement of the TCR with agonist pMHC results in an intracellular signalling cascade that leads to T-cell activation. Early studies show a clear dependency on TCR engagement and  $\text{Ca}^{2+}$  elevation for T-cell activation, defined by IL-2 production (Weiss, Imboden, Shoback and Stobo, 1984; Waldmann, 1989). Since these studies, many molecules and intracellular signalling pathways have been identified that regulate T-cell activation, relating to cytoskeletal remodelling, binding affinities and gene transcription. What follows is a discussion of a few of the signalling pathways relevant to the model results presented in chapters 5 and 6.

Upon binding with pMHC, immunoreceptor tyrosine-based activation motifs (ITAMs) on the cytoplasmic portion of the TCR are phosphorylated on tyrosine residues through Src-kinase enzymes (Lck and Fyn), that leads to subsequent recruitment and phosphorylation of  $\zeta$ -associated protein of 70 kDa (ZAP-70). The activated ZAP-70 subsequently phosphorylates the adaptor protein linker for activated T cells (LAT), whereupon SH2-domain-containing leukocyte-specific phosphoprotein of 76 kDa (SLP-76) and growth factor receptor-bound protein 2 (Grb2) can bind. Two signal transducing molecules downstream of SLP-76, phospholipase C  $\gamma$  1 (PLC $\gamma$ 1) and Wiscott Aldrich Syndrome protein (WASp), are necessary for the elevation of intracellular  $\text{Ca}^{2+}$  and actin remodelling (Finco *et al.*, 1998). Activated PLC $\gamma$ 1 produces

inositol triphosphate (IP3) and diacyl-glycerol (DAG), that results in increased concentration levels of intracellular  $\text{Ca}^{2+}$ , mediated through intracellular stores and  $\text{Ca}^{2+}$ -release-activated  $\text{Ca}^{2+}$  (CRAC) channels. This process also transduces the mitogen-activated protein kinase (MAPK) signalling cascade, leading to synthesis of activator protein-1 (AP-1) in the nucleus. The increase in  $\text{Ca}^{2+}$  also results in the production of calcineurin that is capable of dephosphorylating sites on nuclear factor of activated T-cells (NFAT), allowing it to migrate to the nucleus where it forms a complex with AP-1 and binds with DNA to promote gene expression (Northrop *et al.*, 1994; Hogan, Chen, Nardone and Rao, 2003; Macià, López-Rodriguez and Rao, 2001; Lewis, 2003). WASp is understood to relay signals from the CD2 and TCR receptors for remodelling of the actin cytoskeleton to form a stable synapse (Dustin *et al.*, 1998; Cannon *et al.*, 2001; Sechi and Wehland, 2004). Conversely,  $\text{PKC}\theta$  creates instabilities in the SMAC that result in broken symmetry, allowing the cell to migrate (Sims *et al.*, 2007). The interplay between WASp and  $\text{PKC}\theta$  is required by naive T-cells to migrate through the substrate.

Signalling via the bond formed between CD28 and CD80 molecules (CD28:CD80) in the pSMAC has a positive affect on the quantity of IL-2 production (Shen, Thams, Dustin and Kam, 2008) and early signals through the CD28:CD80 bonds are necessary for recruitment of additional molecules to the synapse through cytoskeletal effects (Wülfing and Davis, 1998). However, the effect of CD28 signalling on the TCR signalling pathways is not well understood and two contradictory reports have been published. Carey *et al.* (2000) produced results suggesting CD28 signalling augments signals from TCR through inhibition of Rap1, however, another study by Bromley *et al.* (2001) shows CD28 signalling in the cSMAC does not support adhesion or enhancement of TCR signalling.

Experimental measurements of the time duration for some of these signalling events and biological markers are detailed below in table 1.3. These experimental results show TCR

<b>Signalling Theme</b>	<b>Experimental Observation</b>
Lck	Lck phosphorylates ITAMs on the $\zeta$ chain within 3-6 seconds (Nika <i>et al.</i> , 2010). Activated Lck is continually generated in the pSMAC during the first 5 minutes after initial contact (Campi, Varma and Dustin, 2005).
LAT	LAT phosphorylation recorded at 4 seconds (Huse <i>et al.</i> , 2007).
ZAP-70	ZAP-70 is recruited to the TCR within 15 seconds of contact formation, with half-maximal recoveries within 7-10 seconds (Bunnell <i>et al.</i> , 2002). Houtman <i>et al.</i> (2005) recorded phosphorylation of ZAP-70 at 5 seconds.
Intracellular $\text{Ca}^{2+}$ elevation	Huse <i>et al.</i> (2007) recorded $\text{Ca}^{2+}$ elevation at 6-7 seconds. Bunnell <i>et al.</i> (2002) recorded $\text{Ca}^{2+}$ responses within 12 seconds.

Table 1.3: **Biological measurements for intracellular signalling Src-kinase phosphorylation events.**

related intracellular signalling activity is evident in the order of seconds, long before the

synapse stabilises in to the SMAC formation. The elevated  $\text{Ca}^{2+}$  levels are of particular importance, since elevated levels are necessary and sufficient to stop thymocyte migration in the thymus, allowing the stabilisation of cell:cell engagement (Bhakta, Oh and Lewis, 2005). Also, elevation of  $\text{Ca}^{2+}$  levels upon stimulation by agonist pMHC correlates with T-cell activation (Wülfing *et al.*, 1997).

#### 1.2.4 TCR Triggering Models

As described in the previous section, the movement of the cell surface proteins and the downstream signalling pathways have been studied extensively, but it is still not well understood how the TCR complex is triggered to induce the initial intracellular signalling required to promote IS formation. There have been a number of models proposed over the years and three models, that are relevant to this study, are outlined below.

Davis and van der Merwe (1996, 2006) proposed the Kinetic Segregation (KS) model, where the kinetic segregation of the cell surface molecules are determined through the minimisation of the energy function with respect to the bond lengths. They propose that the membrane dynamics, coupled with the two competing length scales of the TCR:pMHC and LFA-1:ICAM-1 bonds, are sufficient to drive segregation and aggregation of the sets of molecules. Under this assumption, the TCR are continuously phosphorylated and dephosphorylated maintaining a balance that avoids internal signalling and T-cell activation. During cell-cell adhesion the shorter bonds (TCR:pMHC, CD2:CD48 and CD28:CD80) form clusters that exclude larger molecules, such as LFA-1:ICAM-1 and the CD45 phosphatase, through steric barriers. The exclusion of CD45 enables prolonged phosphorylation of the TCR, resulting in intracellular signalling. There have been a number of experiments that support this model, including the initial segregation patterns produced showing TCR in the cSMAC and LFA-1 in the pSMAC (Monks *et al.*, 1998; Grakoui *et al.*, 1999); experiments varying the ectodomain size of CD45, where shortened versions inhibited TCR signalling (Cordoba *et al.*, 2013); experiments varying the CD48 length, where increased lengths disrupted the ability for T-cell activation (Wild *et al.*, 1999); and the relatively high level of activated Lck (40%) in unstimulated T-cells that is readily available upon TCR binding (Nika *et al.*, 2010).

There are also forces involved due to polarisation of the actin cytoskeleton toward the contact zone. Under these conditions, the molecules attached to the cytoskeleton, such as CD43, are transported away from the contact zone through ERM-dependent movement (Allenspach *et al.*, 2001). Savage *et al.* (2002) tested if the steric barrier created from the extracellular length difference affected the synapse formation and found no negative effects, supporting the ERM-dependent movement. This implies the KS model can not fully explain the SMAC formation and it is likely the balance between kinetic segregation and signalling pathways are

required.

Another model presented by Valittuti *et al.* (1995) is the Serial Triggering model. This model attempts to explain the anomaly between the requirement of sustained signalling for T-cell activation and the low binding affinity between TCR and pMHC. They propose that a single pMHC can serially trigger up to 200 TCRs, which using the dissociation rates exhibited by TCR:pMHC will require  $\sim 8,000$  TCRs for T-cell activation (Viola and Lanzavecchia, 1996). Recent work by Manz *et al.* (2011) shows a minimum density of agonist pMHC (4 molecules) available to a TCR microcluster is sufficient for T-cell activation and this number may be further reduced by the introduction of costimulatory signalling through CD28:CD80 bonds.

Finally, McKeithan (1995) proposed the Kinetic Proofreading model, that depends on the half-life of the TCR:pMHC bond. In this model the interactions between TCR and agonist pMHC are expected to have a longer half-life than TCR bonds with weak agonist or null peptide MHC molecules. The longer bond time facilitates stronger downstream signals required for T-cell activation and the shorter bond times ensures non-activation of T-cells to weak agonists of self MHC. This model is supported by results that show a correlation between the dissociation rate and T-cell activity, the faster dissociation rates result in weaker T-cell activity (Matsui *et al.*, 1994).

### 1.3 Mathematical Modelling of the Immunological Synapse

A number of mathematical models have been suggested for modelling different aspects of the biochemical processes observed during synapse formation. An early model of cell adhesion by Bell (1978) considered the binding rates, the strength of specific bonds and the force required to uproot a receptor from the membrane. Then, Bell, Dembo and Bongrand (1984) presented a thermodynamic calculus for modelling cell adhesion, including a free energy function that includes the attractive chemical potentials and repulsive forces due to the glycocalyx. This model is capable of measuring the thermodynamic equilibrium under a given set of parameters, that are sought from biological experiments. However, it did not include multiplicity of cell surface receptors and therefore could not be used to understand the membrane dynamics associated with two different bond lengths. As the complexity of the synapse formation is better understood, the models have grown more sophisticated to simulate membrane dynamics, surface protein kinetics (Qi, Groves and Chakraborty, 2001; Burroughs and Wülfing, 2002; Raychaudhuri, Chakraborty and Kardar, 2003; Chattopadhyay and Burroughs, 2007), and intracellular signalling pathways (Heinrich, Neel and Rapoport, 2002; Lee *et al.*, 2003; Burroughs, Lazic and van der Merwe, 2006).

Qi *et al.* (2001) proposed the first model to include TCR down-regulation and membrane

dynamics under thermal fluctuations, called the synapse assembly (SA) model. Their results were in near quantitative agreement with the experimental results produced by Grakoui et al. (1999), where they successfully reproduced the inversion pattern for LFA-1s and TCRs. An analysis of the model parameters highlighted the importance of the kinetic dissociation rates and the cell membrane properties in the formation of the synapse. Extensions of this model to include cytoskeletal forces have also been presented (Burroughs and Wülfing, 2002; Raychaudhuri, Chakraborty and Kardar, 2003), where similar comparable results have been produced along with phase diagrams that give an indication of permissible parameters changes, such as binding rates, that do not disrupt the synapse formation (Lee *et al.*, 2002). At the same time, a stability analysis of the SA model was produced that predicts the size differences of the bond lengths driving the segregation, showing the different bond lengths have a significant contribution to the free energy (Hori, Raychaudhuri and Chakraborty, 2002).

The importance of the close contact patch sizes and density during a steady state equilibrium for the protein molecule concentrations were quantified for the first time by Chattopadhyay and Burroughs (2007), and also the scale of the stochastic cellular fluctuations. They concluded that the density decreases exponentially as the membrane separation distance increases, but the mean patch sizes remain relatively unchanged. Their results conform with those of Raychaudhuri, Chakraborty and Kardar (2003) at the immature synapse formation level and the analysis relies on methods applied to the calculation of the persistence probability for the simple diffusion problem (Majumdar, Sire, Bray and Cornell, 1996; Chakraborty and Bhattacharjee, 2007). The method used to calculate the persistence probability was framed as the persistence within a close contact zone and was used to calculate the average size of the patches within a close contact region. The patch size was calculated to be in the order of tens of nanometers (Chattopadhyay and Burroughs, 2007). The small size implies that phosphatase exclusion (CD45) probably results from density fluctuations, implying a specific exclusion mechanism may not be required for CD45. Burroughs et al. (2011) also show that the protein segregation can be attributed to the extracellular domain sizes through thermodynamic arguments and these results validate some of the quantitative parameter ranges used in the SA model.

During cytoskeletal polarisation, the cell surface proteins bound to the actin skeleton may be translocated according to polarising forces, which adds non-thermal forces to the analysis. Chattopadhyay (2011) and Taloni, Chechkin and Klafter (2012) have proposed models that account for these non-thermal forces. The competition between thermal and non-thermal forces are currently being explored, but no quantitative results have been produced that can be verified by experimentation yet, since the spatio-temporal scales of nanometers and picoseconds compare with experimental tolerance/uncertainty limits. Also, TCR:pMHC half-life differences arising between cell-cell and cell-planar bilayer experiments have been

addressed using thermodynamic models, suggesting the rigidity of the molecular subdomains and changes in heat capacity upon binding account for the anomalies (Qi, Krosgaard, Davis and Chakraborty, 2006).

The membrane models outlined above are used to describe the cell surface molecular patterns and membrane shape distortions, however, they do not address the signal transduction events. There have been a number of models proposed in this respect, some that are based on the kinetic proofreading triggering model (Chan, George and Stark, 2001, 2004; Wedagedera and Burroughs, 2006), some that test the KS hypothesis through kinase-phosphatase models (Heinrich, Neel and Rapoport, 2002; Burroughs, Zorana and van der Merwe, 2006; Burroughs and van der Merwe, 2007) and Chiam (2007) suggests a Src kinase signalling model based on the Michealis-Menton equations to describe the rates of change for the protein kinases. While these models are not analysed further in this study, they are of interest when considering extensions to this work.

## 1.4 Research Questions

As discussed in the previous section, previous works (Hori, Raychaudhuri and Chakraborty, 2002) have analysed the phase separation properties about the thermodynamic limit for the SA model and the spatial size of TCR patches for the related steady-state linearised model (Chattopadhyay and Burroughs, 2007). What has not been studied are the temporal properties of the steady-state model, therefore the research questions addressed in this thesis are:

- What is the average contact time, predicted by the linear steady state membrane separation distance model, for a TCR:pMHC bond during early contact events between T-cells and APCs? This information will help quantify the IS bond strength.
- Does the average contact time predicted by the steady state model agree with experimental observations? This information will help to understand if the linear model is sufficient predict the TCR signalling events, that begin the progression to the mature synapse formation.
- The IS as a phenomenology, as well as from the modelling point of view, is driven by stochastic fluctuations. What is not known is the importance of the magnitude of these fluctuations in the bond formation process. So, what is the contribution of the low and high amplitude membrane fluctuations to the average contact time? The answer to this question will resolve what sort of mathematical theory could be used to model the IS.
- How does a change in the thermal noise strength alter the average contact time?

## 1.5 Thesis Organisation

Chapter 2 is a detailed description of the linearised steady-state membrane separation distance model, developed from the SA model proposed by Qi *et al.* (2001). In chapter 3 the analytical and numerical methods used to analyse the model are discussed. This is followed in chapter 4 by an asymptotical approximation of the temporal correlation function as the time difference tends to infinity. Chapters 5 and 6 present the analytical and simulation results, describing the temporal dynamics of the early contact periods between a T-cell and an APC, exploring the scaling dynamics in the large time limit where signalling occurs. Finally, chapter 7 discusses the implications of the present work and proposes possible extensions.

This thesis is primarily based on the published papers (Bush and Chattopadhyay, 2014; Bush and Chattopadhyay, 2015) and the manuscript under preparation (Bush and Chattopadhyay, 2016).

## Chapter 2

# Membrane Model

This chapter introduces the core nonlinear membrane model, including the derivation of the linearly stable non-equilibrium model that forms the basis of the theoretical analysis in the later chapters. Section 2.1 presents the SA model, including a description of the terms included in the equations, the model parameters and a discussion on proposed variations to this simple model. In section 2.2, the linearization steps required to construct the model used to describe the dynamics of the local membrane separation distance are shown, under the assumption of steady state cell surface protein concentration levels. Finally, in section 2.2.1 the final form of the linearized model is presented and the relevant biological parameter values are defined, that are subsequently used in the analysis presented in later chapters.

### 2.1 Synapse Assembly Model

Qi *et al.* (2001) proposed the nonlinear SA model, that includes the TCR and LFA-1 surface molecules on the T-cell and the pMHC and ICAM-1 molecule on the antigen presenting cell. As shown elsewhere (Burroughs and Wülfing, 2002), these two sets of surface proteins are sufficient to model two different bond lengths interacting in the synaptic junction, TCR:pMHC (15nm) and LFA-1:ICAM-1 (45nm). The model uses the Smoluchowski (reaction-diffusion) setup coupled with a time-dependent Landau-Ginzberg model (Van Kampen, 1987), where two interacting two-dimensional membranes are considered, one fluctuating and the other a flat, static, membrane. Using parameter values derived from experimental results, this model was able to reproduce the bullseye pattern observed for the mature IS, in near quantitative agreement with experimental findings (Monks *et al.*, 1998; Grakoui *et al.*, 1999). Table 2.1 and equations (2.1) to (2.3) are reproduced from the article by Qi *et al.*, listing the variables and equations that define the SA model.

Equation (2.1) describes the free energy in the system. The first term represents the contribution of the TCR:pMHC bond to the free energy. Deviations from the natural bond

Symbol	Description
$F$	Free Energy
$C_T$	TCR concentration in the T-cell membrane
$C_M$	MHC-peptide concentration in the APC membrane
$C_{TM}$	TCR:MHC-peptide complex concentration
$C_{Tt}$	Triggered TCR concentration in the T-cell membrane
$C_{Ai}$	Concentration of the $i$ th adhesion molecule on the T-cell membrane (LFA-1)
$C_{Bi}$	Concentration of the $i$ th ligand on the APC membrane (ICAM-1)
$C_i$	Concentration of the bound complex formed between $A_i$ and $B_i$
$k_{\text{on}}$	On rate for TCR/MHC-peptide binding
$k_{\text{off}}$	Off rate for TCR/MHC-peptide binding
$k_i$	On rate for $i$ th complex binding
$k_{-i}$	Off rate for $i$ th complex binding
$D_j$	Diffusion coefficient for the $j$ th surface protein in the appropriate membrane
$z$	Intermembrane separation distance
$z_j$	Natural bond length of the $j$ th bond complex
$t$	Time
$\gamma$	Interfacial tension of cell membrane
$\kappa$	Bending rigidity of the cell membrane
$\zeta$	Thermal noise, assumed to be white noise
$k_B T$	Thermal energy at temperature T
$M$	Phenomenological constant for membrane response to free energy
$\lambda_j$	Curvature of binding energy well for $i$ th complex
$P$	The percentage of triggered TCR concentration following pMHC binding
$k_t$	The rate of down-regulation for the triggered TCRs

Table 2.1: **SA membrane model variables.**

length,  $z_{TM}$ , result in a change in the free energy. When the separation distance is larger than the natural bond length, there is an energy cost due to the stretching of the bond and there is also an energy cost when the separation distance is less than the natural bond length, due to the tendency of the “squashed” bond to return to its natural length. The second term in the equation applies the same principle to the adhesion bonds, LFA-1:ICAM-1. Finally, the third term uses the Helfrich Hamiltonian (Safran, 2003) to model the free energy associated with changes to the membrane shape, applying a penalty for the creation of new area (stretching) and also high curvature (bending). An assumption is made here to ignore the Gaussian curvature term, since the membrane is assumed not to undergo any topological changes. The parameters associated with the bending modulus ( $\kappa$ ) and the stretching modulus ( $\gamma$ ) are constants, that assumes the lipid bilayer composition remains unchanged during synapse formation. It may be noted that initial TCR signalling leads to the opening of CRAC channels to increase intracellular  $\text{Ca}^{2+}$  levels, whereupon the membrane becomes increasingly porous and it is likely that these parameters will be altered during the formation of the synapse.

The set of equations (2.2) show the rate of change in the cell surface protein concentrations with respect to time. The concentration of the uncoupled molecules is dependent on their diffusive rates in the membrane, as well as their propensity to couple and uncouple from their complimentary ligands. The model can be used to include any number of adhesion-

ligand bonds through equations (2.2d), (2.2e) and (2.2g), although Qi *et al.* only include the TCR:pMHC and LFA-1:ICAM-1 that exemplify the different bond lengths. The coreceptor molecules and their natural ligands (the bond formed between CD2 and CD58 molecules (CD2:CD58) and the bond formed between CD28 and CD80 molecules (CD28:CD80)) have a bond length similar to that of the TCR:pMHC and will effect the free energy similar to increasing the concentration levels of the TCR:pMHC bond, assuming the binding affinities are similar. In all cases, the thermal noise, due to external forces, is assumed to be white noise.

$$\begin{aligned}
F &= \frac{\lambda_T}{2} \int dx \int dy C_{TM}(x, y, t) \cdot [z(x, y, t) - z_{TM}]^2 \\
&\quad + \sum_i \frac{\lambda_i}{2} \int dx \int dy C_i(x, y, t) \cdot [z(x, y, t) - z_i]^2 \\
&\quad + \frac{1}{2} \int dx \int dy \left[ \gamma (\nabla z(x, y, t))^2 + \kappa (\nabla^2 z(x, y, t))^2 \right]
\end{aligned} \tag{2.1}$$

$$\frac{\partial C_T}{\partial t} = D_T \nabla^2 C_T - k_{\text{on}}(z) C_T C_M + k_{\text{off}}(1 - P) C_{TM} + \zeta_T \tag{2.2a}$$

$$\frac{\partial C_{Tt}}{\partial t} = D_T \nabla^2 C_{Tt} - k_i C_{Tt} + P k_{\text{off}} C_{TM} + \zeta_{Tt} \tag{2.2b}$$

$$\frac{\partial C_M}{\partial t} = D_M \nabla^2 C_M - k_{\text{on}}(z) C_T C_M + k_{\text{off}} C_{TM} + \zeta_M \tag{2.2c}$$

$$\frac{\partial C_{A_i}}{\partial t} = D_{A_i} \nabla^2 C_{A_i} - k_i(z) C_{A_i} C_{B_i} + k_{-i} C_i + \zeta_{A_i} \tag{2.2d}$$

$$\frac{\partial C_{B_i}}{\partial t} = D_{B_i} \nabla^2 C_{B_i} - k_i(z) C_{A_i} C_{B_i} + k_{-i} C_i + \zeta_{B_i} \tag{2.2e}$$

$$\frac{\partial C_{TM}}{\partial t} = D_{TM} \left[ \nabla^2 C_{TM} + \frac{1}{k_{BT}} \nabla \cdot C_{TM} \nabla \frac{\delta F}{\delta C_{TM}} \right] + k_{\text{on}}(z) C_T C_M - k_{\text{off}} C_{TM} + \zeta_{TM} \tag{2.2f}$$

$$\frac{\partial C_i}{\partial t} = D_i \left[ \nabla^2 C_i + \frac{1}{k_{BT}} \nabla \cdot C_i \nabla \frac{\delta F}{\delta C_i} \right] + k_i(z) C_{A_i} C_{B_i} - k_{-i} C_i + \zeta_i \tag{2.2g}$$

$$\frac{\partial z}{\partial t} = -M \frac{\delta F}{\delta z} + \zeta \tag{2.3}$$

Equation (2.2b) attempts to capture the effects of TCR down-regulation following TCR triggering (Valitutti *et al.* 1995). A TCR is considered to be triggered once the signal components have assembled on the cytoplasmic portion of the TCR, as described in section 1.2.3. TCRs that have been bound to pMHC for a sufficient time are triggered and subsequently internalised and degraded, whereas the non-triggered TCR are free to make new bonds. When modelling the early contact time period, immediately following the initial contact between the cells, there is no spatial differentiation associated with down-regulation of TCR. However, Varma *et al.* (2006) show that once the mature synapse has formed TCR internalisation is more prevalent in the cSMAC, therefore this term could include some form of spatial dependency at later stages of the synapse development. A recent work by Choudhuri *et al.* (2014) has provided evidence of TCR detachment in the cSMAC during the synapse disengagement

process, as cells detach and the T-cell resumes migration. While this would not appear to affect the formation of the synapse, it may be included at later stages in the T-cell:APC engagement. The  $Pk_{\text{off}}C_{TM}$  term models the concentration of triggered TCRs, where the kinetic constant  $P$  is approximated by  $P = \exp[-k_{\text{off}}\tau]$  and  $\tau$  is the half-life of the TCR:pMHC bond. Valitutti and Lanzavecchia (1997) suggest TCR:pMHC ligation greater than 5 seconds results in full triggering, 3-5 seconds results in partial triggering and less than 3 seconds corresponds to TCR inactivation.

Equations (2.2f) and (2.2g) relate to the bound complexes, where an additional term is included to model the chemical potential forces, driving the translocation of the complexes toward regions where the membrane separation distance is close to the unstressed bond length (Hori, Raychaudhuri and Chakraborty, 2002). And finally, equation (2.3) shows the Langevin-modelled time evolution of the membrane separation distance, as a functional derivative of the free energy. This equation is a time-dependent Langevin equation for the non conserved order parameter  $z(x, y, t)$ .

The coupled equations demonstrate some of the intrinsic links between the different membrane components, although there are a number of simplifications in this model. One simplification is the exclusion of the cytoskeletal effects on membrane bound molecules. It has been noted that the actin cytoskeleton is continuously remodelled throughout the synapse life-cycle, resulting in an expansion phase, a contraction phase and once the synapse is formed there is centripetal transport of TCRs toward the cSMAC (Saito and Yokosuka, 2006; Wülfing and Davis 1998). Drugs employed to interfere with the actin assembly have effectively stopped the transport of TCRs toward the cSMAC and affected the stability of the synapse (Delon, Bercovici, Liblau and Trautmann, 1998).

Improvements on the SA model that address the cytoskeletal effects have included an extra term in equations (2.2) (Lee *et al.* 2002; Burroughs and Wülfing 2002; Hori, Raychaudhuri and Chakraborty, 2002), for example

$$\frac{\partial C_T}{\partial t} = D_T \nabla^2 C_T - k_{\text{on}}(z) C_T C_M + k_{\text{off}}(1 - P) C_{TM} - \nabla \cdot \mathbf{V} C_T + \zeta_T \quad (2.4)$$

where  $\mathbf{V}$  is the cytoskeletal directional velocity and the  $\nabla \cdot \mathbf{V}$  term models the effect of the cytoskeletal centripetal flow on membrane bound molecules. The model suggested by Burroughs and Wülfing (2002) also includes additional equations of motion to describe the attachment of the molecules to the cytoskeleton. For example, the concentration of TCR:pMHCs attached to the cytoskeleton,  $C_{TM}^{\text{at}}$ , is modelled through equation (2.5)

$$\frac{\partial C_{TM}^{\text{at}}}{\partial t} = -\nabla \cdot \mathbf{V} C_{TM}^{\text{at}} - p_{\text{off}} C_{TM}^{\text{at}} + p_{\text{on}} C_{TM} + k_{\text{on}}(z) C_T C_M - k_{\text{off}} C^{\text{at}} \quad (2.5)$$

where  $\mathbf{V}$  is the cytoskeletal velocity and the TCR attachment and detachment rates to the cytoskeleton are given by  $p_{\text{on}}$  and  $p_{\text{off}}$ , respectively. Analysis of this model points to a necessary requirement of seeding/nucleation of surface molecules, along with bond elasticity conditions, to produce segregation. Their work reinforces the significant effect differential bond lengths have on the free energy and the spatial segregation of different molecules in the IS. However, while the addition of cytoskeletal effects present a more detailed view of the cellular dynamics, the thermodynamics corresponding to the free energy functional driving the cell membrane shape has been analysed by Hori, Raychaudhuri and Charkaborty (2002). They show that for small values of  $\mathbf{V}$  in equation (2.4) the qualitative physics of pattern formation do not change from the case where only diffusion is used to transport the molecules.

It may also be noted, the binding parameters for the association and dissociation rates in equation (2.2) ( $k_{\text{on}}$ ,  $k_i$ ,  $k_{\text{off}}$ ,  $k_{-i}$ ) are modelled by Gaussian distributions centred on the natural bond lengths. This simplification of the binding dynamics does not capture the affinity changes observed empirically. Lollo *et al.* (1993) have shown a percentage of the LFA-1:ICAM-1 affinity is increased 200-fold upon T-cell stimulation and CD2 affinity is also increased. Springer and Dustin (2012) have also shown LFA-1 affinity can be increased in orders of  $10^3$  to  $10^4$  when in an open-extended state, although it is not clear how the change of state from the bent or close-extended state occurs. Also, large differences have been noted in the binding rates of TCR:pMHC measured in solution, compared with those measured *in situ*. Huppa *et al.* (2010) used single molecule microscopy and fluorescence resonance energy transfer (FRET) to show the dissociation rates increased 4-12-fold *in situ* and association rates increased by 100-fold, leading to an increased TCR affinity for MHC. These studies highlight the sensitivity of the parameters on the environmental conditions.

Finally, the model was created before the identification of TCR microclusters, subsequently the understanding of the cell surface protein movements has altered significantly. This model does not accommodate the expansion and contraction phases during the synapse formation as shown in figure 1.4. Also, the results drawn from this model agree with the synapse formation images produced by Monks *et al.* (1998) and Grakoui *et al.* (1999). The later images produced by a number of labs (Campi, Varma and Dustin, 2005; Douglass and Vale, 2005; Yokosuka *et al.*, 2005) show TCR microcluster signalling in the pSMAC indicating the membrane separation distance in this region must facilitate bonds of 15nm, something that is not evident in the results of Qi *et al.*

## 2.2 Steady State Linearized Membrane Separation Distance Model

While the SA model attempts to describe the nonlinear dynamics during the formation of the synapse from the immature to the mature structure, the focus here is directed toward the early contact times where initial TCR signalling occurs. The start point is the nonlinear coupled equations (2.1)-(2.3). Linearizing the system around a steady-state homogeneous solution, such that the surface membrane protein concentrations are constant and nontrivial at time  $t_0$ , the linearly stable SA model becomes

$$\frac{\partial C_j}{\partial t} = 0, \quad C_j(x, y, t_0) > 0, \quad j = T, Tt, M, Ai, Bi, TM, i \quad (2.6)$$

$$\begin{aligned} F &= \frac{\lambda_T}{2} \int dx \int dy C_{TM}(x, y, t_0) \cdot [z(x, y, t) - z_{TM}]^2 \\ &\quad + \sum_i \frac{\lambda_i}{2} \int dx \int dy C_i(x, y, t_0) \cdot [z(x, y, t) - z_i]^2 \\ &\quad + \frac{1}{2} \int dx \int dy \left[ \gamma (\nabla z(x, y, t))^2 + \kappa (\nabla^2 z(x, y, t))^2 \right] \end{aligned} \quad (2.7)$$

$$\frac{\partial z}{\partial t} = -M \frac{\delta F}{\delta z} + \zeta \quad (2.8)$$

The time evolution of the membrane separation distance is modelled by a Langevin equation, and is determined solely by the functional derivative of the free energy, that is dependent on the reaction kinetics of the bound molecules and the membrane deformation dynamics. The freely moving surface proteins do not have a role in the linearized model, except to say that the number of bonds being created must equal the number of dissociating bonds at the equilibrium point. Appendix A shows the derivation of the Langevin equation that arises for the local separation distance,  $z(x, y, t)$ , when the SA model is linearized about this steady state equilibrium. The resulting Langevin equation is given by

$$\frac{\partial z(x, y, t)}{\partial t} = -M \left[ \kappa \nabla^4 z(x, y, t) - \gamma \nabla^2 z(x, y, t) + \lambda z(x, y, t) + \sigma \right] + \zeta(x, y, t) \quad (2.9)$$

where

$$\lambda = \lambda_T C_{TM}(x, y, t_0) + \sum_i \lambda_i C_i(x, y, t_0) \quad (2.10)$$

$$\sigma = \lambda_T C_{TM}(x, y, t_0) z_{TM} + \sum_i \lambda_i C_i(x, y, t_0) z_i \quad (2.11)$$

Equation (2.11) describes the total chemical potential of the binding energy for the unstretched bonds, when they are resting at their natural bond length. This is the mean separation distance that the unperturbed system will tend toward. Equation (2.10) represents the strength of the binding energy associated with the bound complexes at time  $t_0$ .

This coefficient acts as a damping term, that draws  $z(x, y, t)$  toward the mean separation distance  $\sigma$ .

### 2.2.1 Chattopadhyay and Burroughs Model

Chattopadhyay and Burroughs (2007) have used a similar form of this linear model to determine the spatial patch sizes for different bond lengths in the interface. They used a translation in  $z$  that consumes the  $\sigma$  term,  $z \mapsto z - \frac{\sigma}{\lambda}$ , that effectively performs a linear translation fixing the model about the mean separation distance. The specific form of the resulting set of equations is given by

$$M \frac{\partial z(x, y, t)}{\partial t} = -B \nabla^4 z(x, y, t) + \gamma \nabla^2 z(x, y, t) - \lambda z(x, y, t) + \eta(x, y, t) \quad (2.12a)$$

$$\langle \eta(x, y, t) \rangle = 0 \quad (2.12b)$$

$$\langle \eta * \eta' \rangle = 2D \delta(x - x') \delta(y - y') \delta(t - t') \quad (2.12c)$$

where  $\eta * \eta' = \eta(x, y, t) \eta(x', y', t')$  and the model parameter values were calculated as shown in table 2.2. The properties of the thermal noise are described by equations (2.12b)

Parameter	Description	Value	Units
$M$	Phenomenological Parameter	$4.7 \times 10^6 k_B T$	$s \mu\text{m}^{-4}$
$B$	Membrane rigidity (normal force)	$11.8 k_B T$	
$\gamma$	Membrane surface tension	$5650 k_B T$	$\mu\text{m}^{-2}$
$\lambda$	Total reaction binding force	$6.0 \times 10^5 k_B T$	$\mu\text{m}^{-4}$
$D$	Delta correlated thermal noise strength	$4.7 \times 10^6 (k_B T)^2$	

Table 2.2: **Steady state membrane separation distance model parameters.** Model parameters calculated by Chattopadhyay and Burroughs (2007).

and (2.12c). The first equation ensures the net force imposed by the thermal noise on the system has an ensemble average of zero and the second equation describes the spatial and temporal correlation for the noise. A delta correlation, with strength proportional to  $D$ , is required to satisfy the equipartition law and is called a white noise force (Risken, 1989). And, while it is noted that changes in the lipid bilayer resulting from signalling may lead to non-constant parameter values for the bending modulus and stretching modulus, in the linear model the constant values may be justified by the small time duration considered. Using this model and parameters, Chattopadhyay and Burroughs (2007) estimated the average size of the close contact patches at  $\sim 84\text{nm}$ , in agreement with experimental results by Krummel, Sjaastad, Wülfing and Davis (2000).

As noted in section 2.1, the SA model was developed prior to the discovery of TCR microclusters and the linearized version of the model is identified with the early contact times when the TCR:pMHC and LFA-1:ICAM-1 bonds mix in the same region of the membrane, before the onset of the mature synapse. The existence of TCR microcluster signalling in the

pSMAC, where LFA-1:ICAM-1 bonds are also located, suggests the linearized model can also be used to model the dynamics in the pSMAC once the mature synapse has formed, since there exists a mix of the two different bond lengths in this regime.

# Chapter 3

## Theoretical Methods

This chapter outlines the approach taken and the methods used to analyse the temporal behaviour of the early contact patches in the IS. The methods used have their roots in thermodynamics and statistical physics, specifically related to phase-ordering of quenched systems and first passage probability problems. Section 3.1 outlines the analytical methods used to analyse the linear steady state membrane separation distance model. The following section, 3.2, presents a full description of the numerical methods used to produce a computer simulation for the problem.

### 3.1 Analytical Methods

The *Time Persistence Method*, described below, builds on a Gaussian Stationary Process structure to derive the probability density function associated with membrane:membrane contact patches. This method has previously been applied to the Ising, Simple Diffusion and Random Walk models (Majumdar and Sire, 1996; Majumdar, Sire, Bray and Cornell, 1996; Chakraborty and Battacharjee, 2007). It has also been used to determine the close contact patch size in the linear IS model described by equation (2.12) (Chattopadhyay and Burroughs, 2007). This section describes the analytical methods required to implement the time persistence method on the linear IS model, with a view to analysing the temporal dynamics. Section 3.1.1 presents a solution for  $z(x, y, t)$  in equation (2.12), using the Fourier transform method. In the following section 3.1.2, an estimate is derived for the probability density function for the local membrane separation distance, calculated using the steady state Fokker-Planck description. Then, section 3.1.3 shows a derivation of the temporal correlation function for the problem. Similar problems have been analysed using a scaling approach (Barabasi and Stanley, 1995), however, section 3.1.4 highlights the problems using this approach for the linear IS problem. Then, in section 3.1.5 a description of the *independent interval approximation* (IIA) method is given, that leads to the calculation required to deter-

mine the average time persistence for a Gaussian Stationary Process. Finally, section 3.1.6 extends the IIA method to include a single threshold, that is used to determine the bond persistence for the linear IS model.

### 3.1.1 Integral Equation Solution of the Langevin Equation

In this section, a solution is derived for the linear membrane model defined in equation (2.12), that is further detailed in appendix B. In the following sections, vector notation is used to define the  $x, y$  dimensions in the plane of the membrane, such that  $\mathbf{x} = \begin{bmatrix} x & y \end{bmatrix}^T$ . In this case, equation (2.12) can be rewritten

$$M \frac{\partial z(\mathbf{x}, t)}{\partial t} = -B \nabla^4 z(\mathbf{x}, t) + \gamma \nabla^2 z(\mathbf{x}, t) - \lambda z(\mathbf{x}, t) + \eta(\mathbf{x}, t) \quad (3.1a)$$

$$\langle \eta(\mathbf{x}, t) \rangle = 0 \quad (3.1b)$$

$$\langle \eta(\mathbf{x}, t) \eta(\mathbf{x}', t') \rangle = 2D \delta(\mathbf{x} - \mathbf{x}') \delta(t - t'). \quad (3.1c)$$

Using the complementary Fourier transforms,

$$\mathcal{F}\{z(\mathbf{x}, t)\} = \tilde{z}(\mathbf{k}, t) = \frac{1}{2\pi} \int_{\Omega} z(\mathbf{x}, t) e^{-i\mathbf{k}\cdot\mathbf{x}} d\mathbf{x} \quad (3.2a)$$

$$\mathcal{F}^{-1}\{\tilde{z}(\mathbf{k}, t)\} = z(\mathbf{x}, t) = \frac{1}{2\pi} \int_{-\infty}^{\infty} \tilde{z}(\mathbf{k}, t) e^{i\mathbf{k}\cdot\mathbf{x}} d\mathbf{k} \quad (3.2b)$$

$$\mathcal{F}\{\eta(\mathbf{x}, t)\} = \tilde{\eta}(\mathbf{k}, t) = \frac{1}{2\pi} \int_{\Omega} \eta(\mathbf{x}, t) e^{-i\mathbf{k}\cdot\mathbf{x}} d\mathbf{x} \quad (3.3a)$$

$$\mathcal{F}^{-1}\{\tilde{\eta}(\mathbf{k}, t)\} = \eta(\mathbf{x}, t) = \frac{1}{2\pi} \int_{-\infty}^{\infty} \tilde{\eta}(\mathbf{k}, t) e^{i\mathbf{k}\cdot\mathbf{x}} d\mathbf{k} \quad (3.3b)$$

where  $\mathbf{k} = \begin{bmatrix} k_1 & k_2 \end{bmatrix}^T$  and  $\Omega$  describes the surface area considered. The Langevin equation (3.1a) can then be expressed in the  $k - t$  space as

$$\frac{\partial \tilde{z}(\mathbf{k}, t)}{\partial t} = -\alpha(\mathbf{k}) \tilde{z}(\mathbf{k}, t) + \frac{\tilde{\eta}(\mathbf{k}, t)}{M} \quad (3.4)$$

where

$$\alpha(\mathbf{k}) = \frac{1}{M} \left( B|\mathbf{k}|^4 + \gamma|\mathbf{k}|^2 + \lambda \right) \quad (3.5)$$

Then, equation (3.4) can be solved using the integrating factor method, as

$$\tilde{z}(\mathbf{k}, t) = e^{-\alpha(\mathbf{k})t} \left[ \frac{1}{M} \int_{t_0}^t e^{\alpha(\mathbf{k})t'} \tilde{\eta}(\mathbf{k}, t') dt' + \tilde{z}_0(\mathbf{k}, t, t_0) \right] \quad (3.6)$$

whereupon, the inverse transform equation (3.2b) is applied to express the time-dependent

solution as an integral equation

$$z(\mathbf{x}, t) = \frac{1}{2\pi M} \int d\mathbf{k} \int_{t_0}^t dt' e^{-\alpha(\mathbf{k})(t-t') + i\mathbf{k}\cdot\mathbf{x}} \tilde{\eta}(\mathbf{k}, t') + z_0(\mathbf{x}, t, t_0) \quad (3.7)$$

where

$$z_0(\mathbf{x}, t, t_0) = \frac{1}{2\pi} \int_{-\infty}^{\infty} d\mathbf{k} \tilde{z}_0(\mathbf{k}, t_0) e^{-\alpha(\mathbf{k})t} e^{i\mathbf{k}\cdot\mathbf{x}} = \mathcal{F}^{-1} \left\{ \tilde{z}_0(\mathbf{k}, t_0) e^{-\alpha(\mathbf{k})t} \right\} \quad (3.8)$$

describes the relevant contribution from the initial condition  $\tilde{z}_0(\mathbf{k}, t_0)$ . The  $\alpha(\mathbf{k})$  function is positive definite, with a minimum at  $\mathbf{k}_0 = [0 \ 0]^T$  of  $\alpha(\mathbf{k}_0) = \lambda/M$ . Therefore,  $z_0(\mathbf{x}, t, t_0) \rightarrow 0$  as  $t \rightarrow \infty$ , such that, following an initial relaxation period the effect of the initial conditions are negligible. In practice, the initial condition,  $z_0(\mathbf{x}, t, t_0)$ , is set to zero. This corresponds to a configuration where the entire membrane:membrane contact region is set at the mean intermembrane separation distance.

### 3.1.2 Fokker-Planck Equation for the Steady State Probability Distribution

In this section, the Fokker-Planck equation is used to study the steady state probability density distribution for the local mean separation distance, where it can be shown the steady state probability density distribution admits of a Gaussian form. The Langevin equation in the  $k - t$  space, equation (3.4), may be expressed in the form

$$\frac{\partial \tilde{z}(\mathbf{k}, t)}{\partial t} = f(\tilde{z}(\mathbf{k}, t), t) + g(\tilde{z}(\mathbf{k}, t), t)\zeta(\mathbf{k}, t) \quad (3.9)$$

where  $\zeta$  has zero mean and unit variance. The linear IS model is mapped to equation (3.9) through the functions

$$f(\tilde{z}(\mathbf{k}, t), t) = -\alpha(\mathbf{k})\tilde{z}(\mathbf{k}, t) \quad (3.10)$$

$$g(\tilde{z}(\mathbf{k}, t), t) = \frac{\sqrt{2D}}{M} \quad (3.11)$$

where  $g(\tilde{z}(\mathbf{k}, t), t)$  is a constant function that is independent of time and the separation distance, that will be defined by the constant variable  $g$ . In the form presented in equation (3.9), it can be shown that the Langevin equation is equivalent to the forward Fokker-Planck equation for the probability distribution  $P(\tilde{z}_{\mathbf{k}}, \mathbf{k}, t)$ , that is the probability the system is at the separation distance in the  $k - t$  space,  $\tilde{z}_{\mathbf{k}}$ , at time  $t$  (Risken, 1989). Using the probability definition,

$$P(\tilde{z}_{\mathbf{k}}, \mathbf{k}, t) = \langle \delta(\tilde{z}_{\mathbf{k}} - \tilde{z}(\mathbf{k}, t)) \rangle \quad (3.12)$$

where the ensemble is taken over all noise realisations, the Langevin equation (3.9) gives rise to the corresponding time-dependent Fokker-Planck equation

$$\frac{\partial}{\partial t} P(\tilde{z}_{\mathbf{k}}, \mathbf{k}, t) = -\frac{\partial}{\partial \tilde{z}_{\mathbf{k}}} [f(\tilde{z}_{\mathbf{k}}) P(\tilde{z}_{\mathbf{k}}, \mathbf{k}, t)] + \frac{\partial^2}{\partial \tilde{z}_{\mathbf{k}}^2} \left[ \frac{g^2}{2} P(\tilde{z}_{\mathbf{k}}, \mathbf{k}, t) \right], \quad (3.13)$$

that describes the time evolution of the probability density function for the process. The steady state solution occurs when  $\frac{\partial P(\tilde{z}_{\mathbf{k}}, \mathbf{k}, t)}{\partial t} = 0$  and the steady state probability distribution is given by  $P_s(\tilde{z}_{\mathbf{k}}, \mathbf{k})$ , such that

$$\frac{\partial}{\partial \tilde{z}_{\mathbf{k}}} \left[ -f(\tilde{z}_{\mathbf{k}}) P_s(\tilde{z}_{\mathbf{k}}, \mathbf{k}) + \frac{g^2}{2} \frac{\partial}{\partial \tilde{z}_{\mathbf{k}}} P_s(\tilde{z}_{\mathbf{k}}, \mathbf{k}) \right] = 0. \quad (3.14)$$

A solution exists when the term inside the square brackets is constant, that can be set to 0 without loss of generality, then

$$\frac{g^2}{2} \frac{\partial}{\partial \tilde{z}_{\mathbf{k}}} P_s(\tilde{z}_{\mathbf{k}}, \mathbf{k}) - f(\tilde{z}_{\mathbf{k}}) P_s(\tilde{z}_{\mathbf{k}}, \mathbf{k}) = 0 \quad (3.15)$$

that for the linear IS model is

$$\frac{\partial}{\partial \tilde{z}_{\mathbf{k}}} P_s(\tilde{z}_{\mathbf{k}}, \mathbf{k}) + \frac{M^2 \alpha(\mathbf{k})}{D} \tilde{z}_{\mathbf{k}} P_s(\tilde{z}_{\mathbf{k}}, \mathbf{k}) = 0. \quad (3.16)$$

Using the integrating factor method, equation (3.16) can be solved

$$P_s(\tilde{z}_{\mathbf{k}}, \mathbf{k}) = C e^{-\frac{M^2 \alpha(\mathbf{k})}{D} \tilde{z}_{\mathbf{k}}^2} \quad (3.17)$$

where  $P_s$  is a function of  $\mathbf{k}$  and  $\tilde{z}_{\mathbf{k}}$ , and  $C$  is the normalisation factor. Applying the inverse Fourier transform and through a little manipulation, as shown in appendix G.2, the probability density distribution for the local membrane separation distance can be modelled by the following Gaussian form

$$P(Z, \mathbf{x}, t) = \langle \delta(Z - z(\mathbf{x}, t)) \rangle = \left( \frac{1}{2\pi \sum_{\mathbf{k}} A(\mathbf{k}, \mathbf{x})} \right)^{\frac{1}{2}} e^{-\frac{Z^2}{2 \sum_{\mathbf{k}} A(\mathbf{k}, \mathbf{x})}} \quad (3.18)$$

with

$$\sum_{\mathbf{k}} A(\mathbf{k}, \mathbf{x}) = \frac{D}{2\pi^2 M^2} \int d\mathbf{k} \frac{e^{2i\mathbf{k} \cdot \mathbf{x}}}{\alpha(\mathbf{k})}. \quad (3.19)$$

### 3.1.3 Temporal Two Point Correlation Function

In this section, the calculation is outlined for the two point temporal correlation function

$$c_{12}(z(\mathbf{x}, t_1), z(\mathbf{x}, t_2)) = \langle z(\mathbf{x}, t_1) z(\mathbf{x}, t_2) \rangle, \quad (3.20)$$

using the time-dependent solution for the local intermembrane separation distance, equation (3.7). The temporal correlation for  $t_2 \geq t_1$  can be written as the sum of two integrals (see Appendix C.1 for the full derivation)

$$\langle z(\mathbf{x}, t_1) z(\mathbf{x}, t_2) \rangle = \frac{D}{(2\pi) M^2} \left[ \int_0^\infty r \frac{e^{-\alpha(r)\tau}}{\alpha(r)} dr - \int_0^\infty r \frac{e^{-\alpha(r)(\tau'-2t_0)}}{\alpha(r)} dr \right] + \langle z_0^2 \rangle \quad (3.21)$$

where  $\tau = t_2 - t_1$  is the time difference between two time points,  $\tau' = t_1 + t_2$  is the sum of the two time points,  $z_0$  is dependent on the initial conditions and the scalar function  $\alpha(r)$  (not to be confused with equation (3.5), although it has a similar form) is given by

$$\alpha(r) = \frac{Br^4 + \gamma r^2 + \lambda}{M} . \quad (3.22)$$

The dependence of the correlation function on  $\tau'$  shows that this is a non-stationary process. However, by setting  $z_0 = 0$  and considering the large time limit as  $t_1 \rightarrow \infty$ , the second integral term on the r.h.s of equation (3.21) tends to 0, leaving a correlation function that is entirely dependent on the time difference between  $t_1$  and  $t_2$  (time translation invariant)

$$c_{12}(|t_2 - t_1|) = \langle z(\mathbf{x}, t_1) z(\mathbf{x}, t_2) \rangle = \frac{D}{2\pi M^2} \int_0^\infty r \frac{e^{-\alpha(r)\tau}}{\alpha(r)} dr . \quad (3.23)$$

In this domain, the correlation function is a Gaussian Stationary Process and the autocorrelation function, where  $t_1 = t_2$ , is given by the constant term

$$c_{11} = c_{12}(0) = \langle z^2(\mathbf{x}, t) \rangle = \frac{D}{2\pi M^2} \int_0^\infty \frac{r}{\alpha(r)} dr . \quad (3.24)$$

By analysing this time domain, far from the initial contact point, the focus is not on the time dynamics directly following the initial contact between the cells. Instead, the time period immediately following the relaxation of the membranes in to a quasi-stable contact zone is considered, where the interplay between the membrane dynamics and the chemical potential from the bonding maintain the Gaussian Stationary Process behaviour. Figure 3.1 shows the normalised two point temporal correlation function plotted against  $\tau$ , that is independent of the thermal noise amplitude. As  $\tau \rightarrow \infty$ , there is a slow convergence and the correlation function asymptotically approaches zero. Attempts to obtain a closed solution for the integral equation (3.23) have proved unfruitful (see appendix D) and subsequently an asymptotic approximation is developed in chapter 4, to analyse the behaviour as  $\tau \rightarrow \infty$ .

### 3.1.4 Scaling Approach

A traditional scaling approach to determine the *growth*, *roughening* and *dynamical scaling* exponents would determine if the interface  $z(\mathbf{x}, t)$  is self-affine (Barabasi and Stanley, 1995).

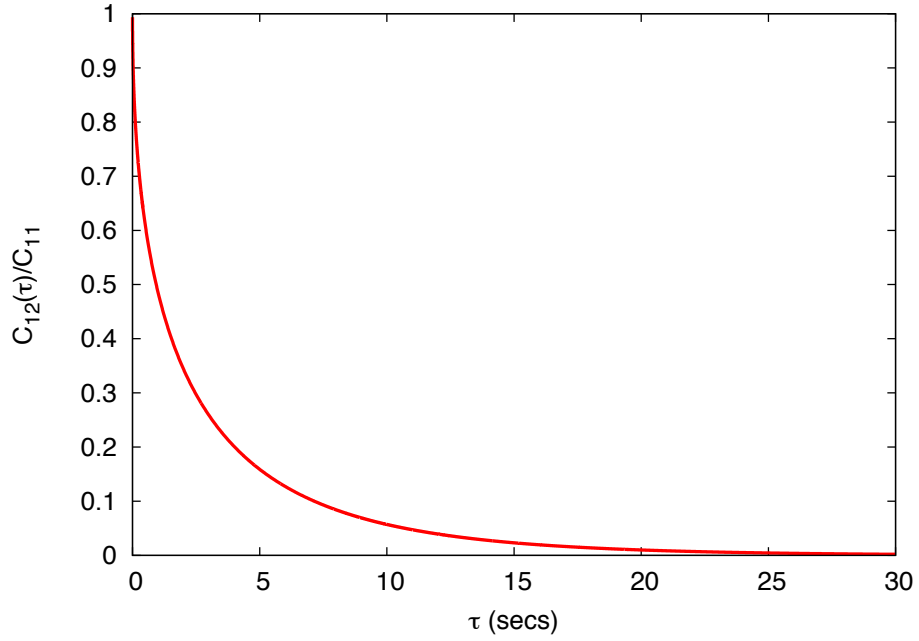


Figure 3.1: **The large time Gaussian stationary process temporal correlation length.** The two point temporal correlation is scaled by the autocorrelation length.

In this case, through rescaling an interface that is statistically equivalent to the unscaled interface can be obtained. For the purposes of this section only,  $\phi(\mathbf{x}, t) = z(\mathbf{x}, t)$  is used for the local separation distance in equation (3.1a), in order to retain the variable  $z$  for the dynamic exponent (as is commonly used in the literature). Rescaling in the spatial dimensions, time dimension and intermembrane separation distance relies on the introduction of the scaled variables

$$\mathbf{x} \mapsto \mathbf{x}' \equiv b\mathbf{x} \quad (3.25)$$

$$t \mapsto t' \equiv b^z t \quad (3.26)$$

$$\phi \mapsto \phi' \equiv b^\alpha \phi \quad (3.27)$$

whereupon equation (3.1a) can be expressed as

$$Mb^{\alpha-z} \frac{\partial \phi(\mathbf{x}, t)}{\partial t} = -Bb^{\alpha-4} \nabla^4 \phi(\mathbf{x}, t) + \gamma b^{\alpha-2} \nabla^2 \phi(\mathbf{x}, t) - \lambda b^\alpha \phi(\mathbf{x}, t) + b^{-\frac{d+z}{2}} \eta(\mathbf{x}, t) \quad (3.28)$$

and so

$$M \frac{\partial \phi(\mathbf{x}, t)}{\partial t} = -Bb^{z-4} \nabla^4 \phi(\mathbf{x}, t) + \gamma b^{z-2} \nabla^2 \phi(\mathbf{x}, t) - \lambda b^z \phi(\mathbf{x}, t) + b^{\frac{z-d}{2}-\alpha} \eta(\mathbf{x}, t). \quad (3.29)$$

To find the correct exponents  $z$ ,  $\alpha$  and subsequently  $\beta = \alpha/z$ , the equation (3.1a) must remain invariant under the rescaling (3.29). Each of the four terms has a distinct exponent and there are only 2 unknowns, therefore the system is overdetermined and it has no solution. However,

the scaling behaviour can be analysed when different terms are forced to be invariant under the transformation. Consider the following scenarios

- The rigidity term  $\nabla^4\phi$  is invariant when  $z = 4$ .  
 Rendering the noise term invariant, this then leads to  $\alpha = \frac{4-d}{2}$  and  $\beta = \frac{4-d}{8}$ .  
 In this case, the remaining terms scale like  $b^2\nabla^2\phi$  and  $b^4\lambda\phi$ . Then, in the hydrodynamic limit, as  $b \rightarrow \infty$  the  $\lambda\phi$  term dominates.
- The surface tension term  $\nabla^2\phi$  is invariant when  $z = 2$ .  
 Rendering the noise term invariant, this then leads to  $\alpha = \frac{2-d}{2}$  and  $\beta = \frac{2-d}{4}$ .  
 In this case, the remaining terms scale like  $b^{-2}\nabla^4\phi$  and  $b^2\lambda\phi$ . Again, in the hydrodynamic limit, as  $b \rightarrow \infty$  the  $\lambda\phi$  term dominates.
- The chemical potential term  $\lambda\phi$  is invariant when  $z = 1$ .  
 Rendering the noise term invariant, this then leads to  $\alpha = \frac{1-d}{2}$  and  $\beta = \frac{1-d}{2}$ .  
 In this case, the remaining terms scale like  $b^{-3}\nabla^4\phi$  and  $b^{-1}\nabla^2\phi$ . Then, in the hydrodynamic limit, as  $b \rightarrow \infty$  the first two terms on the RHS of equation (3.29) vanish to give

$$M\frac{\partial\phi(\mathbf{x},t)}{\partial t} = -\lambda\phi(\mathbf{x},t) + \eta(\mathbf{x},t) \quad (3.30)$$

While this approach is useful for the Edwards-Wilkinson equation (Edwards and Wilkinson, 1982), it is ineffectual for the linear IS model.

### 3.1.5 Independent Interval Approximation

The persistence probability of a stochastic process has been studied for a number of models including the Ising, Random Walk, Diffusion and the IS model. The *independent interval approximation* method, used to determine the time persistence, is introduced through works by Majumdar, Sire, Bray and Cornell (1996) and more recently reviewed in Bray, Majumdar and Schehr (2013). Here, a brief description is given of the method that is generic for all Gaussian processes. The stochastic variable,  $z(\mathbf{x},t)$ , with temporal correlation function  $c_{12}(t_1, t_2) = \langle z(\mathbf{x}, t_1)z(\mathbf{x}, t_2) \rangle$  as shown in equation (3.23), may be normalised

$$X(t) = \frac{z(\mathbf{x},t)}{\sqrt{\langle z(\mathbf{x},t)^2 \rangle}} \quad (3.31)$$

whereupon, the temporal correlation function is given by

$$C(t_1, t_2) = \langle X(t_1)X(t_2) \rangle = \left\langle \frac{z(\mathbf{x}, t_1)z(\mathbf{x}, t_2)}{\sqrt{\langle z(\mathbf{x}, t_1)^2 \rangle}\sqrt{\langle z(\mathbf{x}, t_2)^2 \rangle}} \right\rangle. \quad (3.32)$$

For the case considered by Majumdar, Sire, Bray and Cornell, a new time variable  $T$  is introduced, such that  $C(T_1, T_2) = f(T_1 - T_2)$ . This correlation function is time translation invariant and is expressed as a function solely dependent on the time difference between two observations, whereupon it is shown to be a Gaussian Stationary Process. Then, the “clipped” process  $\sigma(T) = \text{sgn } X(T)$  has the “clipped” correlator (Majumdar, Sire, Bray and Cornell, 1996), as shown in appendix E

$$A(T) = \langle \sigma(0)\sigma(T) \rangle = \frac{2}{\pi} \sin^{-1}(C(T)), \quad (3.33)$$

that can be used to calculate the probability density  $P(T)$ . Subsequently, the probability  $p_0(T)$  that there are no zeros of  $X(T)$  in the interval  $T$  can also be determined. Calculation of  $P(T)$  and  $p_0(T)$  enable the expression of the “clipped” correlator in terms of the mean interval length  $\langle T \rangle$  (through the small  $T$  approximation),

$$A(T) = 1 - \frac{2T}{\langle T \rangle} + \dots \quad (3.34)$$

whereupon, differentiating  $A(T)$  with respect to  $T$ , leads to the direct calculation

$$\langle T \rangle = -\frac{2}{A'(T)} \quad (3.35)$$

The basis of the method depends on the assumptions that successive crossings of the  $z = 0$  line are independent, in the limit of the interval size tending to 0. An alternative calculation was formerly presented half a century earlier by Rice (1944, 1945), that makes direct use of the correlation function,  $C(T)$ ,

$$\rho = \frac{1}{\pi} \sqrt{-C''(0)} \quad (3.36)$$

$$\langle T \rangle = \frac{1}{\rho}. \quad (3.37)$$

The method outlined in section 3.1.6 is based on this methodology, but with an important difference concerning the reflection symmetry, as detailed below.

### 3.1.6 Single-Threshold Model

The method presented in section 3.1.5 can be used to calculate the average time persistence between successive cuts of the  $z = 0$  line for a given point,  $\mathbf{x}$ , in the synaptic junction. The  $z = 0$  line represents the mean separation distance, taking in to consideration all separation distances throughout the contact zone. Given a concentration of two differing bond lengths in the synaptic junction, 15nm and 45nm, the mean separation distance will be somewhere in between these two distances, and dependent on the relative bond concentration levels. The

focus here is on the time persistence of membrane patches related to shorter TCR:pMHC bonds, where the membrane separation distance is less than the mean separation distance. To analyse this, a single threshold value is introduced,  $\Delta$ , that can be used to define a bond length at a distance  $\Delta$  from the mean separation distance. In this case, two opposing membranes are said to be within a close contact distance if the separation distance is less than  $-\Delta$  nm (Chattopadhyay and Burroughs, 2007), such that if the mean separation distance were 25 nm, then  $\Delta = 10$  nm would describe a close contact definition of 15 nm. The time persistence of this bond is then given by the length of time the separation distance remains below this threshold value.

The Gaussian Stationary nature of the linear model, demonstrated through equation (3.23), has reflection symmetry about the  $z = 0$  line. Therefore, the statistics relating to  $z(\mathbf{x}, t) \leq -\Delta$  are equivalent to the statistics for  $z(\mathbf{x}, t) \geq \Delta$ , and the latter description is used for ease of notation.

As per Majumdar, Sire, Bray and Cornell (1996), the stochastic variable is normalised, such that

$$X(t) = \frac{z(\mathbf{x}, t)}{\sqrt{\langle z(\mathbf{x}, t)^2 \rangle}} \quad (3.38)$$

and this new normalised variable has the two-point time correlation function

$$C_{12}(t_1, t_2) = \langle X(t_1)X(t_2) \rangle = \left\langle \frac{z(\mathbf{x}, t_1)z(\mathbf{x}, t_2)}{\sqrt{\langle [z(\mathbf{x}, t_1)]^2 \rangle} \sqrt{\langle [z(\mathbf{x}, t_2)]^2 \rangle}} \right\rangle = \frac{c_{12}(\tau)}{c_{11}} = C_{12}(\tau) \quad (3.39)$$

where  $c_{12}(\tau)$  is given by equation (3.23).

Then, for two variables  $X_1 = X(t_1)$  and  $X_2 = X(t_2)$ , the joint probability distribution has the probability density function

$$P(X_1, X_2) = N e^{-\frac{1}{2} \mathbf{X}^T \mathbf{C}^{-1} \mathbf{X}} \quad (3.40)$$

where  $\mathbf{X} = [X_1 \quad X_2]^T$ , the covariance matrix is given by

$$\mathbf{C} = \begin{bmatrix} 1 & C_{12}(\tau) \\ C_{12}(\tau) & 1 \end{bmatrix} \quad (3.41)$$

and  $N = \frac{1}{2\pi\sqrt{\det \mathbf{C}}}$  is the normalisation constant, ensuring

$$\int_{-\infty}^{\infty} dX_1 \int_{-\infty}^{\infty} dX_2 P(X_1, X_2) = 1 \quad (3.42)$$

Next, the determination of an expression for the ‘‘clipped’’ correlator is sought. The sign flip present in the  $\sigma$  function used by Majumdar *et al.* can be represented as a step

function, that is appropriate for analysis on a process with vertical symmetry about the  $z = 0$  line. However, the introduction of the  $\Delta$  threshold value breaks this symmetry for  $\Delta \neq 0$ , therefore the solution requires the introduction of the “clipped” step function that is 1 for close contact patches and 0 otherwise. The condition  $z(\mathbf{x}, t) \geq \Delta$  translates as  $X(t) \geq \frac{\Delta}{\sqrt{c_{11}}}$  for the normalised variable, therefore the “clipped” variable is introduced

$$\sigma(X) = \begin{cases} 1 & \text{for } X \geq \frac{\Delta}{\sqrt{c_{11}}} \\ 0 & \text{for } X < \frac{\Delta}{\sqrt{c_{11}}} \end{cases} \quad (3.43)$$

to analyse the desired region. In this case, the “clipped” correlator is given by (see appendix F)

$$A(t_1, t_2) = \frac{1}{2\pi\sqrt{\det \mathbf{C}}} \int_{\frac{\Delta}{\sqrt{c_{11}}} - C_{12}(\tau)X_1}^{\infty} dX_1 e^{-\frac{1}{2}X_1^2} \int_{\frac{\Delta}{\sqrt{c_{11}}} - C_{12}(\tau)X_1}^{\infty} du e^{-\frac{1}{2\det \mathbf{C}}u^2} \quad (3.44)$$

where  $\tau = t_2 - t_1$  and  $\det \mathbf{C}$  is the determinant of the covariance matrix  $\mathbf{C}$ .

Since the  $\tau$  dependence for the clipped correlator is realised through the two-point correlation function, the first derivative of  $A(\tau)$  with respect to  $\tau$  can be calculated using the chain rule

$$\frac{\partial A(\tau)}{\partial \tau} = \frac{\partial A(\tau)}{\partial c_{12}(\tau)} \frac{\partial c_{12}(\tau)}{\partial \tau} \quad (3.45)$$

The workings are shown in appendix F where the final form is expressed as

$$\begin{aligned} \frac{\partial A(\tau)}{\partial \tau} = & \left[ \frac{C_{12}(\tau)}{2\pi (\det \mathbf{C})^{\frac{3}{2}}} \int_{\frac{\Delta}{\sqrt{c_{11}}} - C_{12}(\tau)X_1}^{\infty} dX_1 e^{-\frac{1}{2}X_1^2} \int_{\frac{\Delta}{\sqrt{c_{11}}} - C_{12}(\tau)X_1}^{\infty} du e^{-\frac{1}{2\det \mathbf{C}}u^2} \right. \\ & + \frac{1}{2\pi\sqrt{\det \mathbf{C}}} \int_{\frac{\Delta}{\sqrt{c_{11}}} - C_{12}(\tau)X_1}^{\infty} dX_1 e^{-\frac{1}{2}X_1^2} X_1 e^{-\frac{C_{12}(\tau)}{2\det \mathbf{C}} \left( X_1 - \frac{\Delta}{C_{12}(\tau)\sqrt{c_{11}}} \right)^2} \\ & \left. - \frac{C_{12}(\tau)}{2\pi (\det \mathbf{C})^{\frac{5}{2}}} \int_{\frac{\Delta}{\sqrt{c_{11}}} - C_{12}(\tau)X_1}^{\infty} dX_1 e^{-\frac{1}{2}X_1^2} \int_{\frac{\Delta}{\sqrt{c_{11}}} - C_{12}(\tau)X_1}^{\infty} du u^2 e^{-\frac{1}{2\det \mathbf{C}}u^2} \right] \\ & \times \frac{-D}{2\pi c_{11} M^2} \int_0^{\infty} r e^{-\alpha(r)\tau} dr \quad (3.46) \end{aligned}$$

Figure 3.2 shows the plot of  $\langle \tau \rangle$  (using equations (3.35) and (3.46)) against  $\Delta$ .

## 3.2 Numerical Methods

In order to obtain a numerical solution of the linear separation distance model, the spatial and time dimensions in equation (3.1) are discretized using a finite difference scheme, to approximate the derivatives at discrete sample points. Section 3.2.1 describes the mapping of the continuous space and time dimensions on to a discrete set of sample points. In

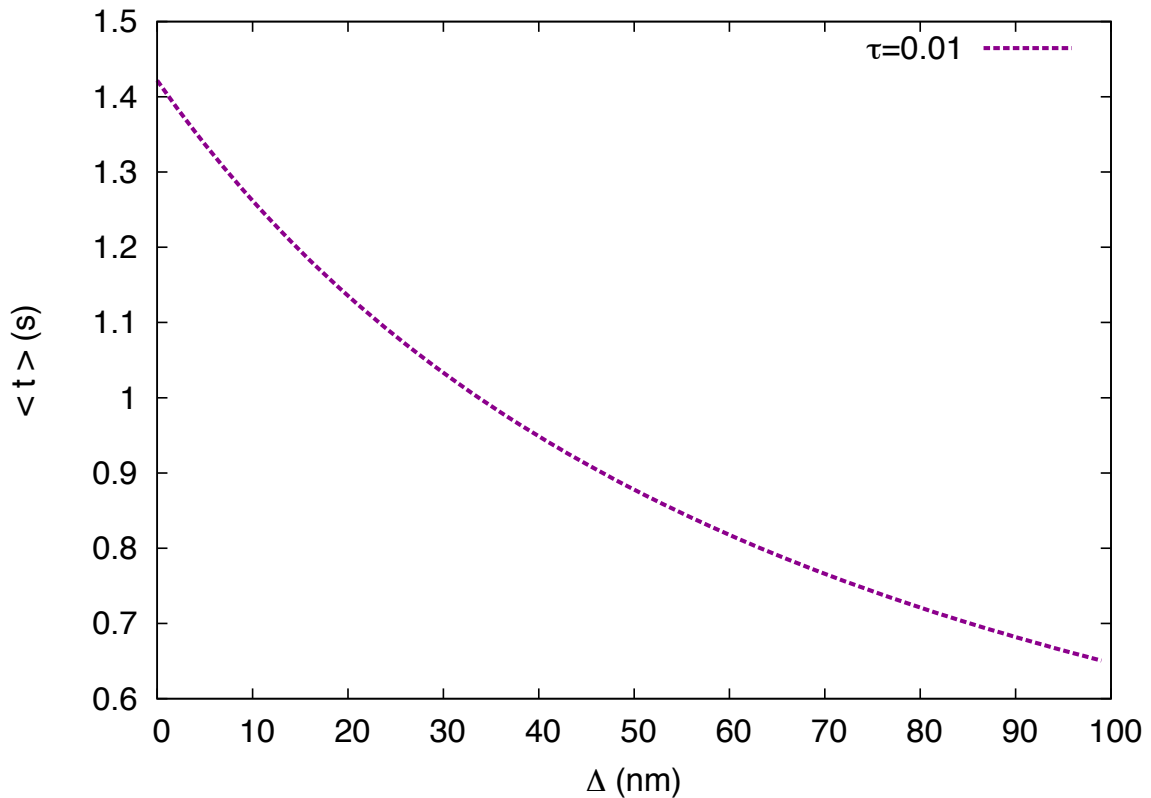


Figure 3.2:  $\langle \tau \rangle$  plotted against  $\Delta$ . The correlation function  $c_{12}(\tau)$  was calculated for  $\tau = 0.01$ . Changing the value of  $\tau$  in the correlation function has the effect of vertically rescaling the mean interval length  $\langle \tau \rangle$ , but the qualitative picture remains unchanged.

section 3.2.2, the finite difference equations for approximating the derivative terms in the Langevin equation are defined, along with the explicit forward Euler representation. And finally, section 3.2.3 gives an outline of the method used to collect ensemble statistics during computer simulations.

### 3.2.1 Discretisation

Consider an area of membrane in the synaptic junction that is described in the Cartesian coordinate system by length  $X$  in the  $x$ -direction and  $Y$  in the  $y$ -direction. The area can be discretized using  $N$  regularly spaced intervals of size  $\Delta x$  in the  $x$ -dimension to describe the range 0 to  $X$ . Similarly, the  $y$  dimension is discretized using  $M$  intervals of size  $\Delta y$  to describe the range 0 to  $Y$ . The membrane area can then be represented as a grid with discrete sample points defined as

$$x_{n,m} = (n\Delta x, m\Delta y) \quad (3.47)$$

where  $n = 0, 1, \dots, N$  and  $m = 0, 1, \dots, M$ . Similarly, the time dimension may be discretized using regular intervals such that the discrete time points are given by  $t_k = k\Delta t$ , where  $\Delta t$  is the temporal step size.

Using this discretization scheme, the local membrane separation distance and the noise term at the discrete point  $x_{n,m}$ , at time  $t_k$ , can be expressed using the subscript notation

$$z_{n,m,k} = z(x_{n,m}, t_k) \quad (3.48)$$

$$\eta_{n,m,k} = \eta(x_{n,m}, t_k). \quad (3.49)$$

The second moment for the noise term, equation (3.1c), can then be approximated in the discrete domain by

$$\langle \eta(x_{n,m}, t_k) \eta(x_{n',m'}, t_{k'}) \rangle = 2D \delta(\Delta x(n - n')) \delta(\Delta y(m - m')) \delta(\Delta t(k - k')) \quad (3.50)$$

$$= \frac{2D}{\Delta x \Delta y \Delta t} \delta(n - n') \delta(m - m') \delta(k - k') \quad (3.51)$$

and subsequently a scaling factor of  $\sqrt{\frac{2D}{\Delta x \Delta y \Delta t}}$  is applied to the random noise variable drawn from a Gaussian distribution with unit variance, that is used to represent the thermal noise.

### 3.2.2 Finite Difference Approximations and Time Evolution

Using the discrete representation from section 3.2.1 the Taylor series expansion can be used to derive the central difference approximations for the spatial derivatives in equation (3.1).

The second order Laplacian term can be approximated by

$$\nabla^2 z(x_{n,m}, t_k) = \frac{z_{n+1,m,k} - 2z_{n,m,k} + z_{n-1,m,k}}{(\Delta x)^2} + \frac{z_{n,m+1,k} - 2z_{n,m,k} + z_{n,m-1,k}}{(\Delta y)^2} \quad (3.52)$$

and fourth order derivative can be approximated by

$$\begin{aligned} \nabla^4 z(x_{n,m}, t_k) &= \frac{z_{n+2,m,k} - 4z_{n+1,m,k} + 6z_{n,m,k} - 4z_{n-1,m,k} + z_{n-2,m,k}}{(\Delta x)^4} \\ &+ \frac{z_{n,m+2,k} - 4z_{n,m+1,k} + 6z_{n,m,k} - 4z_{n,m-1,k} + z_{n,m-2,k}}{(\Delta y)^4} \\ &+ \frac{2(z_{n+1,m+1,k} + z_{n+1,m-1,k} + z_{n-1,m+1,k} + z_{n-1,m-1,k})}{(\Delta x)^2(\Delta y)^2} \\ &- \frac{4(z_{n+1,m,k} + z_{n-1,m,k} + z_{n,m+1,k} + z_{n,m-1,k})}{(\Delta x)^2(\Delta y)^2} \\ &+ \frac{8z_{n,m,k}}{(\Delta x)^2(\Delta y)^2} \end{aligned} \quad (3.53)$$

The synaptic junction may be considered as a large (infinite) sized system, that is modelled using a small patch of membrane, whereupon periodic boundary conditions may be assumed. Periodic boundary conditions can be implemented by “wrapping” the derivatives across the boundary. For example, the Laplacian term at the point  $(n = 1, m = 0)$  on the membrane,

at time  $t_k$ , can be approximated by

$$\nabla^2 z(x_{1,0}, t_k) = \frac{z_{2,0,k} - 2z_{1,0,k} + z_{0,0,k}}{(\Delta x)^2} + \frac{z_{1,1,k} - 2z_{1,0,k} + z_{1,M,k}}{(\Delta y)^2} . \quad (3.54)$$

Finally, the derivative with respect to time can be approximated using the forward difference equation

$$\frac{\partial z(x_{n,m}, t_k)}{\partial t} = \frac{z_{n,m,k+1} - z_{n,m,k}}{\Delta t} . \quad (3.55)$$

Using equations (3.52), (3.53) and (3.55) (with equations (3.54) and the fourth order equivalent applied at the boundaries), the linear IS model described by equation (3.1) can be numerically solved using the simple Euler integration method. The time evolution is then given by

$$z_{n,m,k+1} = z_{n,m,k} + \Delta t F(z_{n,m,k}) + \frac{1}{M} \sqrt{\frac{2D\Delta t}{\Delta x \Delta y}} \zeta_{n,m,k} \quad (3.56)$$

where

$$F(z_{n,m,k}) = -\frac{B}{M} \nabla^4 z_{n,m,k} + \frac{\gamma}{M} \nabla^2 z_{n,m,k} - \frac{\lambda}{M} z_{n,m,k} \quad (3.57)$$

and  $\zeta$  is a random variable drawn from a Gaussian distribution with unit variance. In practise, the Box-Müller algorithm is used to generate the values for  $\zeta$  (Press, Teukolsky, Vetterling and Flannery, 2005).

The stability of the Simple Euler method depends on the values of the time step size and the discrete step size used in the spatial dimensions. The two-dimensional Laplacian is stable when

$$\frac{\Delta t}{\Delta x \Delta y} \leq \frac{1}{4} \quad (3.58)$$

and by fixing  $\Delta x = \Delta y = 1$ , the stability is managed through the choice of  $\Delta t$ .

The core structure relies on a version of Stratonovich calculus (Risken, 1989) in order to avoid explicit multiplicative noise in the basic model, in conformity with most biological models of this genre (Qi *et al.*, 2001; Burroughs and Wülfing, 2002). The Runge-Kutta order 4 method was used for the validation of the Eulerian scheme and the simulation results remained unaffected by the choice of method.

Given thermal fluctuations arising from the reaction kinetics for the binding surface proteins, the membrane dynamics over time are simulated through the time-evolution of the discrete model, equation (3.56). Periodic boundary conditions are used and the initial conditions for the simulations were chosen to represent a positioning of the membrane away from the steady-state configuration. Figure 3.3 shows the time evolution of the local membrane separation distance for a fixed point on the membrane, starting from an initial separation distance of 100 nm, for a range of time steps used in the numerical integration. All values of  $\Delta t$  follow a similar initial relaxation trajectory, with the Gaussian Stationary Process ev-

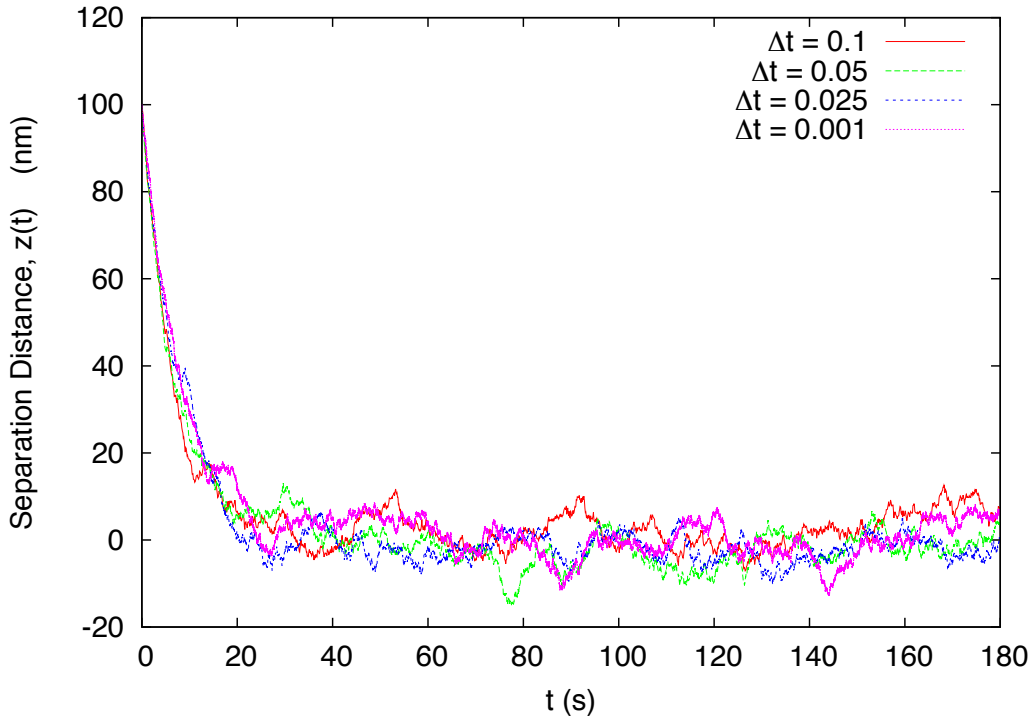


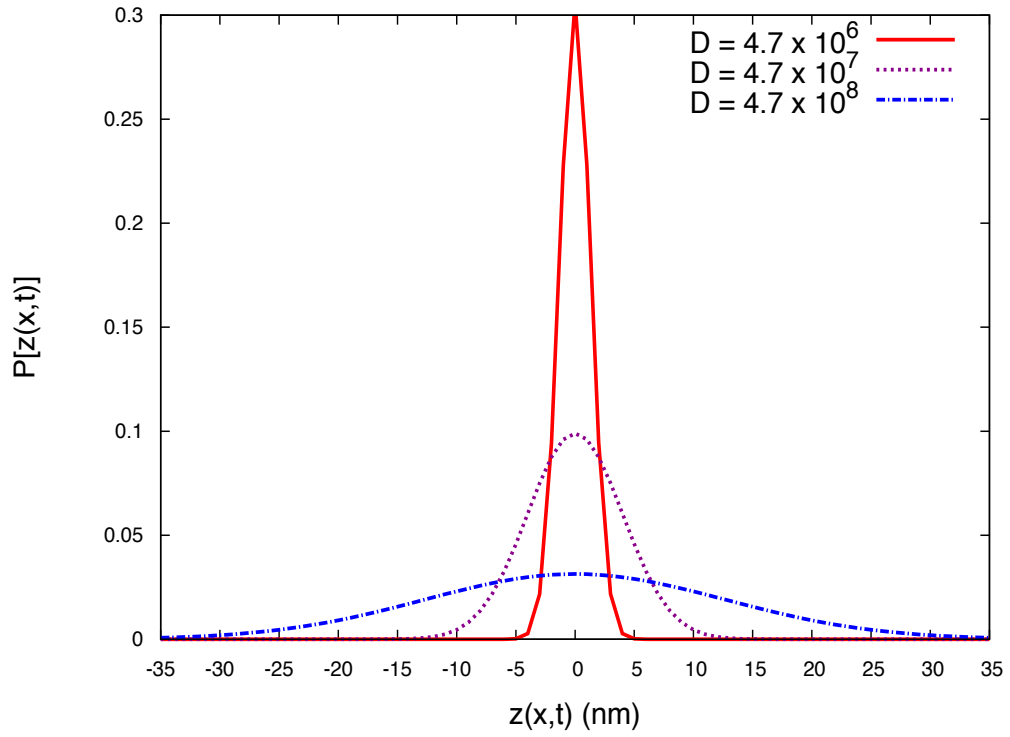
Figure 3.3: **The simulated time evolution of the local membrane separation distance.** The membrane separation distance simulated over time using finite difference methods, for a fixed point  $\mathbf{x}$  on the membrane, with initial condition  $z(\mathbf{x}, 0) = 100$  nm. The separation distance relaxes to a steady-state, fluctuating about  $z = 0$ . The relaxation trajectory and magnitude of fluctuations are consistent for different values of  $\Delta t$ .

ident after  $\sim 20$  seconds. The fluctuations are of the same magnitude for all  $\Delta t$ , due to the rescaling constant used in the thermal noise term.

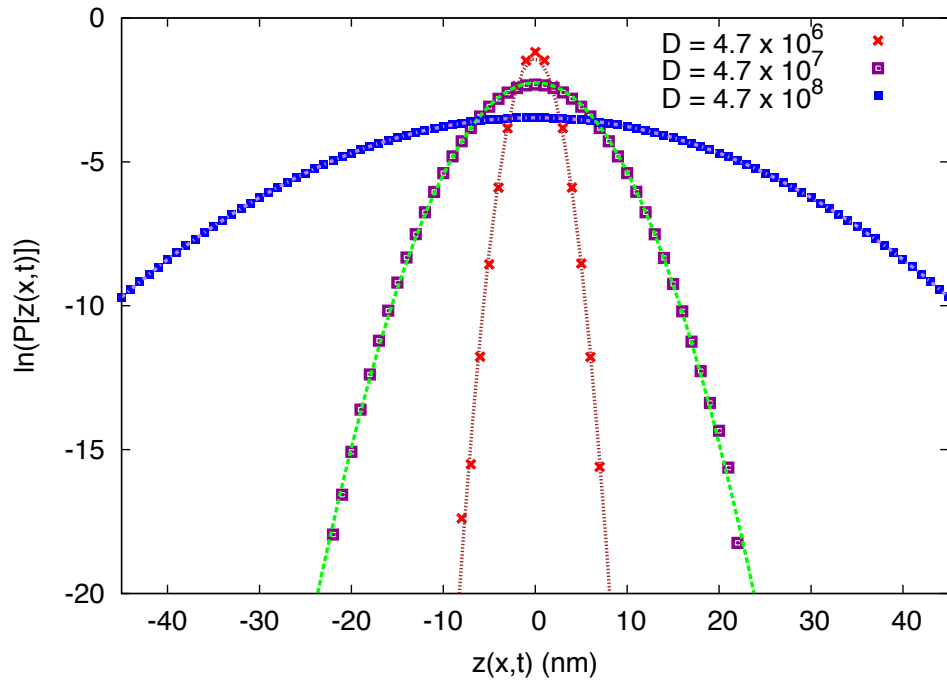
The delta correlated noise strength in equation (3.1c),  $D$ , determines the strength of the thermal fluctuations. Using the model parameter values in table 2.2, a range of  $D$  values were used in simulations to determine the observed deviations of membrane fluctuations about the mean. Figure 3.4 shows the probability density distribution for  $z(\mathbf{x}, t)$  generated from numerical simulations, comparing three different thermal noise strengths. Using the parameter values in table 2.2, the local membrane separation distance fluctuations are of the nanometric scale. Figure 3.4(b) shows a good parabola fit to the natural logarithm of the probability density, indicating a Gaussian structure for the probability density function.

### 3.2.3 Numerical Simulation of the Single-Threshold Model

In this section the numerical implementation of the single-threshold model, as described in section 3.1.6, is outlined. The solution to equation (3.1) is the stochastic variable  $z(\mathbf{x}, t)$  that is a Gaussian Stationary Process fluctuating about  $z = 0$ , as shown in section 3.2.2. Figure 3.5(a) shows simulation results for  $z(\mathbf{x}, t)$ , at a fixed point on the membrane, during a sample time frame. The two different values of the noise strength,  $D$ , display the effect of increasing/decreasing the thermal fluctuations, that corresponds to a Gaussian Stationary



(a)



(b)

Figure 3.4: **The probability density of the local membrane separation distance, extracted from numerical simulations using three different thermal noise strengths.** Panel 3.4(a) shows the probability density for  $z(\mathbf{x}, t)$ . The probability density is centred around 0 and the width increases as the magnitude of the thermal noise increases. Panel 3.4(b) shows the probability density function plotted in the natural log scale (data points), with parabolic curves fitted (lines) to show the Gaussian nature.

Process with a larger/smaller amplitude. This implies higher values of thermal noise increase the probability of crossing larger  $\Delta$  values.

A schematic illustration of the method used to determine the bond time persistence instances is shown in figure 3.5(b). The  $t_{-\Delta}^-$  regions correspond to the length of time a bond (with length  $\Delta$  from the mean separation distance) persists and are calculated as the time  $z(\mathbf{x}, t)$  spends below the  $-\Delta$  threshold.  $z(\mathbf{x}, t)$  is statistically symmetrical about  $\Delta = 0$ , but for  $\Delta \neq 0$  the symmetry in the  $z$  direction is broken, whereupon the statistics below  $-\Delta$  are different from the statistics above  $-\Delta$ . In this case, the persistence above  $-\Delta$  would indicate the time duration where no bonding is taking place. However, in accordance with the statistical symmetry of the Gaussian Stationary Process about  $\Delta = 0$ , the statistics for  $z(\mathbf{x}, t) < -\Delta$  are equivalent to the statistics for  $z(\mathbf{x}, t) > \Delta$ . A  $t_{\Delta}^+$  region is defined as a time interval between two successive crossings of the  $z = \Delta$  line, where  $z(\mathbf{x}, t)$  remains above  $\Delta$ . In this case,  $z(\mathbf{x}, t)$  enters the region from below the  $\Delta$  line and  $t_{\Delta}^+$  is the time taken to return below the  $\Delta$  threshold. Then, each instance of time persistence is given by  $t_{\Delta}^+ = t_2 - t_1$ , where

$$\begin{aligned} z(\mathbf{x}, t_1) &= z(\mathbf{x}, t_2) = \Delta \\ z(\mathbf{x}, t) &\geq \Delta, \quad t_1 < t < t_2. \end{aligned} \tag{3.59}$$

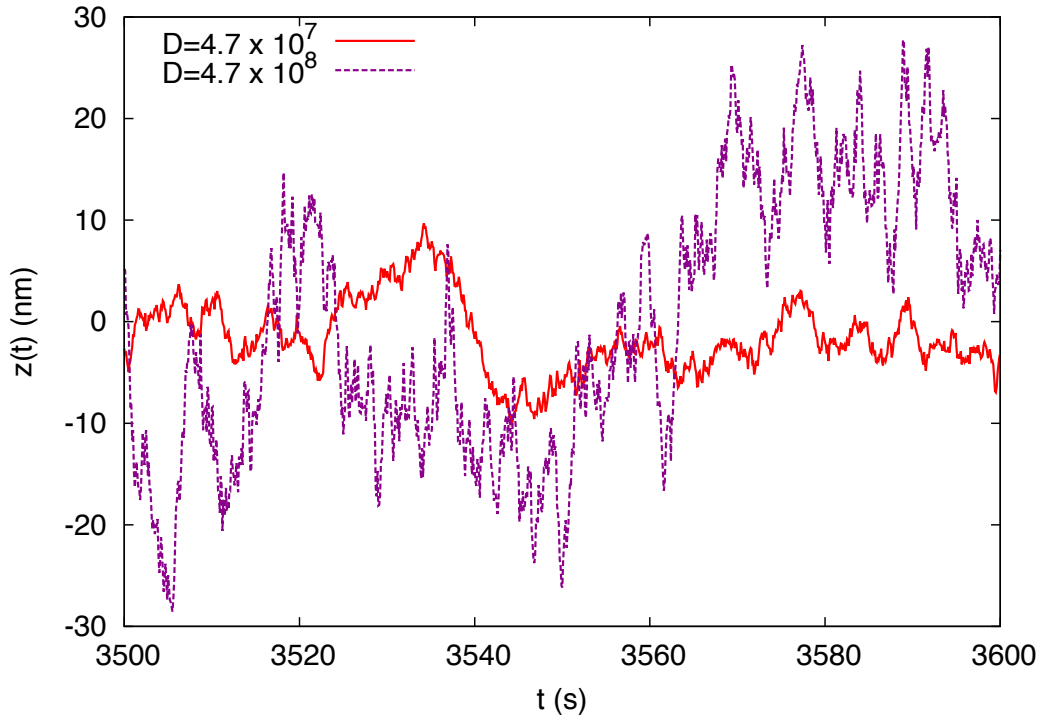
Using the discrete notation of section 3.2.1, if the separation distance at some point  $x_{n,m}$  on the membrane crosses the threshold from below at  $z_{n,m,k}$ , then the index  $k$  is stored in memory until the separation distance crosses back over the  $\Delta$  threshold at some future point  $z_{n,m,k+j}$ . Then, the time persistence above the  $\Delta$  threshold is given by  $t_{\Delta}^+ = j\Delta t$ , where  $\Delta t$  is the integration time step.

The different instances of time persistence are assumed to be statistically independent via the *independent interval approximation* (Bray, Majumdar and Schehr, 2013; Majumdar, Sire, Bray and Cornell, 1996). Then, the average time persistence is given by the statistical average

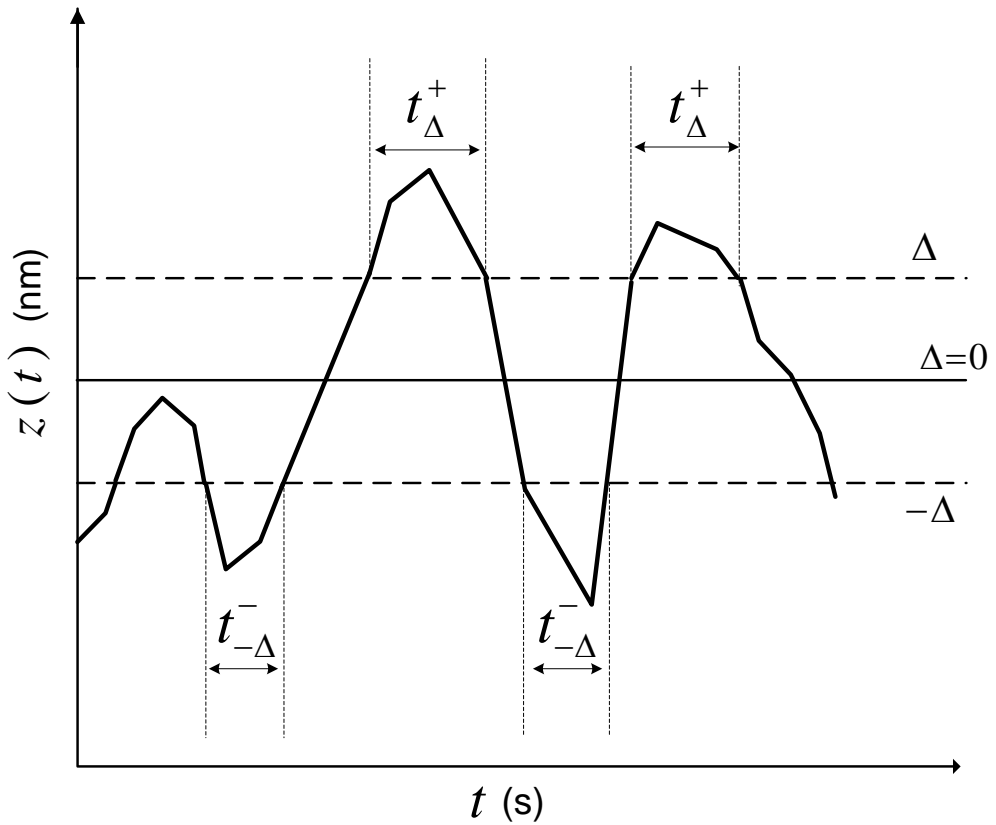
$$\langle t_{\Delta}^+ \rangle = \frac{1}{T} \sum_{i=1}^T t_{\Delta}^{+(i)} \tag{3.60}$$

where  $t_{\Delta}^{+(i)}$  is the  $i$ th instance of time persistence above  $\Delta$  and  $T$  is the total number of instances recorded for all points  $x_{n,m}$  over the simulated time range. In the following analysis the ‘+’ is dropped for ease of notation, where it is assumed  $t_{\Delta}$  is the time persistence above  $\Delta$ .

The probability density of the  $t_{\Delta}$  instances is recorded by maintaining a frequency distribution of the various  $t_{\Delta}^{(i)}$  lengths. For large enough statistics, this normalised frequency distribution is equivalent to the probability density for  $t_{\Delta}$ . Then the probability that the



(a)



(b)

Figure 3.5: **Examples of simulated solutions for the separation distance and the time persistence definition.** Figure 3.5(a) shows the simulated time dependent solution for  $z(\mathbf{x}, t)$  using two different delta correlated noise strengths and 3.5(b) shows a schematic illustration of the  $t_{-\Delta}^-$  and  $t_{\Delta}^+$  regions that represent persistent bonds.

time persistence is equal to or less than  $\tau$  is given by  $P(t_\Delta \leq \tau)$ , with  $P(t_\Delta \leq \infty) = 1$ . For discrete  $P$ , the probability density can be expressed as a sum of Dirac- $\delta$  functions

$$W_\Delta(\tau) = \sum_{m=1}^{\infty} p_m^\Delta \delta(\tau - \tau_m) \quad (3.61)$$

where  $\tau_m$  are multiples of  $\Delta t$  and  $p_m^\Delta$  is the first passage probability density associated with  $\tau_m$  for a given  $\Delta$  value (Krug *et al.*, 1997). The persistence (survival) probability is then identified through the first passage statistics of the fluctuating interface

$$P_\Delta(\tau) = 1 - \int_0^\tau W_\Delta(\tau') d\tau' \quad (3.62)$$

A major emphasis of this study is to analyse the effect of extremal values on the time persistence calculated using this statistical average technique, as has often been shown to be of great importance in understanding the expected variation between the theoretical analysis presented and analogous biological experiments (Chattopadhyay and Burroughs, 2007; Bush and Chattopadhyay, 2014). As an example of the latter type, quite often in the nanospectroscopy of flagellar dynamics, for example sperm (Hilfinger, Chattopadhyay and Jülicher, 2009; Bayly and Wilson, 2014), ensemble averaging is a serious issue due to the perceived lack of ergodicity in such dynamics. Technically, what this will imply is an understanding of the role of the long tail in the  $P_\Delta(\tau)$  probability distribution profile, as defined in equation (3.62). The results shown in chapter 6, surprisingly indicate that high frequency nodes, the generator of extremal value statistics, return negligible contribution to the ensemble statistics.

## Chapter 4

# Asymptotic Analysis Applied to the Temporal Correlation Function

The essence of this chapter lies in the understanding that the presence of the  $\nabla^4 z$  term in the membrane kinetics annuls the possibility of an exact closed form non-integral solution of the two-point correlation function (cf. appendix D for a trial using the *residue theorem*). However, asymptotic analysis can be employed to determine an approximation for the correlation function, as  $\tau \rightarrow \infty$ . Section 4.1 shows the derivation of the asymptotic solution using Laplace's Method and section 4.2 details the same derivation using the Saddle Point Method. Both methods are detailed in Murray (1974) and the analysis that follows performs the same logical steps as those presented in this work.

### 4.1 Laplace's Method

Laplace's method can be used for integral equations of the form

$$f(\tau) = \int_0^\infty g(k) e^{h(k)\tau} dk . \quad (4.1)$$

The temporal correlation function has the same functional form as equation (4.1), if the following functional mapping is used

$$g(k) = \frac{D}{2\pi M^2} \left( \frac{Mk}{Bk^4 + \gamma k^2 + \lambda} \right) \quad (4.2)$$

$$h(k) = -\frac{Bk^4 + \gamma k^2 + \lambda}{M} . \quad (4.3)$$

As  $\tau \rightarrow \infty$ , the dominant term in the integral equation (4.1) comes from the immediate vicinity of the maximum of  $h(k)$ . The stationary points for  $h(k)$  occur at the points where

the first derivative is zero, such that

$$\frac{\partial h(k)}{\partial k} = -\frac{k(4Bk^2 + 2\gamma)}{M} = 0. \quad (4.4)$$

In this case, values of  $k = 0$  or  $k^2 = -\gamma/2B$  describe the turning points, with the latter describing purely imaginary solutions, that are considered through the application of the saddle-point method in section 4.2. The stationary point with a real solution for  $\partial h(k)/\partial k = 0$  occurs at  $k = 0$ , where  $h(0) = -\frac{\lambda}{M}$ . Now  $h(k) < h(0)$  for  $0 < k < \infty$  and  $h''(0) = -2\gamma/M < 0$ , therefore  $h(k)$  is a maximum at  $k = 0$  and the Taylor expansion about  $k = 0$  can be expressed as

$$h(k) = h(0) + h'(0)k + \frac{h''(0)}{2!}k^2 + \frac{h'''(0)}{3!}k^3 + \frac{h''''(0)}{4!}k^4, \quad (4.5)$$

where the expansion terminates  $\mathcal{O}(k^4)$ , since  $h^n(k) = 0$  for  $n > 4$ . It is also noted that  $h'(0) = 0$  and  $h'''(0) = 0$ , such that

$$h(k) - h(0) = \frac{h''(0)}{2!}k^2 + \mathcal{O}(k^4) \quad (4.6)$$

where  $h''(0) < 0$ , such that the positive real variable  $s$  may be introduced

$$h(k) - h(0) = -s^2 \quad (4.7)$$

and the exponent in the term under the integral in equation (4.1) may be written

$$e^{h(k)\tau} = e^{h(0)\tau} e^{-s^2\tau}. \quad (4.8)$$

By comparing equations (4.6) and (4.7), it is possible to represent  $k$  as a function of  $s$

$$\frac{h''(0)}{2!}k^2 + \mathcal{O}(k^4) = -s^2 \quad (4.9)$$

$$k^2 + \mathcal{O}(k^4) = -\frac{2}{h''(0)}s^2 \quad (4.10)$$

$$k = \left(-\frac{2}{h''(0)}\right)^{\frac{1}{2}} s + \mathcal{O}(s^2) \quad (4.11)$$

such that the Taylor expansion of  $g(k)$  may also be represented as a function of  $s$

$$\begin{aligned} g(k) &= g(0) + g'(0)k + \frac{g''(0)}{2!}k^2 + \mathcal{O}(k^3) \\ &= g(0) + g'(0) \left(-\frac{2}{h''(0)}\right)^{\frac{1}{2}} s + \mathcal{O}(s^2). \end{aligned} \quad (4.12)$$

The rate of change of  $k$  with respect to  $s$  can be determined from differentiating equation (4.11), to give

$$\frac{dk}{ds} = \left( -\frac{2}{h''(0)} \right)^{\frac{1}{2}} + \mathcal{O}(s) \quad (4.13)$$

and then finally, using equations (4.8), (4.12) and (4.13), the integral equation (4.1) can be approximated by the expansion

$$\begin{aligned} f(\tau) &\sim e^{h(0)\tau} g(0) \left[ \int_0^\infty \left( -\frac{2}{h''(0)} \right)^{\frac{1}{2}} e^{-s^2\tau} ds + \int_0^\infty \mathcal{O}(s) e^{-s^2\tau} ds \right] \\ &\quad + e^{h(0)\tau} g'(0) \left[ -\frac{2}{h''(0)} \int_0^\infty s e^{-s^2\tau} ds + \int_0^\infty \mathcal{O}(s^2) e^{-s^2\tau} ds \right] \\ &\quad + \int_0^\infty \mathcal{O}(s^2) e^{-s^2\tau} ds \end{aligned} \quad (4.14)$$

$$\sim e^{h(0)\tau} g(0) \left( -\frac{\pi}{2\tau h''(0)} \right)^{\frac{1}{2}} + e^{h(0)\tau} \mathcal{O} \left( \frac{1}{\tau} \right) . \quad (4.15)$$

The specific function,  $g(k)$ , required to map the temporal correlation function for the linear IS model, equation (4.2), is zero for  $g(0)$ . Therefore, the second term in the expansion containing  $g'(0) \neq 0$  is used (c.f. equation (4.14)), to give

$$f(\tau) \sim e^{h(0)\tau} g'(0) \left( -\frac{2}{h''(0)} \right) \int_0^\infty s e^{-s^2\tau} ds + \mathcal{O} \left( \tau^{-\frac{3}{2}} \right) . \quad (4.16)$$

Finally, substituting the values for  $h(0)$ ,  $g'(0)$  and  $h''(0)$ , gives the asymptotic approximation

$$f(\tau) \sim \frac{M^2}{\lambda\gamma} \tau^{-1} e^{-\frac{\lambda}{M}\tau} + \mathcal{O} \left( \tau^{-\frac{3}{2}} \right) . \quad (4.17)$$

Figure 4.1 shows a plot of the asymptotic solution (dashed line) and the integral solution (solid line), where the asymptotic solution has been scaled by a pre-factor that is derived from a least squares fit to the integral solution in the large  $\tau$  range. The asymptotic approximation is not appropriate for the range  $\tau < 30$ , where there is a marked difference between the two curves. However, a comparison of the decay rate in the large  $\tau$  region, shows a consistent decay rate for the two solutions. This is shown in figure 4.2, where the correlation function solutions are plotted against time, using a log scale for the correlation functions. This implies the asymptotic approximation may be used as an analytical alternative to the integral solution in this region.

## 4.2 Saddle Point Method

The Saddle Point Method may also be used to determine an asymptotic approximation for the integral solution. The method is similar to Laplace's Method, but is applied in the complex plane and the main steps, as described by Murray(1974), are shown below. In this case, the

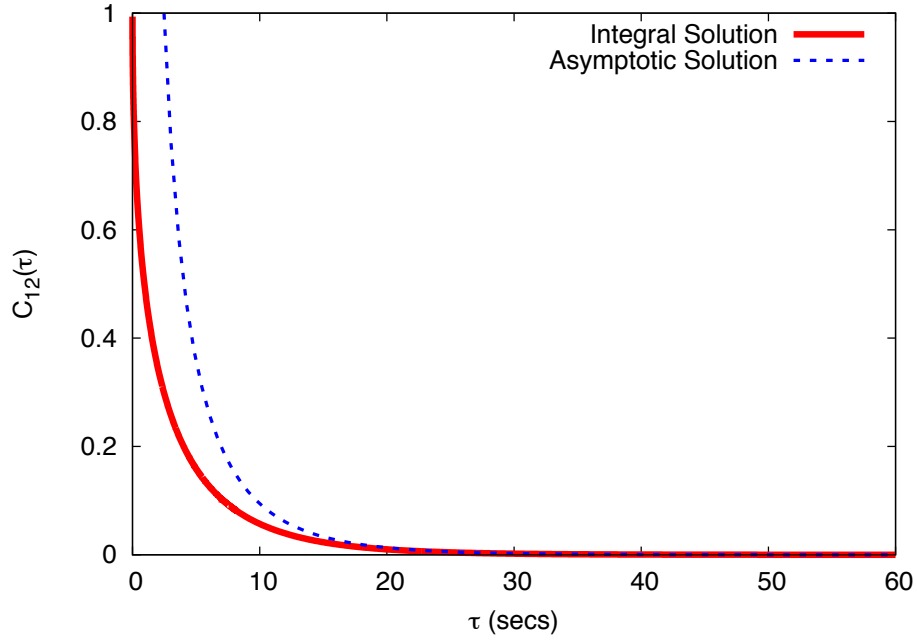


Figure 4.1: **Integral and asymptotic solution comparison for the temporal correlation function as  $\tau \rightarrow \infty$ .** The integral and asymptotic solutions are rescaled by the autocorrelation function,  $c_{11}$ .

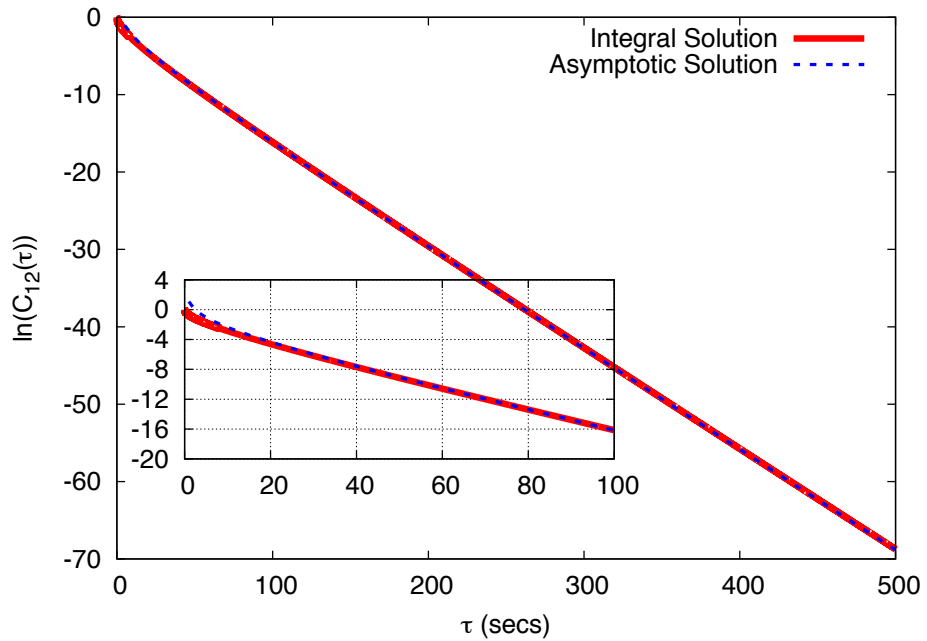


Figure 4.2: **Log comparison of the integral and asymptotic temporal correlation functions.** For the large  $\tau$  time range the exponential decay rate of the asymptotic solution is consistent with the numerical solution for the integral equation. The inset shows the decay rate closer to the  $\tau = 0$  point, where the divergence from the temporal correlation function and the asymptotic solution can be seen.

asymptotic approximation is derived for integrals of the form

$$f(\tau) = \int_C g(z) e^{h(z)\tau} dz \quad (4.18)$$

where  $z = x + iy$  and  $x, y \in \Re$ . The two-point correlation function, equation (3.23), can be expressed in the form of equation (4.18) by using the following functions

$$h(z) = -\alpha(z) = -\frac{Bz^4 + \gamma z^2 + \lambda}{M} \quad (4.19)$$

$$g(z) = \frac{D}{2\pi M^2} \frac{z}{\alpha(z)} = \frac{Dz}{2\pi M(Bz^4 + \gamma z^2 + \lambda)} \quad (4.20)$$

and then  $h(z)$  is the complex function

$$h(z) = \phi(x, y) + i\psi(x, y) \quad (4.21)$$

with the two real-valued functions given by

$$\phi(x, y) = -\frac{B(x^4 + y^4 - 6x^2y^2) + \gamma(x^2 - y^2) + \lambda}{M} \quad (4.22a)$$

$$\psi(x, y) = -\frac{4B(x^3y - xy^3) + 2xy\gamma}{M}. \quad (4.22b)$$

It can be shown that these equations satisfy the Cauchy-Riemann equations

$$\frac{\partial \phi}{\partial x} = \frac{\partial \psi}{\partial y} = -\frac{4Bx^3 - 12Bxy^2 + 2\gamma x}{M} \quad (4.23a)$$

$$\frac{\partial \phi}{\partial y} = -\frac{\partial \psi}{\partial x} = -\frac{4By^3 - 12Bx^2y - 2\gamma y}{M} \quad (4.23b)$$

and they are potential functions that satisfy Laplace's equation

$$\frac{\partial^2 \phi}{\partial x^2} + \frac{\partial^2 \phi}{\partial y^2} = 0 \quad \text{and} \quad \frac{\partial^2 \psi}{\partial x^2} + \frac{\partial^2 \psi}{\partial y^2} = 0. \quad (4.24)$$

Consider the solution,  $z_0$ , that satisfies  $\nabla \phi = 0$ , then through the Cauchy-Riemann equations  $z_0$  is also a solution of  $\nabla \psi = 0$ . By the maximum modulus theorem,  $\phi$  and  $\psi$  cannot have a maximum (or minimum) in the domain of analyticity of  $h(z)$ . Therefore, the solution  $z_0$  is a saddle-point of both  $\phi$  and  $\psi$ , and hence, a saddle-point of  $h(z)$ . The aim is to find solutions for  $h(z)$ , where  $h'(z_0) = 0$  and  $h''(z_0) \neq 0$ . The first derivative of  $h$  with respect to  $z$  is given by

$$h'(z) = \hat{\phi}(x, y) + i\hat{\psi}(x, y) \quad (4.25)$$

where

$$\hat{\phi}(x, y) = -\frac{4B(x^3 - 3xy^2) + 2\gamma x}{M} \quad (4.26a)$$

$$\hat{\psi}(x, y) = -\frac{4B(3x^2y - y^3) + 2\gamma y}{M}. \quad (4.26b)$$

Then, the stationary points exist where  $\hat{\phi}(x_0, y_0) = 0$  and  $\hat{\psi}(x_0, y_0) = 0$ . Solving the simultaneous equations that arise at the turning points leads to the following solutions

$$x = 0, \quad y = 0 \quad (4.27a)$$

$$x = 0, \quad y = \pm\sqrt{\frac{\gamma}{2B}} \quad (4.27b)$$

$$x = \pm\frac{i}{2}\sqrt{\frac{\gamma}{2B}}, \quad y = \pm\frac{1}{2}\sqrt{\frac{\gamma}{2B}} \quad (4.27c)$$

$$x = \pm i\sqrt{\frac{\gamma}{2B}}, \quad y = 0 \quad (4.27d)$$

and ultimately the 3 distinct complex solutions

$$z_0 = 0 \quad (4.28)$$

$$z_0 = i\sqrt{\frac{\gamma}{2B}} \quad (4.29)$$

$$z_0 = -i\sqrt{\frac{\gamma}{2B}}. \quad (4.30)$$

In the region of the saddlepoint, where  $h'(z_0) = 0$ , the Taylor series for  $h(z)$  about  $z_0$  is

$$h(z) = h(z_0) + \frac{1}{2}(z - z_0)^2 h''(z_0) + \mathcal{O}((z - z_0)^3) \quad (4.31)$$

and using the definition

$$h''(z_0) = ae^{i\beta}, \quad a > 0, \quad z - z_0 = re^{i\theta}, \quad r > 0 \quad (4.32)$$

equation (4.31) can be written, using equation (4.21), as

$$\phi(x, y) + i\psi(x, y) = \phi_0 + i\psi_0 + \frac{1}{2}ar^2e^{i(2\theta+\beta)} + \mathcal{O}(r^3) \quad (4.33)$$

where  $\phi_0 = \phi(x_0, y_0)$  and  $\psi_0 = \psi(x_0, y_0)$ . The second derivative of  $h$  is given by

$$h''(z) = -\frac{12Bz^2 + 2\gamma}{M} \quad (4.34)$$

that can be evaluated for the three solutions to give

$$h''(z_0 = 0) = -\frac{2\gamma}{M} \quad (4.35)$$

$$h''(z_0 = \pm i\sqrt{\frac{\gamma}{2B}}) = \frac{4\gamma}{M}. \quad (4.36)$$

It is noted that  $h''(z_0)$  is a purely *real-valued* function for all three solutions. Thus,  $\beta = 0$  such that the real part of equation (4.33) is given by

$$\phi = \phi_0 + \frac{1}{2}ar^2 \cos(2\theta) + \mathcal{O}(r^3). \quad (4.37)$$

Then, there are two orthogonal lines which are solutions of  $\frac{1}{2}ar^2 \cos(2\theta) = 0$ , namely

$$\theta = \frac{\pi}{4} \text{ and its continuation } \theta = \pi + \frac{\pi}{4}$$

and

$$\theta = -\frac{\pi}{4} \text{ and its continuation } \theta = \pi - \frac{\pi}{4}$$

that correspond to two ranges of  $\theta$  around  $z_0$  where  $\phi < \phi_0$ ,  $\frac{\pi}{4} < \theta < \frac{3\pi}{4}$  and  $\frac{5\pi}{4} < \theta < \frac{7\pi}{4}$ . Similarly, equating the imaginary parts, the two curves  $\psi = \psi_0$  where  $\phi$  changes most rapidly, are described by the solutions to  $\sin(2\theta)$ , namely

$$\theta = 0 \text{ and its continuation } \theta = \pi$$

and

$$\theta = -\frac{\pi}{2} \text{ and its continuation } \theta = \pi - \frac{\pi}{2}.$$

The contour  $C$  is then deformed to lie along the steepest descent path where  $\psi = \psi_0$ , whereupon

$$\phi - \phi_0 = h(z) - h(z_0) = \frac{1}{2}(z - z_0)^2 h''(z_0) < 0. \quad (4.38)$$

The next step involves the introduction of a new real-valued variable,  $\varepsilon$ , such that

$$h(z) - h(z_0) = -\varepsilon^2, \quad \varepsilon \text{ real} \quad (4.39)$$

whereupon equation (4.18) can now be written as

$$f(\tau) = e^{\tau h(z_0)} \int_{\varepsilon_a}^{\varepsilon_b} e^{-\tau \varepsilon^2} g(z(\varepsilon)) \frac{dz}{d\varepsilon} d\varepsilon. \quad (4.40)$$

Finally, Watson's lemma is used to write the asymptotic expansion as

$$f(\tau) \sim e^{\tau h(z_0)} \int_0^\infty e^{-\tau \varepsilon^2} g(z(\varepsilon)) \frac{dz}{d\varepsilon} d\varepsilon, \quad \tau \rightarrow \infty. \quad (4.41)$$

To determine  $z$  as a function of  $\varepsilon$ , equation (4.39) is used and  $h(z)$  expanded as a Taylor series about  $z_0$

$$\frac{1}{2} (z - z_0)^2 h''(z_0) + \mathcal{O}((z - z_0)^3) = -\varepsilon^2 \quad (4.42)$$

leading to

$$z - z_0 = \left\{ \frac{-2}{h''(z_0)} \right\}^{\frac{1}{2}} \varepsilon + \mathcal{O}(\varepsilon^2). \quad (4.43)$$

Then,  $g(z(\varepsilon))$  can be presented as a power series

$$g(z(\varepsilon)) = g(z_0) + (z - z_0)g'(z_0) + \dots \quad (4.44)$$

$$= g(z_0) + g'(z_0) \left\{ \frac{-2}{h''(z_0)} \right\}^{\frac{1}{2}} \varepsilon + \mathcal{O}(\varepsilon^2) \quad (4.45)$$

and equation (4.41) can be written

$$f(\tau) \sim e^{\tau h(z_0)} g(z_0) \left\{ \frac{-2}{h''(z_0)} \right\}^{\frac{1}{2}} \int_0^\infty e^{-\tau \varepsilon^2} d\varepsilon + \dots \quad (4.46)$$

$$= e^{\tau h(z_0)} g(z_0) \left\{ \frac{-\pi}{2\tau h''(z_0)} \right\}^{\frac{1}{2}} + \mathcal{O}\left(\frac{e^{\tau h(z_0)}}{\tau}\right). \quad (4.47)$$

Each of the stationary points, equations (4.28)-(4.30) has a different asymptotic form, depending on the values of  $h(z)$ ,  $g(z)$  and  $h''(z)$  at the stationary point. Comparing the different solution values for  $h(z_0)$

$$h(z_0 = 0) = -\frac{\lambda}{M} \quad (4.48a)$$

$$h\left(z_0 = i\sqrt{\frac{\gamma}{2B}}\right) = \frac{\gamma^2 - 4B\lambda}{4BM} \quad (4.48b)$$

$$h\left(z_0 = -i\sqrt{\frac{\gamma}{2B}}\right) = \frac{\gamma^2 - 4B\lambda}{4BM} \quad (4.48c)$$

and noting all the parameter values are positive, it can be seen the complex conjugate imaginary solutions have a greater value for  $h(z)$  than the real-valued solution,  $z = 0$ . However,

the second derivative of  $h(z)$  calculated for each solution

$$h''(z_0 = 0) = -\frac{2\lambda}{M} \quad (4.49a)$$

$$h''\left(z_0 = i\sqrt{\frac{\gamma}{2B}}\right) = \frac{4\gamma}{M} \quad (4.49b)$$

$$h''\left(z_0 = -i\sqrt{\frac{\gamma}{2B}}\right) = \frac{4\gamma}{M} \quad (4.49c)$$

shows the stationary points associated with the imaginary solutions represent a minimum in the respective regions. In this case, the  $z = 0$  solution represents the dominant term in the integral and the final steps to produce the asymptotic form follows the analysis in section 4.1 to give

$$f(\tau) \sim \frac{D}{4\pi\gamma^2} \tau^{-1} e^{-\frac{\gamma}{M}\tau} \quad (4.50)$$

which has the same form as that produced through the application of Laplace's Method, equation (4.17).

## Chapter 5

# Contact Time Periods in Immunological Synapse

In this chapter, the focus is on the dynamics related to the linear IS model defined by equation (2.12), specifically analysing the variation in the time duration associated with close contact patches of varying bond lengths. The layout of this chapter is as follows: Section 5.1 outlines the objectives of the analysis presented in this chapter. Section 5.2 introduces the two-threshold model that extends the single threshold model previously used for analysing the close contact patch sizes (Chattopadhyay and Burroughs, 2007). Then in section 5.3, the results for the average time persistence of the close contact patches are presented, for both the single and two-threshold models. These results are compared with the analytical results calculated in section 3.1.6. In section 5.4, the probability density functions associated with the time persistence are shown together with a discussion of the symmetry properties for the first passage statistics. Finally, the biological interpretation of these results are discussed in section 5.5.

### 5.1 Introduction

A primary objective of this study is to focus on the kinetic behaviour at the start of the dynamical IS bond formation process. When the TCR is attached to an agonist pMHC, intracellular signalling molecules can phosphorylate the cytoplasmic portion of the TCR leading to signal transduction. Recent studies have also identified TCR microclusters, small patches of membrane enriched in TCR and signalling molecules. Throughout the contact duration the microclusters continuously form in the pSMAC, followed by centripetal migration toward the cSMAC (Yokosuka *et al.*, 2005). The TCR signalling peaks while in the periphery (Mossman, Campi, Groves and Dustin, 2005) and diminishes as they migrate toward the centre of the synapse, with the kinase-phosphatase signalling complexes dissociating from the mi-

croclusters as they cross the barrier from the pSMAC to the cSMAC. The time dynamics of these signals are in the order of seconds, consistent with upregulation of  $\text{Ca}^{2+}$  levels, before the synapse matures minutes later (Dustin, 2008). It is not well understood if signalling continues after the TCR has disengaged from the pMHC, so this scenario is discounted for the present work, although some studies indicate this may be possible (Bunnell, 2010).

The strength and start time of the IS bond patterning is defined by the average time the two randomly forced (due to thermal fluctuations) fluctuating membranes (T-cell and APC) remain in contact with each other above a minimum threshold  $\Delta$ , that is defined by the bond lengths of the participating molecules as described in section 3.2.3. Previously, the model was successfully implemented (Chattopadhyay and Burroughs, 2007) to estimate the average length scale of the interacting TCR:pMHC patch sizes and here the focus is on the average time of contact of these close contact patches, at the start of patterning, based on an analogous *one membrane-two-threshold model* that is described below in section 5.2.

The probability that the membrane remains within a close contact distance, i.e. above the threshold value, represents the survival probability for an engaged bond. The probability density functions for the single threshold and two-threshold models therefore provide a picture of the survival probability as a function of time, for the different bond lengths. The linearised model portrays the non-stationary state dynamics of a fluctuating membrane  $z(\mathbf{x}, t)$  close to the linearly stable point and across a range of mean separation distances, defined by the bond lengths of relevant coreceptor molecules (15-45nm). Incorporation of the first nonlinear (cubic) perturbation in the linearised (stochastic) model predicts a Hopf-bifurcation point, below which the linear regime dominates and above which oscillatory nonlinear patterning takes over (Košmrlj, Kardar and Chakraborty, 2013; Qi *et al.*, 2001; Burroughs *et al.*, 2011). The focus here is to study the crossover from the linear to the nonlinear regime.

## 5.2 The Two-Threshold Model

The starting model is a generalised version of the model described by Chattopadhyay and Burroughs (2007). In this earlier work, they defined a one membrane model fluctuating across a threshold as an analogue of the physical system. In that model, this single threshold cloned the TCR:pMHC and other small coreceptor bond lengths but considered all larger length bonds (e.g. integrin-ligand) as part of the coreceptor chemical potential, which was then associated with the inherent spatial scale of the model itself ( $[L] \sim \sqrt{\frac{B}{\gamma}}$ ). This present improved model considers two thresholds  $\Delta_1$  (TCR:pMHC) and  $\Delta_2$  (LFA-1:ICAM-1) in acknowledgment of the presence of two different length scales, one large and other small, in a reminder of the conclusions drawn by Burroughs *et al.* (2011). Two opposing points on the membranes are said to be within close contact if the separation distance is less than  $-\Delta_i$

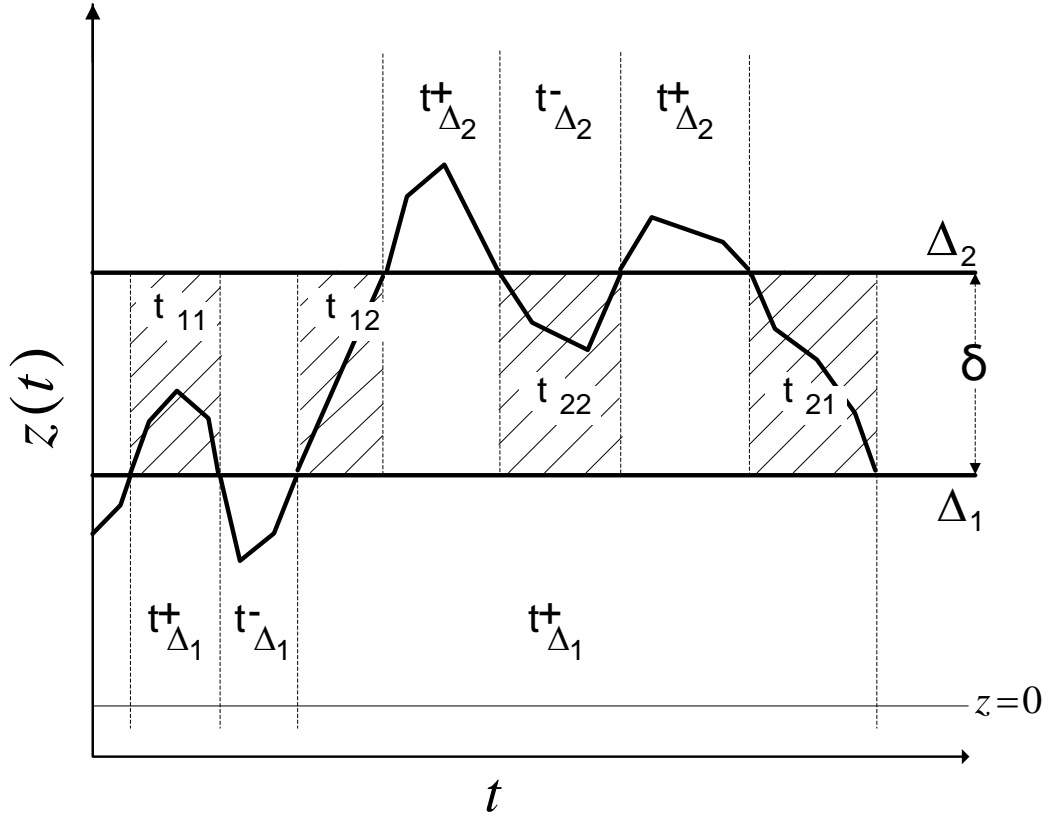


Figure 5.1: **Schematic for the identification of the different time persistence domains for the fluctuating membrane in the IS, using the two-threshold model.** The  $t_{\Delta_i}^+$  regions are periods of time where  $z(\mathbf{x}, t)$  remains above the  $\Delta_i$  threshold. These regions are periods where close contact patches exist between the membrane surfaces at distances  $\Delta_i$  ( $i = 1, 2$ ). The  $t^-_{\Delta_i}$  regions are periods of time where  $z(\mathbf{x}, t)$  remains below the  $\Delta_i$  threshold and this represents the time duration where the membrane separation distance is not favourable for ligand-receptor bond formation. The shaded regions indicate the four different scenarios for time persistence between the two thresholds,  $\Delta_1$  and  $\Delta_2$ . In each case, the separation distance enters the domain between the thresholds for below  $\Delta_1$  or above  $\Delta_2$  and exits again through crossing one of the thresholds.

nm ( $i=1,2$ ), that, in the one-membrane model, translates to a configuration of a fluctuating membrane staying above a critical threshold  $\Delta_i$  nm through a certain average distance  $\langle X^+ \rangle$  (Chattopadhyay and Burroughs, 2007) and an average time  $\langle t^+ \rangle$  (Bush and Chattopadhyay, 2014). Figure 5.1 shows a schematic of the time persistence behaviour of the fluctuating membrane, where  $t^{\pm}_{\Delta_i}$  ( $i=1,2$ ) gives the “bottom-up/up-bottom” cross-over times across the lines  $z = \Delta_i$ , corresponding to the single threshold definition of section 3.2.3.

The two-threshold model introduces additional analytical domains that exist between the two thresholds. The assumption is made that each successive crossing of the  $z = \Delta_i$  line is statistically independent via the *independent interval approximation*. Then, the time persistence characteristics between two thresholds  $\Delta_1$  and  $\Delta_2$  ( $\Delta_2 > \Delta_1$ ), that are separated by a distance  $\delta = \Delta_2 - \Delta_1$ , represents a set of four different events where a signal,  $z(\mathbf{x}, t)$ , persists

between the two thresholds:

$t_{11}$ : the fluctuation enters the  $\delta$  region from below the lower threshold, persists within the  $\delta$  region and returns below the lower threshold, never crossing the upper threshold.

$t_{12}$ : the fluctuation enters the  $\delta$  region from below the lower threshold, persists and becomes larger than the upper threshold.

$t_{21}$ : the fluctuation enters the  $\delta$  region from above the upper threshold, persists and exits below the lower threshold.

$t_{22}$ : the fluctuation enters from above the upper threshold, persists and exits above the upper threshold, never crossing the lower threshold.

A consummate representation of the average time persistence, considering all four scenarios together, can then be given as

$$\langle t_\delta \rangle = \sum_{i,j=1}^2 w_{ij}(\delta) \langle t_{ij}(\delta) \rangle, \quad (5.1)$$

where  $w_{ij}(\delta)$  is the  $\delta$ -dependent probability of the occurrence of the event  $t_{ij}$ , with the probabilities normalised to ensure  $\sum_{i,j=1}^2 w_{ij}(\delta) = 1$ . A detailed quantitative depiction of statistics for each of these zones will be detailed in section 5.4. In the numerical simulation of the model, the above normalisation condition was strictly adhered to.

### 5.3 Average Close Contact Time Persistence

The theoretical routine encompasses both analytical and numerical fronts. As of the former, the target is to recast the model solutions within a Gaussian Stationary Process framework and use the methods set out in section 3.1.6 to determine the average time persistence about  $\Delta_i$ . For the latter, numerical integration of the stochastic model, using Eulerian and Runge-Kutta schemes separately, is followed by an estimation of the average time persistence, and then the probability density function of the persistent crossings.

In the numerical simulations, the magnitude of noise strength ( $D$ ) is chosen to provide enough stimulation to overcome the relaxation dynamics and drive the thermal fluctuations, while remaining small enough to avoid dominating the equation, rendering it pure brownian motion. Here the choice of  $D = 4.7 \times 10^7$  is shown to satisfy this remit through dimensional analysis. From a dimensional term-by-term comparison of the starting linear model, using

the biological parameter values described in table 2.2, the dimensional analysis gives

$$\begin{aligned}
B\nabla^4 z &\sim \gamma\nabla^2 z \sim \lambda z \sim \sqrt{2D}\zeta \\
11.8 \times \frac{[z]}{L^4} &\sim 5650 \times \frac{[z]}{L^2} \sim 6 \times 10^5 \times [z] \sim \sqrt{2 \times 4.7 \times 10^7} [\zeta] \\
\frac{11.8 \times [z]}{(10^2 \times 10^{-3})^4} &\sim \frac{5650 \times [z]}{(10^2 \times 10^{-3})^2} \sim 6 \times 10^5 \times [z] \sim \sqrt{9.4 \times 10^7} [\zeta] \\
\frac{11.8 \times [z]}{10^{-4}} &\sim \frac{5.65 \times 10^3 [z]}{10^{-2}} \sim 6 \times 10^5 \times [z] \sim \sqrt{0.94} \times 10^4 [\zeta] \\
1.18 \times 10^5 [z] &\sim 5.65 \times 10^5 [z] \sim 6 \times 10^5 \times [z] \sim 1 \times 10^4 [\zeta]
\end{aligned}$$

where  $\zeta$  is a random variable drawn from a Gaussian distribution with zero mean and unit variance. The numerical results shown below apply this noise strength regime.

Figure 5.2 shows the ensemble average for the time persistence above any of the ( $\Delta_1$  or  $\Delta_2$ ) thresholds keeping the other fixed, for both the numerical and the scaled analytical solution. The parameters used give rise to persistent close contact patches in the order of magnitude required for the biological problem, that is 15-45 nm. The numerical results (in dots: figure 5.2) are consistent with the analytical solutions (continuous line: figure 5.2), where the close contact time decreases as the separation distance increases, suggesting that the TCR:pMHC bond persists longer than the LFA-1:ICAM-1, thereby explaining the stability aspect of shorter bonds, as was previously conjectured by Burroughs and Wülfing (2002).

The result shown in figure 5.2 can be qualitatively understood from simple probabilistic considerations. As the threshold value increases, it becomes more difficult for the randomised (Gaussian) fluctuations to cross this threshold, resulting in reduced average time spent above the threshold value, also leading to smaller time patches. More non-trivial, though, is the functional nature of the decay in the  $\langle \tau^+ \rangle$  value against  $\Delta$ . As opposed to a simplistic (and incorrect) visual impression, the decay profile here is not exponential, rather it is defined through an intricate balance between power-law scaled fluctuations against the statistics of deterministically decaying membrane fluctuation modes.

A vital part of this model study is the analysis of the dynamics of the randomly driven membrane in between the two given thresholds. In line with the parlance used previously, as well as in (Chattopadhyay and Burroughs, 2007), this can be represented as an estimation of the time persistence between two threshold values,  $\Delta_1$  and  $\Delta_2$ , where  $\Delta_1$  is the T cell analogue of the TCR:pMHC bond length ( $\sim 15$  nm) and  $\Delta_2$  symbolises the LFA-1:ICAM-1 bond separation length ( $\sim 45$  nm).

The result for the variation of the average time between the two thresholds as a function of the distance  $\delta$  between the thresholds is shown in figure 5.3. The calculations were performed by starting with  $\Delta_1 = 0$  nm and then varying  $\Delta_2$  between 1 nm to 50 nm. The results shown in figure 5.3 are the average over multiple such initial choices of  $\Delta_1$  and then varying

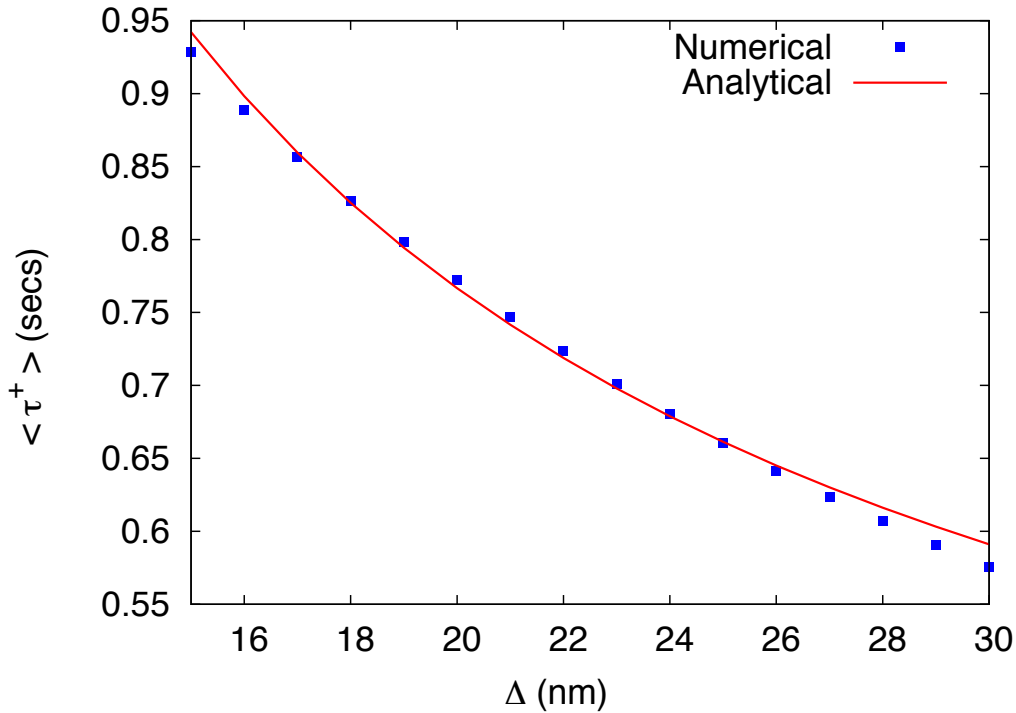


Figure 5.2: **Time persistence above the  $\Delta_i$  threshold,  $\langle \tau^+ \rangle$  vs  $\Delta_i$ .** The dots show the result obtained by numerically solving equation (3.56) and applying the method set out in section 3.2.3, while the solid line indicates the analytical result obtained from a solution of equation (3.35). The results have been linearly scaled for comparison and qualitatively remain unchanged irrespective of the choice of  $\Delta_1$  or  $\Delta_2$ , since this is essentially a single threshold analysis.

$\Delta_2$  accordingly to generate the appropriate range for  $\delta$ . The dotted points refer to the numerical simulation results while the continuous line represents the interpolation of the same to maintain continuity. The time persistence initially increases as  $\delta$  increases, then it saturates and asymptotically approaches the  $\langle \tau^+ \rangle_{\Delta_1}$  value, as the two-threshold picture reduces to the one-threshold picture. As  $\delta \rightarrow 0$  the average time persistence tends toward the smallest time length scale used. For the case shown,  $dt = 0.1$  seconds. Once again, an understanding of figure 5.3 can be had from the fact that an increase in the  $\delta$  value can be wrought about in either of the two possible ways, either through an increase in  $\Delta_2$  for fixed  $\Delta_1$ , or else through a decrease in  $\Delta_1$  for a fixed  $\Delta_2$ . For the first case, fixing  $\Delta_1$  and increasing  $\Delta_2$ , it is easier for a fluctuation mode to remain within the upper limit ( $\Delta_2$ ) than to cross it. For the second case, with a fixed value of the upper threshold  $\Delta_2$ , a lowering of  $\Delta_1$  increases the probability of a fluctuation mode remaining within the lower limit, thus increasing the value of  $\langle \tau_\delta \rangle$ .

Figures 5.2 and 5.3 respectively express the variation of the average “persistent times” against bond lengths above a critical threshold, and between two thresholds ( $\Delta_1$  and  $\Delta_2$ ). These results are subsets of a bigger ensemble defined by a membrane that fluctuates across two thresholds  $\Delta_1$  and  $\Delta_2$ , or else that of two membranes whose fluctuations are measured

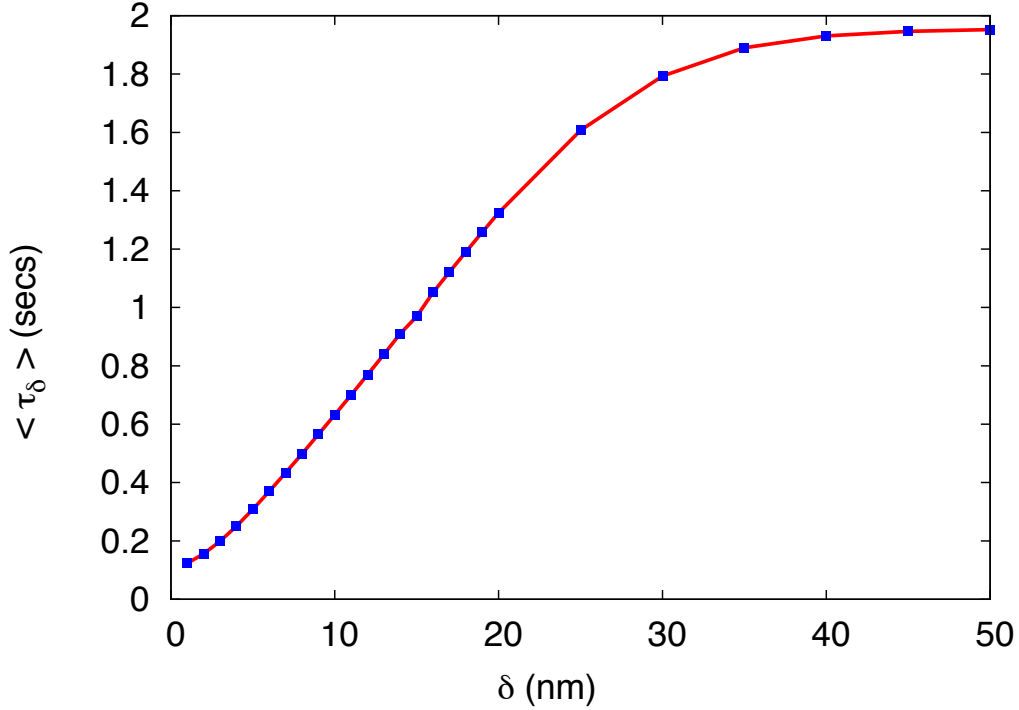


Figure 5.3: **Time persistence between two thresholds,  $\langle \tau_\delta \rangle$  vs  $\delta$ .** The ensemble average time persistence between two thresholds, where the distance between the thresholds is given by  $\delta = \Delta_2 - \Delta_1$ . The dotted points represent the numerical results and the solid line is an interpolation of the numerical results.

across a single threshold  $\Delta$ , that, as already explained earlier, are equivalent analytical descriptions. In line with the model of a single membrane, fluctuating across two thresholds, as detailed in the previous section and as depicted in figure 5.1, the statistics can be classified into four broad zones - “11”, “12”, “21” and “22”. While “11” defines the fluctuation regime for a crossing from a region in  $z < \Delta_1$  across the line  $z = \Delta_1$ , remaining below the upper threshold ( $z < \Delta_2$ ) and then returning to the  $z < \Delta_1$  region, “22” encapsulates the complementary regime for a crossing across  $z = \Delta_2$  from a point  $z > \Delta_2$ . “12” and “21” represent statistics when crossings are restricted within  $\Delta_1 < z < \Delta_2$  as explained in figure 5.1.

## 5.4 Persistence Probability Density of Close Contact Time

Representing the corresponding average t“persistent time” by  $\tau_{ij}$  ( $i,j=1,2$ ), it can be shown that due to reflection symmetry, the time correlators obey ( $A_+(t_+, \Delta_1) = -A_-(t_-, \Delta_2)$  and  $A_-(t_+, \Delta_1) = -A_+(t_-, \Delta_2)$ ), such that  $\tau_{11}$  and  $\tau_{22}$  are identical, as are  $\tau_{12}$  and  $\tau_{21}$ . Comparing with the notations used previously,  $\tau_{12}(= \tau_{21})$  may be identified with  $\tau_\delta$  as in figure 5.3, while  $\tau_{11}(= \tau_{22})$  may be identified with  $\langle \tau^+ \rangle$  under the constraint  $z < \Delta_2$ . For the same reason (reflection symmetry), as shown in figure 5.4, the respective density distributions also conform to these symmetry lines.

The result presented in figure 5.4 is not a special case, as shown in figure 5.5 where the  $\tau_{11}$

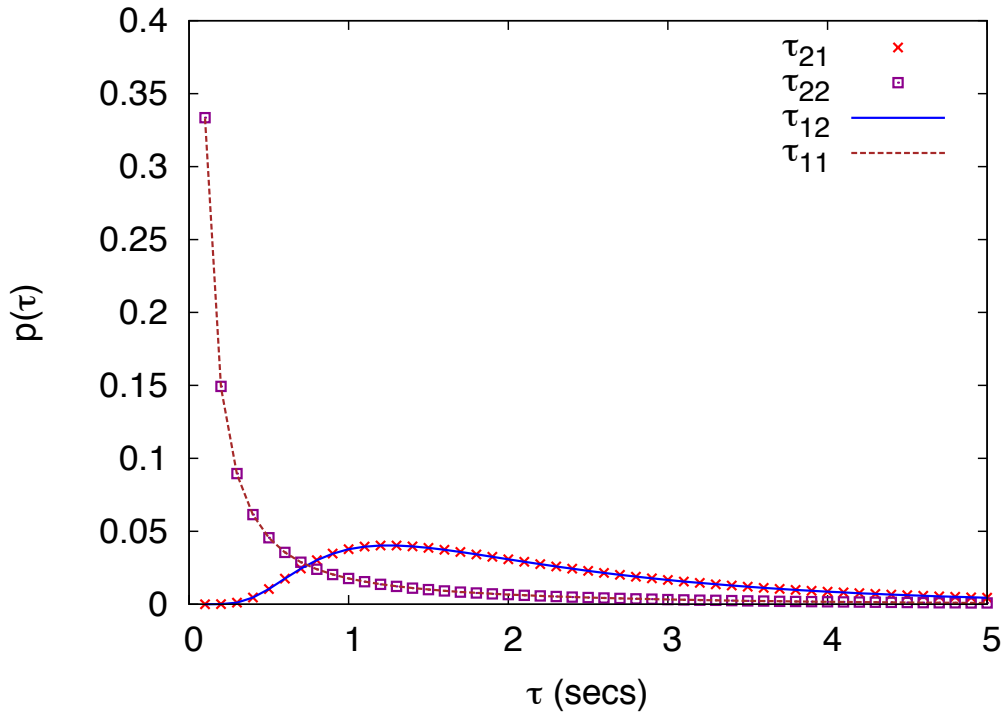


Figure 5.4: **Probability density,  $p(\tau)$  between two thresholds.** For large enough statistics, the probability density profile for  $\tau_{11}$  is equivalent to  $\tau_{22}$ , and similarly the probability density for  $\tau_{12}$  is equivalent to  $\tau_{21}$ .

and  $\tau_{12}$  probability densities are plotted for three values of  $\delta$ . As  $\delta$  increases, the probability density for the  $\tau_{12}$  case shows an increase in the probability associated with longer time persistences, shown as a right shift in the statistics for the *stretched Gaussian with a long tail*, a result that matches with the observation presented earlier through figure 5.3. On the other hand, the number of  $\tau_{12}$  events become less frequent as  $\delta$  is increased, since the probability for crossing the upper threshold is significantly decreased. The  $\tau_{11}$  probability densities also change slightly as  $\delta$  varies, again showing an increase in the probability for longer time persistence, that corresponds to bond durations in the order of seconds, consistent with  $\text{Ca}^{2+}$  concentration level elevation.

## 5.5 Discussion

The analysis presented here has two major immunological implications. Firstly, figures 5.2 and 5.3 clearly prove that the onset of patterning at the immature synapse level, when the central LFA-1:ICAM-1 bond gives way to the smaller TCR:pMHC bond, occurs at the time scale of seconds. This discovery is expected to confirm the start time of mature synapse formation. Admittedly, though, the parameter values used make the result a subjective case for TCR:pMHC bonding, in that the time scale predicted for a different membrane:membrane dynamics may as well be in minutes or hours, instead of in seconds. Secondly, the non-universal character of the time correlation of the IS bond, in that the probability density

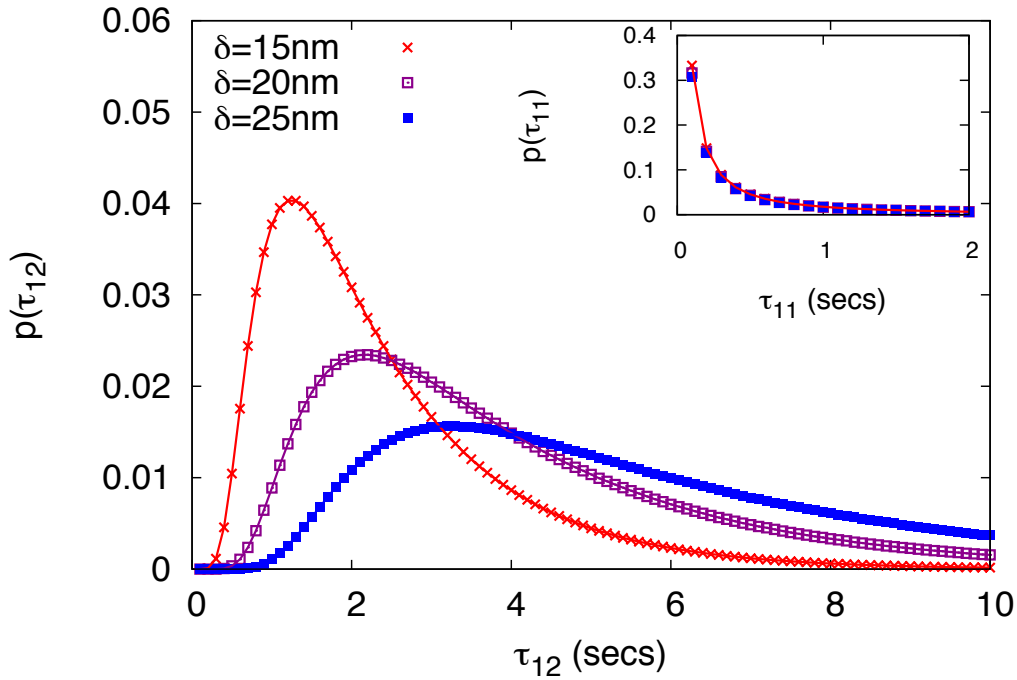


Figure 5.5: **Comparison of the probability density for  $p(\tau_{12})$  and  $p(\tau_{11})$  as  $\delta$  varies.**

$p(t)$  is a function of the system parameters along with being a function of the bond length difference  $\delta$  (figure 5.5), confirms a widely acknowledged belief in the community that the TCR:pMHC bond is non-self-organising in nature. As shown in figure 5.5, the difference in the two bond lengths introduces a persistence time scale that spans 2-4 seconds (peak time of the PDF profile). The implication of this analysis is that of a time scale difference of an order of magnitude related to the start time of the “immature” IS bond formation, a time scale that is also associated with the transition from the linear to the nonlinear regime (and hence the emphasis on this study of the linear stability regime of an otherwise nonlinear dynamics). How such a crossover is affected by the kinase-phosphatase signalling pathways and what modifications it may have on the prediction of the time scale of a mature IS bond are some of the exciting topics currently being investigated.

Results from the linear membrane model calculations show  $\langle \tau^+ \rangle$  to be of the order of seconds instead of minutes. Close to the linearly stable regime, it is shown that in between the two critical spatial thresholds, defined by the integrin:ligand pair ( $\Delta_2 \sim 40-45$  nm) and the T cell receptor (TCR):pMHC bond ( $\Delta_1 \sim 14-15$  nm),  $\langle \tau \rangle$  grows monotonically with increasing co-receptor bond length separation  $\delta$  ( $= \Delta_2 - \Delta_1 \sim 26-30$  nm) while  $\langle \tau \rangle$  decays with  $\Delta_1$  for fixed  $\Delta_2$ .

## Chapter 6

# Temporal dynamics in immunological synapse: Role of thermal fluctuations in signalling

This chapter analyses the contribution of *stochastic thermal fluctuations* in the attachment times of the immature TCR:pMHC immunological synapse bond. The key question addressed here is the following: how does a synapse bond remain stabilised in the presence of large thermal noise that potentially equates to a strong detaching force? Focusing on the average time persistence of an immature synapse, it is shown that the extremal value statistics of large fluctuations are accompanied by an even faster energy dissipation mechanism that eventually leads to the immunological synapse bond being unaffected by the extremal value statistics of large amplitude fluctuations. The analysis shows that such a counterintuitive behaviour, a null result, could be easily explained from the fact that the survival probability distribution is governed by two distinct phases, corresponding to two separate time exponents, for the two different time regimes. The relatively shorter time scales correspond to the cohesion:adhesion induced immature bond formation, whereas the larger time reciprocates the association:dissociation regime leading to TCR:pMHC signalling.

The chapter is organised as follows: in section 6.1, the ensemble statistics used to generate the results are shown, along with the probability density profile associated with the single threshold method described in section 3.2.3. This is followed by an analysis of the numerical results, that is subdivided into three parts. Section 6.2 analyses the small time phase where thermal fluctuations are dominant, section 6.3 analyses the large time phase statistics and section 6.4 focuses on extremal value statistics, including comparisons with sections 6.2 and 6.3. This is followed by a discussion of the biological implications of these results in section 6.5.

## 6.1 Close Contact Survival Statistics

Equation (3.56) was solved using the parameter values described in table 2.2. The numerical simulations were performed for a time evolution using a sufficiently large time window, including  $10^6$  time steps. The  $t_{\Delta}^+$  statistics for the frequency distributions using the single threshold model were then collected, as set out in section 3.2.3.

Using these simulation parameters, a single  $d=2+1$  system with a lattice of  $L = 10 \times 10$  discrete spatial points generates on average  $2.5 \times 10^5$  statistics for  $\Delta = 0$ . As the  $\Delta$  threshold increases, the average number of statistics per system decreases as shown in figure 6.1. Ensemble averaging was used to further increase the statistics, where an ensemble size of  $10^5$

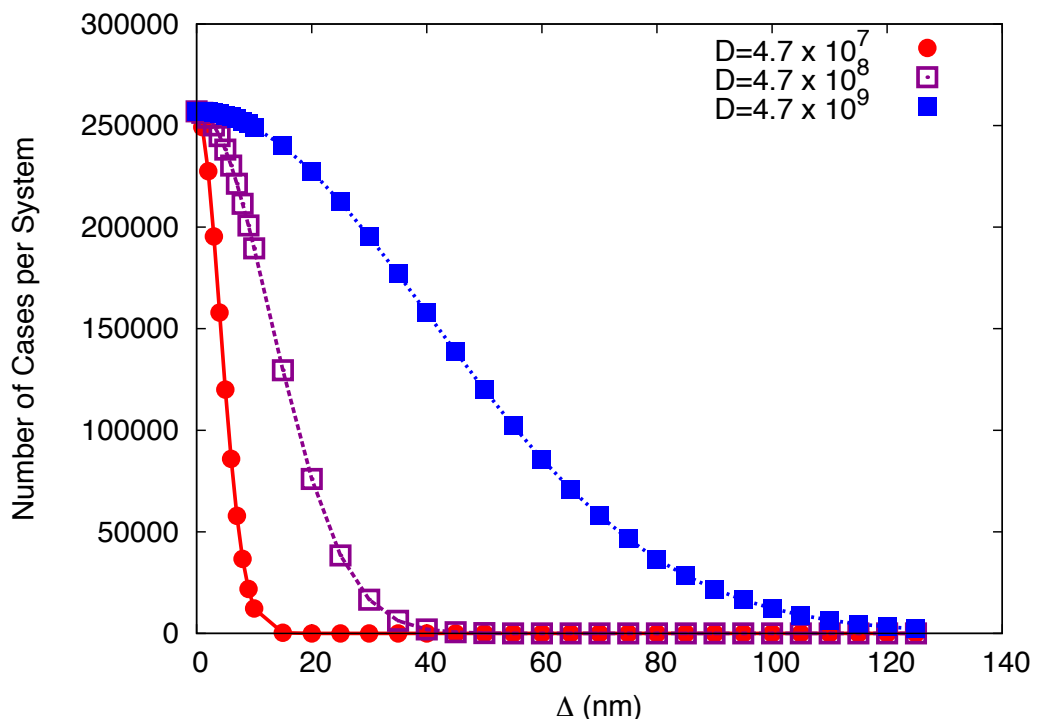


Figure 6.1: **Average number of cases per system run for  $d = 2 + 1$ .** The number of statistics per simulated system is plotted against the  $\Delta$  threshold value. Three thermal noise strengths are plotted to show the variation in the statistics as the noise strength changes.

systems produced statistics in the order of  $10^{10}$  for the  $\Delta = 0$  case. Increasing the thermal noise strength increases the range of  $\Delta$  where statistics can be found, although the Gaussian profile shown in figure 6.1 is unaltered. It can also be noted that the number of statistics is constant for  $\Delta = 0$ , regardless of the noise strength. Simulations were performed on a lattice of  $L=100 \times 100$  and the number of statistics generated scales proportional to the number of spatial nodes.

Figure 6.2 shows the numerical simulation results for the probability density,  $W_{\Delta}(\tau)$ , for the  $\tau_{\Delta}^+$  instances (for  $\Delta = 0\text{nm}$ ), as defined by equation (3.61). This probability density is then used to calculate the survival probability,  $P_{\Delta}(\tau)$  as defined in equation (3.62). Figure 6.3 shows the log:log plot (solid line) for the survival probability, produced from a numerical

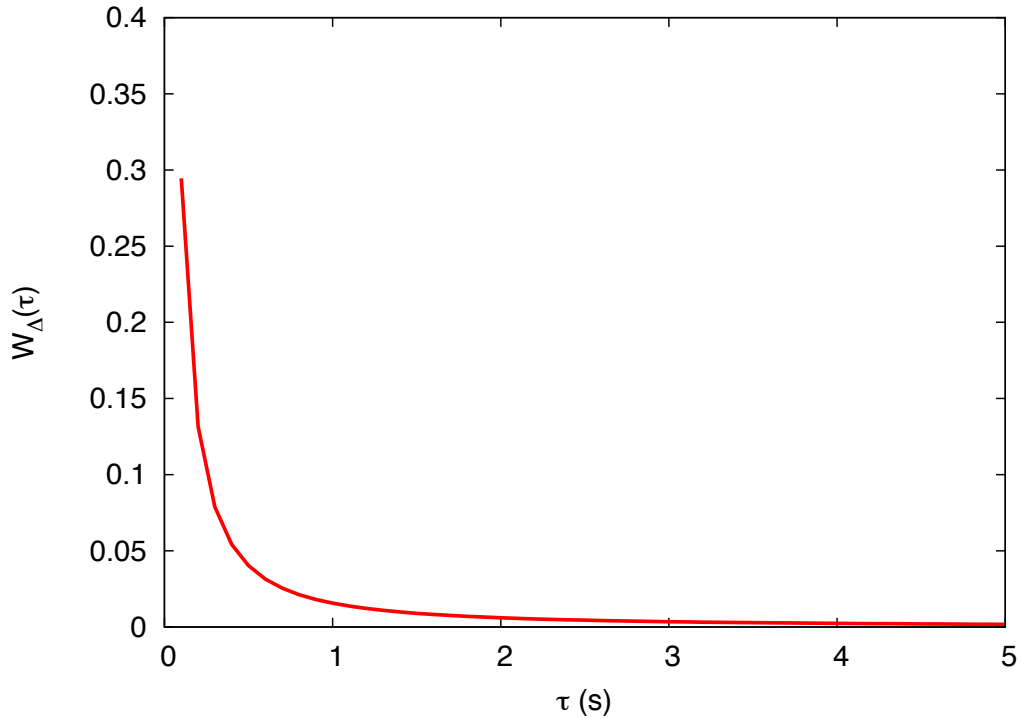


Figure 6.2: **The probability density distribution,  $W_{\Delta}(\tau)$ , for the time persistence above  $\Delta = 0$  nm.**

simulation for the  $\Delta = 0$  case and using the model parameter values mentioned above. Two distinct linear regions can be observed, corresponding to two different power law regimes. Using a least squares' linear fit in the log:log regime, approximations for the time persistence exponents were estimated for each regime. The transition region separating the two different scaling regimes, the *crossover* region, has a length scale in the order of tens of seconds, with the crossover point  $\tau_{\times}$  shown as the intersection between the least square fitted lines. Defining  $\theta_S$  as the time persistence exponent for the small  $\tau$  regime and  $\theta_L$  as the exponent for the large  $\tau$  regime, the survival probability scales according to

$$P_{\Delta}(\tau) \sim \tau^{-\theta_S} \quad \tau \ll \tau_{\times} \quad (6.1)$$

$$P_{\Delta}(\tau) \sim \tau^{-\theta_L} \quad \tau \gg \tau_{\times} \quad (6.2)$$

As the results clearly show, the system exhibits two different relaxation time scales, one dominated by diffusion and the other by the chemical force interacting with the stochastic forcing. In a way, this is complementary to the two time scale problem that was analysed earlier (Burroughs and Wülfing, 2002). In the following subsections the small and large  $\tau$  regimes are analysed, with respect to the bond length and thermal noise strength. In the final section, the persistence probability density is used to understand the effect of high frequency fluctuations on the average statistics.

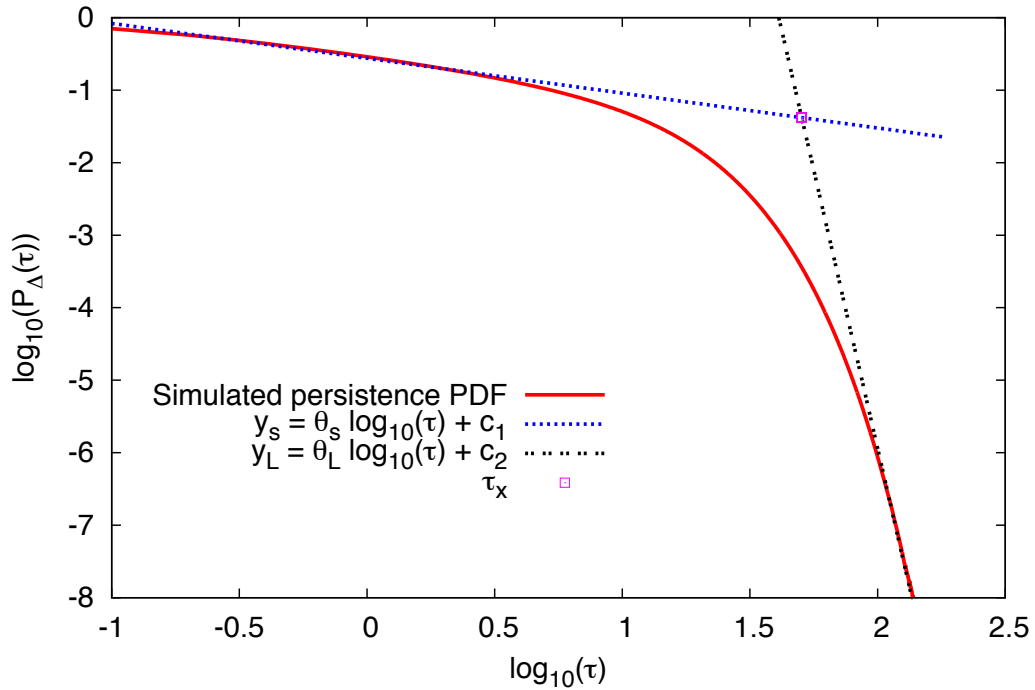


Figure 6.3: **Log:Log plot for the survival probability  $P_{\Delta(=0)}(\tau)$ .** The gradients for the two fitted lines,  $\theta_S$  and  $\theta_L$ , show the power law decay for the small  $\tau$  and large  $\tau$  time domains, respectively. The crossover point between these regimes is marked as the intersection between the fitted lines (square point)

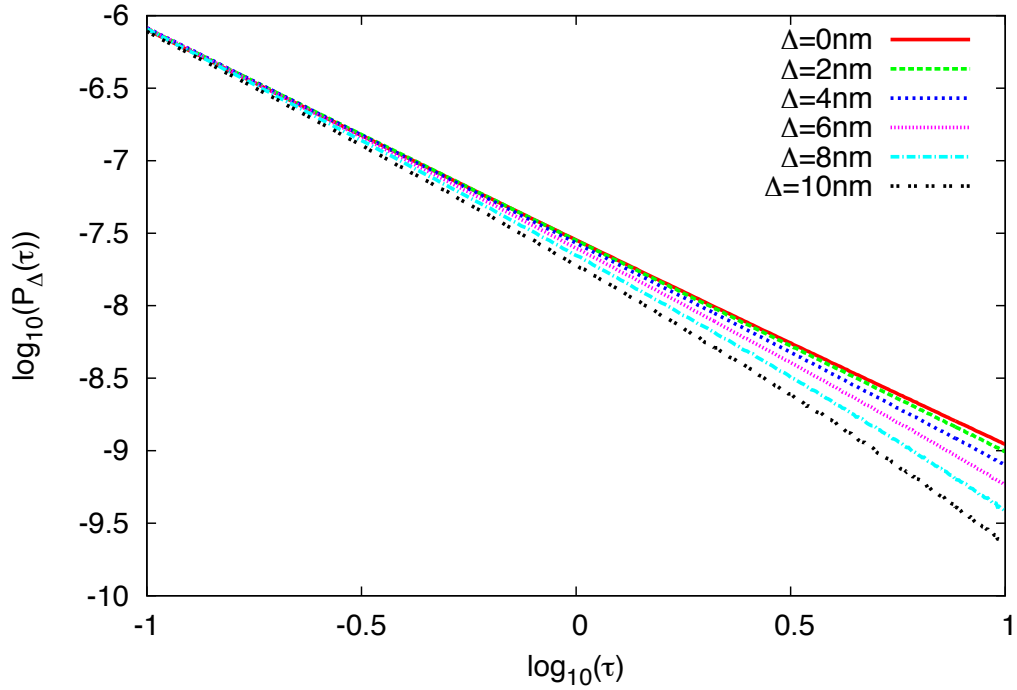
## 6.2 The Small- $\tau$ Phase: The “Thermal Fluctuations” regime

The small  $\tau$  phase represents the regime where receptor:ligand complexes are associating and dissociating rapidly due to the impact of high frequency thermal fluctuations, within a relatively small time frame. The bond duration in the small  $\tau$  regime is not deemed sufficient to coincide with the elevation in intracellular  $\text{Ca}^{2+}$  levels at 6 seconds (Huse *et al.*, 2007).

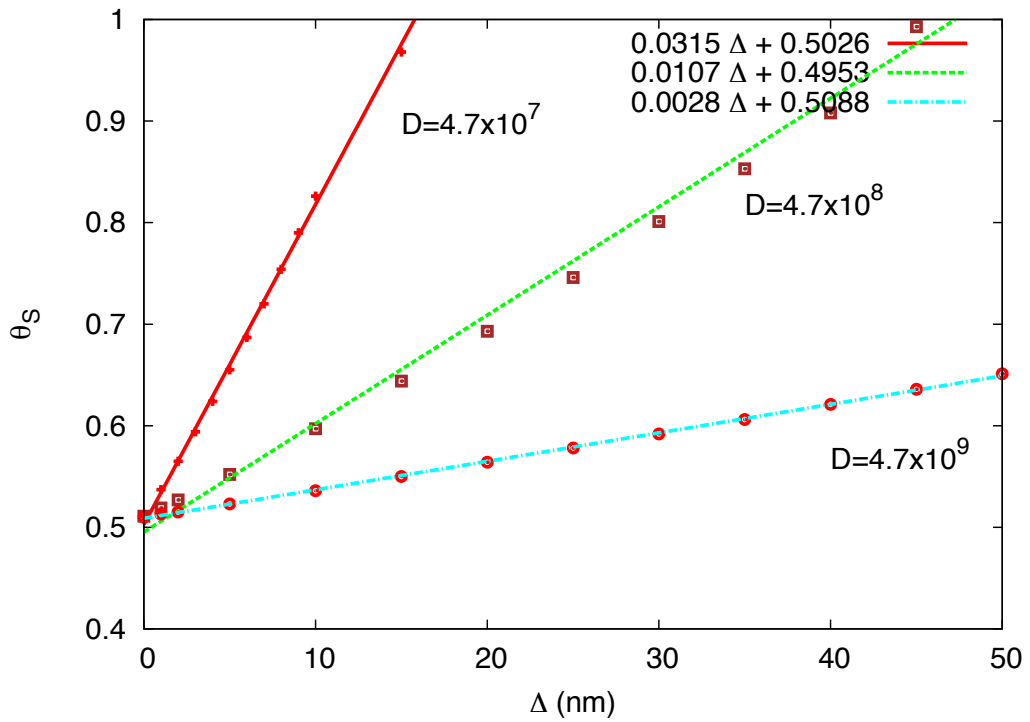
However, this regime is statistically relevant due to its impact on the average time persistence. The simulation results and subsequent calculations indicate the probability density associated with  $\Delta = 0$  explains  $\sim 30\%$  of the statistical cases, where the bonds persist for a single time step and then return below the threshold (shown in figure 6.2). Using the notation from equation (3.61), the first passage probability values are  $p_1^0 = 0.29306$ ,  $p_2^0 = 0.12993$  and  $p_3^0 = 0.07751$ , and thus, 50% of the  $t_{\Delta=0}$  instances survive for three (or less) discrete time lengths.

Simulations using  $\Delta t = 0.01$  second were run and figure 6.4(a) shows the log:log plot for the survival probability against time for different values of  $\Delta$  in the small  $\tau$  regime. The plot shows  $\theta_S$  becomes steeper with increasing  $\Delta$ , indicating the rate of decay for the survival probability (and hence the survival probability) is dependent on  $\Delta$ . The direct relationship between  $\theta_S$  and  $\Delta$  is shown in figure 6.4(b) for three different thermal fluctuation strengths. In each case, a near linear relationship exists between the time exponent  $\theta_S$  and  $\Delta$ . All three

values of  $D$  have the same persistence exponent at  $\Delta = 0$ , but the rate of change of the time exponent with respect to  $\Delta$  is increased as  $D$  is decreased.



(a)



(b)

Figure 6.4: **The time exponent for the small  $\tau$  regime.** Figure 6.4(a) shows the plot of the survival probability against time, in the log:log scale, for a range of  $\Delta$  and figure 6.4(b) shows the time exponent  $\theta_S$  plotted against  $\Delta$  for three different thermal noise strengths.

The linear relationship between  $\theta_S$  and  $\Delta$  suggests the persistence probability has a scaling

relationship in the small  $\tau$  regime of the form

$$P(\tau) \sim \tau^{-\theta_S(\Delta)} \sim \tau^{-(\alpha\Delta+\beta)} \quad (\tau \ll \tau_x) \quad , \quad (6.3)$$

where  $\alpha$  is the coefficient related to the  $\Delta$  dependence, and  $\beta$  is the persistence exponent when  $\Delta = 0$ . Table 6.1 shows values for  $\alpha$  and  $\beta$  for a range of  $D$ . The value of  $\beta$  is constant for all

$\delta$ -correlated noise strength ( $D$ )	$\alpha$	$\beta$
$4.7 \times 10^6$	0.0971	0.5030
$4.7 \times 10^7$	0.0315	0.5026
$4.7 \times 10^8$	0.0107	0.4953
$4.7 \times 10^9$	0.0028	0.5088
$4.7 \times 10^{10}$	0.0008	0.5090

Table 6.1: **Linear fit parameters for  $\theta_S$ .** The  $\alpha$  parameter is dependent on the noise strength, whereas  $\beta$  is independent of the noise.

$D$ , but  $\alpha$  is clearly dependent on  $D$ . Plotting  $\alpha$  against  $D$  in the log:log scale (fig. 6.5) reveals

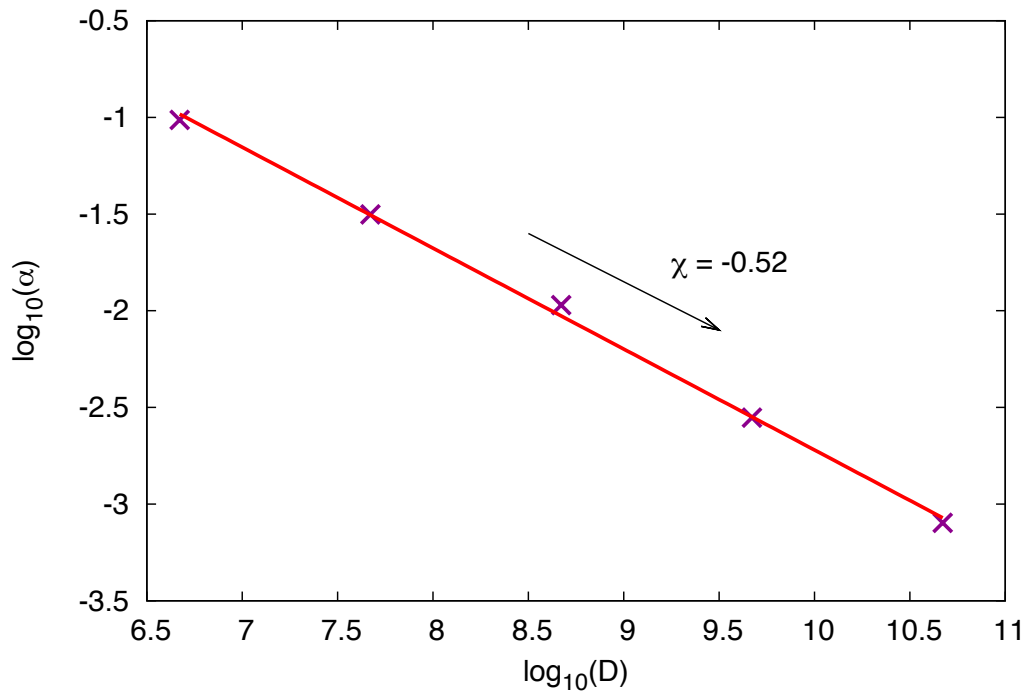


Figure 6.5: **The  $\alpha$  dependence on  $D$ .** Linear fit (solid line) for the time exponent parameter  $\alpha$  against  $D$  in the log:log scale.  $\chi$  shows the gradient of the fitted line.

a linear relationship that leads to a power law:  $\alpha \sim D^\chi$ . The fitted solid line in figure 6.5 suggests a value of  $\chi \approx -0.52$ ; in other words,  $\alpha \sim \frac{1}{\sqrt{D}}$  that combined with the definition of the exponent  $\alpha$  gives the noise scaling of the survival probability as  $P(\tau) \sim \tau^{-(\frac{\Delta}{\sqrt{D}}+\beta)}$ . Mathematically, this implies the existence of a well defined universality class of the noise strength as a function of the bond length  $\Delta$ , which also means that numerical simulations could better use the redefined noise amplitude  $\frac{D}{\Delta^2}$  instead of  $D$ . One must here be aware of

a realistic biological constraint, where higher noise corresponds to larger thermal fluctuations and hence will be capped at some finite value for a finite sized system.

Table 6.1 suggests that for  $\Delta = 0$ , the survival probability is independent of the noise strength (since  $\beta$  is noise independent always converging to the value 0.5) as it should be for Brownian motion. However, for all other values of  $\Delta$ , there is a competition between the free energy and noise terms that eventually determines the effective number of data points to be obtained numerically (the plot for  $D = 4.7 \times 10^8$  in figure 6.1 is instructive here). In a way, this suggests the limit of simulation accuracy in analysing the probabilistic persistence data. So, increasing the thermal noise leads to a greater range of statistics for increasing  $\Delta$ , but does not alter the time exponent relating to  $\Delta = 0$  nm, that corresponds to the glycocalyx length used in the linear stability analysis. The range of  $\tau$  where the scaling relation in equation (6.3) holds is in the order of seconds and the range decreases steadily as  $\Delta$  increases.

### 6.3 The Large- $\tau$ Phase: The “Signalling” regime

The large  $\tau$  phase represents the regime where infrequent, longer lasting, receptor:ligand bonds exist. This is the phase characterised by large TCR:pMHC bond half lives facilitating intracellular signalling required for T-cell activation. The persistence time of these bonds are in the order of tens of seconds and therefore sufficient for signalling pathways that lead to elevated levels of intracellular  $\text{Ca}^{2+}$ .

Analysis of the  $\theta_L$  values for different  $\Delta$  reveals a consistent decay rate of  $\theta_L \sim 16$ . By rescaling the different curves for each  $\Delta$  the large  $\tau$  regime can be data collapsed on to a single universal curve (Barabasi and Stanley, 1995). Figure 6.6 shows the rescaling steps in the log:log scale. The crossover time for a given  $\Delta$ ,  $\Omega_\Delta = \log(\tau_\times)$ , is used as a hard cut-off between the small and large  $\tau$  regimes (fig. 6.6(a)).  $\Omega$  is plotted against  $\Delta$  in figure 6.7(a) for three different noise strengths, where it is found a near linear relationship exists for small  $\Delta$ . For a fixed noise strength the statistics drop off at some upper limit, as shown in figure 6.1. As  $\Delta$  approaches this upper limit, the linear relationship between  $\Omega$  and  $\Delta$  is less convincing, that may or may not be answered with increased statistics, but it is not considered further in this report.

A linear fit can be applied to the sample crossover points,  $\Omega_\Delta$ , for a given noise strength. This linear relationship, shown in figure 6.7(a) (solid lines), leads to the expression  $\Omega = \log(\tau_\times) = -\omega\Delta + c_1$ , where  $c_1$  is a scaling constant. Similar to the analysis conducted for the small  $\tau$  regime, the  $\omega$  coefficient is dependent on the noise strength, but the  $\Delta = 0$  case is independent of noise strength. The crossover time can be then be expressed as the

exponential

$$\tau_{\times} \sim e^{-\omega(D)\Delta+c_1} \quad . \quad (6.4)$$

Then, rescaling the time dimension, using the new time variable  $u = \log(\tau/\tau_{\times})$ , corresponds to a horizontal shift of the curves in the log-log scale. This ensures the phase transition occurs at the same point in the time dimension for all values of  $\Delta$  (figure 6.6(b)).

Similarly, rescaling is applied in the direction of the survival probability. To achieve this, the definition  $\Psi_{\Delta} = \log(P_{\Delta}(\tau_{\times}))$  is used, as shown in 6.6(b), then the values of  $\Psi_{\Delta}$  are plotted against  $\Delta$  (figure 6.7(b)). Again, a linear relationship between  $\Psi_{\Delta}$  and  $\Delta$  is observed, which can be modelled through the linear fit  $\Psi_{\Delta} = -\psi\Delta + c_2$  and it is noted that the  $\psi$  coefficient has a dependency on the thermal noise strength,  $D$ . The survival probability at the crossover time can then be expressed as the exponential

$$P_{\Delta}(\tau_{\times}) \sim e^{-\psi(D)\Delta+c_2} \quad (6.5)$$

where  $c_2$  is a scaling constant. Equations (6.4) and (6.5) remain impervious to changes in the noise strength for  $\Delta = 0$ , thereby indicating the existence of a universal survival probability for  $\Delta = 0$ . This result has a vital biological connotation. While all other persistence statistics are shown to be scale dependent, the cross-over time regime is a scale independent dynamics, suggesting that parameter values could always be monitored to attain non-equilibrium dynamics.

Using the steps above, the following scaling function is introduced

$$f(\tau, \tau_{\times}) = \log(P_{\Delta}(\tau)/P_{\Delta}(\tau_{\times})) \quad (6.6)$$

and plotted against the new time variable,  $u$ , as shown in figure 6.6 (c). This leads to the data collapse in the large  $\tau$  regime on to the universal problem

$$f(\tau, \tau_{\times}) = -\theta_L u + c_3 \quad , \quad (6.7)$$

where  $\theta_L$  is the time exponent described in equation (6.2) and  $c_3$  is a scaling constant. This relationship is valid for  $u \geq 0$ , corresponding to  $\tau \geq \tau_{\times}$ . Substituting equation (6.6) into equation (6.7), the survival probability can be rearranged to give the following scaling relationship

$$P_{\Delta}(\tau) \sim \tau^{-\theta_L} \quad \tau \geq \tau_{\times} \quad . \quad (6.8)$$

Also, from equations (6.4) and (6.5), the magnitude of the survival probability for a given  $\Delta$

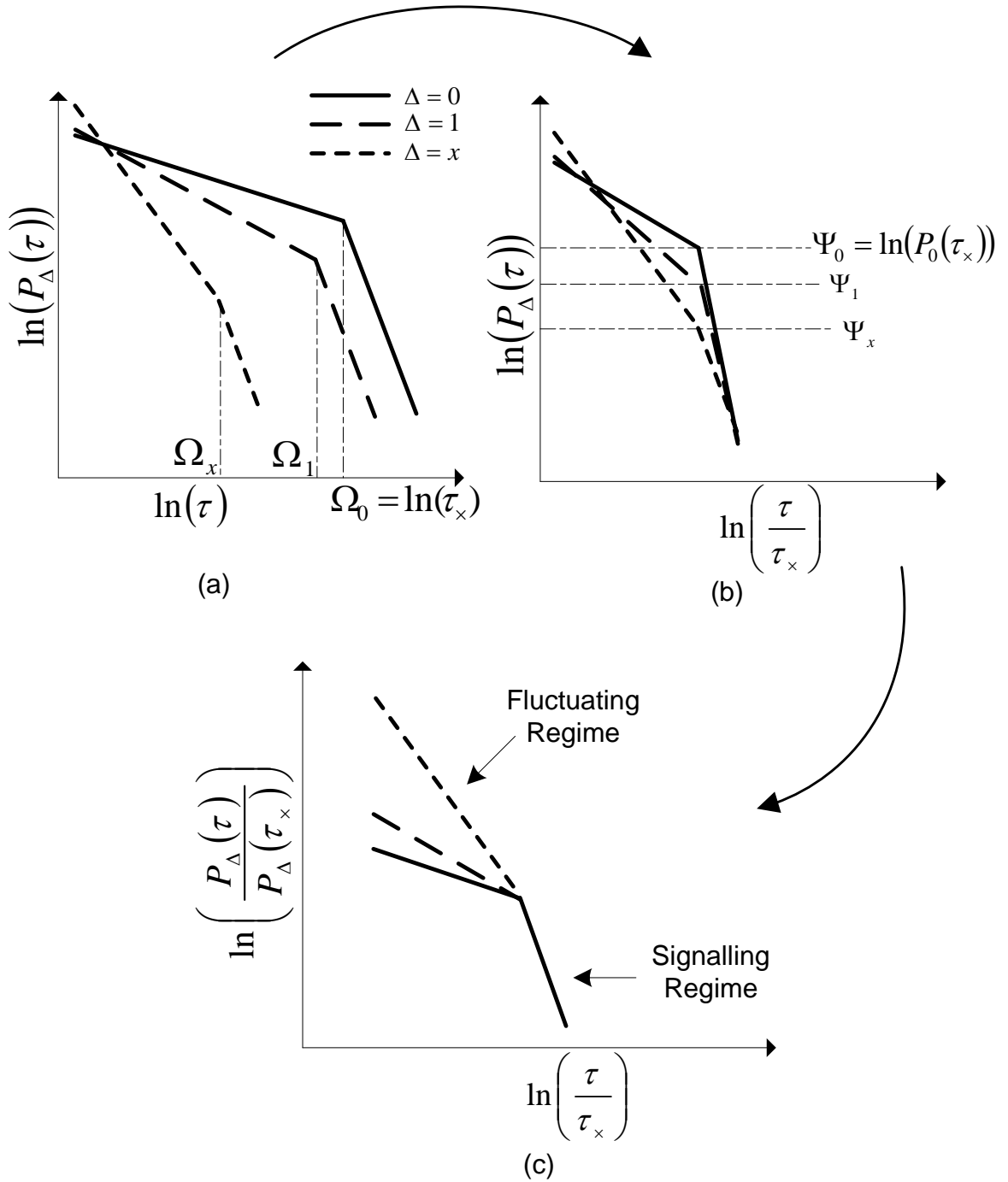
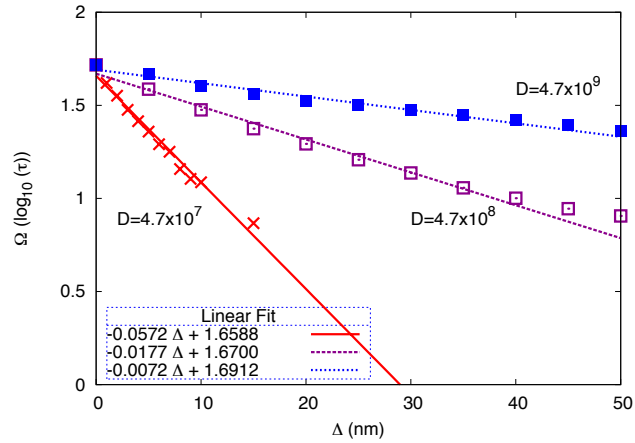
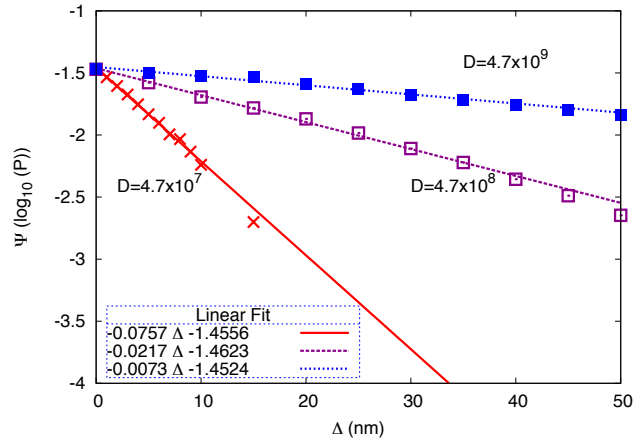


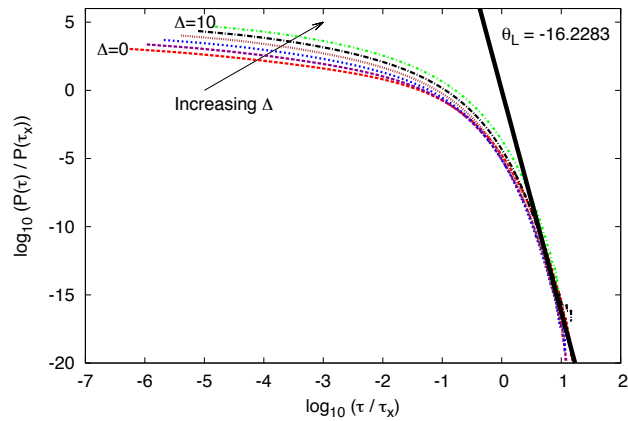
Figure 6.6: **Schematic illustration of the time-dependent rescaling used in the large  $\tau$  regime.** In figure 6.6 (a) the time dimension is rescaled to ensure the crossover point between the two phases occurs at the same time for each  $\Delta$ , then figure 6.6 (b) shows the rescaling step in the direction of the probability density, that collapses the large  $\tau$  regime for the different  $\Delta$  curves. Figure 6.6 (c) shows the final data collapse for the rescaled curves for  $\tau \geq \tau_x$ .



(a) The time dimension rescaling with respect to  $\Delta$ .



(b) The probability rescaling with respect to  $\Delta$ .



(c) The collapsed large  $\tau$  regime.

Figure 6.7: **The rescaling functions,  $\Omega$  and  $\Psi$ , along with the rescaled large  $\tau$  regime.** Figure 6.7(a) shows the time dimension rescaling function  $\Omega$  plotted against  $\Delta$  and figure 6.7(b) shows the probability dimension rescaling function  $\Psi$  plotted against  $\Delta$ . Figure 6.7(c) shows the rescaled simulation results, where the data collapse in the large  $\tau$  regime can be observed. The solid line shows is fitted to the large  $\tau$  portion and the gradient  $\theta_L$  is shown.

and noise strength is given by

$$e^{-(\psi(D)+\omega(D)\theta_L)\Delta+\theta_L c_1+c_2+c_3} \quad , \quad (6.9)$$

confirming the universal persistence probability for  $\Delta = 0$ , for all  $D$ . Finally, figure 6.7(c) shows the collapsed large  $\tau$  regime for the simulation results using a noise strength of  $D = 4.7 \times 10^8$ , that is representative of the amplitude required to stimulate dynamics on a scale required for the TCR:pMHC and LFA-1:ICAM-1 bonds. The data collapse suggests a universal scaling regime for the decay rate of the persistence probability during longer duration bond attachments.

The scaling functions also give some approximation for the range of  $\Delta$  where the method is valid. The linear fit, used to determine the functional relationships for the scaling variables with respect to  $\Delta$ , is a good fit for small  $\Delta$ , but the scaling variables begin to depart from the linear fit as  $\Delta$  increases and the statistics decrease significantly, see figures 6.7(a) and 6.7(b). The simulations have a low cut-off for  $\tau$ , the integration time step length  $\Delta t$ , that can be used to impose an upper limit on  $\Delta$  ( $\Delta_c$ ), such that the problem containing two distinct  $\tau$  regimes can be maintained. Beyond this critical value the small  $\tau$  regime shares the same dynamics as the large  $\tau$  regime and the problem reduces to one with a single  $\tau$  scaling regime. The biological interpretation of this regime would be one where only the TCR:pMHC bonds that have persisted long enough to begin signalling exist. The crossover point must be greater than the simulation step length, giving

$$\begin{aligned} \tau_x &\geq \Delta t \\ e^{-\omega(D)\Delta_c+c_1} &\geq \Delta t \\ \Delta_c &= \frac{c_1 - \log(\Delta t)}{\omega(D)} \end{aligned} \quad (6.10)$$

where  $\Delta_c$  is the critical threshold value for the two  $\tau$  regime problem.

Given  $c_1$  is constant, there is an inverse relationship between  $\Delta_c$  and  $\omega$ . For  $\Delta \geq 0$  as value of  $c_1 \geq \log(\Delta t)$  is required. As the noise level increases,  $\omega(D)$  gets smaller and subsequently the upper limit on  $\Delta$  increases. The upper limit calculated *over* estimates the range of  $\Delta$ , possibly due to the crude linear approximations for  $\Omega_\Delta$  and  $\Psi_\Delta$  for large  $\Delta$ .

## 6.4 Extremal Value Statistics

As shown in section 5.3, the average time persistence is a monotonically decreasing function of an increasing threshold value (Bush and Chattopadhyay, 2014). The fluctuations due to thermal noise lead to rapid crossings of the threshold as the separation distance moves

from a close contact phase to one of separation and vice-versa. This section presents the analysis concerning the extent to which these rapid crossings contribute to the average time persistence for the bonds.

The term *extremal value* is used to describe the time persistence realisations due to rapid fluctuations, where the bond life is extremely short. Table 6.2 shows the first three intervals of the normalised frequency distribution of  $t_\Delta$  for a range of  $\Delta$ . At least 50% of the statistics

$\Delta$ (nm)	First Passage Prob Time			Total
	$\Delta t$	$2\Delta t$	$3\Delta t$	
0	0.2945	0.1315	0.0789	0.5048
5	0.3072	0.1366	0.0818	0.5257
10	0.3201	0.1417	0.0846	0.5465
15	0.3333	0.1467	0.0873	0.5672
20	0.3466	0.1515	0.0897	0.5878
25	0.3601	0.1562	0.0919	0.6082
30	0.3738	0.1607	0.0939	0.6283

Table 6.2: **First passage probability frequencies for transient bonding.** The number of bonds that have a duration of 3 discrete time step lengths or less account for 50% or more of the statistics.

for each  $\Delta$  are accounted for in the first three discrete time steps. That is, at least a half of the bonds forming will dissociate in a fraction of a second.

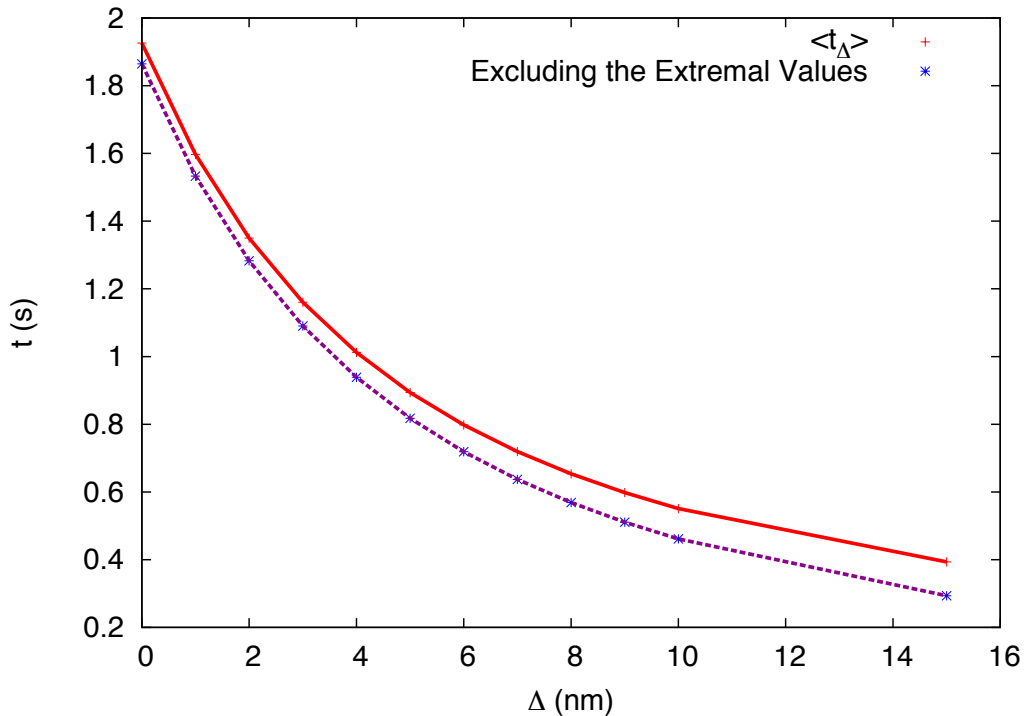


Figure 6.8: **Contribution of the extremal values to the average time persistence calculation.** The average time persistence plotted against  $\Delta$  (solid line), along with the average time persistence excluding the extremal events (dotted line).

The computer simulation results were used to calculate an approximate measure of the  $\Delta$ -dependent probability density function  $W_\Delta$ , equation (3.61), and this is used to calculate

the average time persistence. To assess the contribution of the extremal values to the total average, a lower cut-off,  $v \geq 0$ , is introduced to the first moment calculation

$$\langle t_{\Delta} \rangle = \int_v^{\infty} t W_{\Delta}(t) dt \quad (6.11)$$

that is used to exclude the extremal values from the calculation. A value of  $v = 3\Delta t$  is then used to exclude the statistics set out in table 6.2. Figure 6.8 shows  $\langle t_{\Delta} \rangle$  against  $\Delta$  (solid line) along with the corresponding average time persistence excluding the rapid fluctuations (dotted line), created using a  $D = 4.7 \times 10^8$  thermal noise strength. Increasing  $v$  will exclude a larger portion of the “thermal fluctuation regime”, eventually excluding the “signalling regime” as  $v$  becomes large.

For small  $\Delta$  the extremal values considered have very little contribution to the total average calculation, however the contribution steadily increases as  $\Delta$  increases. This can be understood from the statistical view presented in figure 6.1, where the statistics drop off as  $\Delta$  increases, leading to an increasing percentage of statistics in the small  $\tau$  regime as  $\Delta$  increases. This analysis is limited by the choice of  $v$  and future work aims to use the results of section 6.3 to ascertain the relative contribution of the “thermal fluctuation” regime against the “signalling” regime.

## 6.5 Discussion

From an estimation of the bond survival probability, it is shown that at shorter time scales, the survival probability  $P(\tau)$  scales with time  $\tau$  as a universal function of a rescaled noise amplitude  $D$ , such that  $P(\tau) \sim \tau^{-\left(\frac{\Delta}{\sqrt{D}} + \frac{1}{2}\right)}$ ,  $\Delta$  describing the TCR:pMHC bond length through the distance measure from the mean membrane separation distance. The crossover from this shorter time regime to a longer time regime leads to a loss of this universality property, at which point the survival probability changes from a scaled form to an exponential function of the mean bond length  $\Delta$ . In biological terms, such a crossover indicates that the TCR:pMHC bond has a survival probability with a slower decay rate than the longer LFA-1:ICAM-1 bond justifying its stability. The analysis presented defines a scaled noise amplitude ( $= \frac{D}{\Delta^2}$ ), the breakdown of whose scaling property identifies the crossover from the linear (immature) to the nonlinear (mature) synapse domain.

## Chapter 7

# Conclusion and Discussion

The biological literature review in chapter 1 reveals a lack of clarity regarding the formation of the mature IS, largely due to the spatio-temporal scale of the problem (nanometers and picoseconds). The mechanisms for TCR triggering and processes that drive the pattern formation have therefore inspired a number of hypotheses. The aim of this study was to analyse the temporal dynamics of cell surface bonds engaged during the *immature* phase of the IS formation, long before the *mature* synapse takes root. During the immature synapse phase, there are two different bonds (TCR:pMHC, LFA-1:ICAM-1) of great importance that are evident at the synapse juncture. The different bond length scales and cell membrane properties have been used in various mathematical models, to understand the dynamics underpinning the synapse formation. The temporal dynamics of the bond durations during the immature synapse phase was missing from the literature and this was the basis for the research questions outlined in section 1.4. Further analysis of the biological literature revealed TCR microclusters present in the pSMAC of the mature synapse, and the bond dynamics in this region could be seen as an analogous problem to that of the immature synapse.

The approach to the study was to use a previous model suggested for the immature synapse, detailed in section 2.2.1. This model was then analysed using a set of numerical and analytical methods, outlined in chapter 3. The single threshold model introduced in section 3.1.6 has been previously used to calculate the spatial patch size related to the TCR:pMHC bond, but it had not been applied to the temporal persistence of the patch sizes. This analysis is one of the contributions of knowledge to the field, supported by the published journal articles (Bush and Chattopadhyay, 2014; Bush and Chattopadhyay, 2015) and the manuscript under preparation (Bush and Chattopadhyay, 2016). The analysis led to the development of a two threshold model, described in section 5.2, that had not been previously presented. And it was this model that enabled the calculation of quantitative results, using the maximum likelihood probability for the persistence of the TCR:pMHC bond, defined by the distance between the two thresholds. The findings related to the research questions

addressed in this study are outlined in the sections below.

## 7.1 Average persistence time for the TCR:pMHC bond

The average persistence time for the TCR:pMHC bond in the immature synapse was calculated using both numerical and analytical methods. The results presented in chapter 5 suggest the persistence of the TCR:pMHC bond is in the order of 2-4 seconds. This result is in agreement with the order of magnitude of time, observed in biological experiments, for the biological markers related to signal transduction events. As noted earlier, the result is somewhat subjective, depending on the parameter values used. However, the parameter units used are calculated with time measured in seconds and therefore justifies the case for the proposed 2-4 seconds persistence time. A shortcoming in the results stems from the use of parameter values previously calculated in the original study by Chattopadhyay and Burroughs (2007). Therefore, any recent improvements on these calculations are not included in this study, although at the time of publishing, none have been identified.

The survival probability analysed in chapter 6 shows two distinct phases, a *thermal fluctuation* regime and a *signalling* regime, as shown in figure 6.3, corresponding to two separate time persistence exponents. The thermal fluctuation regime has a time exponent that is dependent on both the threshold bond length and the noise amplitude. As shown in figure 6.5, the exponent  $\alpha$  scales with the noise amplitude  $D$  thereby defining a “diffusive universality class” between  $\alpha$  and  $D$ , that quantifies into the rescaling of the noise amplitude as  $\frac{D}{\Delta^2}$ . From the perspective of a biologist, the above result implies that if the system is calibrated with respect to the dimensionless variable  $\frac{D}{\Delta^2}$  instead of the two variables  $D$  and  $\Delta$  independently, the fluctuation regime can be identified through a single-valued scaling exponent, and then ultimately the start of the signalling regime. For a signalling setup involving multiple coreceptor molecules with varying bond lengths, based on the results presented here, the above analysis could enable the prediction of the start of the signalling regime for a fixed noise input.

The signalling regime is identified by a universal time exponent that is defined by  $\theta_L$ , indicating a constant dissociation rate ( $k_{\text{off}}$ ). This result agrees with the findings of Burroughs and Wülfing (2002) and McKeithan (1995). However, these results do not consider the effects on the binding rates due to coreceptor bonding. The model is simplistic in its approximation of the binding parameters, where they remain constant throughout the synapse formation. Whereas, signals resulting from coreceptor bonding have been shown to increase the affinity for TCR:pMHC and LFA-1:ICAM-1 bonding, therefore an interesting future work would be to analyse the effects of these altered affinities on the persistence time calculated.

## 7.2 The effect of thermal fluctuations on the average persistence time for the TCR:pMHC bond

The calculation of the average time persistence contains statistics from the full probability density function. However, as mentioned above, there are two distinct regimes present in this probability density function. The contribution of the rapid membrane fluctuations, the *fluctuating* regime, to the average bond persistence is important to the biologist when inferring results from experiments. The results in chapter 6 show the maximum likelihood for bond persistence is one that is transient, engaging and disengaging spontaneously, figure 6.2. However, these rapidly fluctuating membrane dynamics appear to have little effect on the statistics and the survival probability profile may be well described excluding large amplitude fluctuations. This is visualised in figure 6.8, where it is clearly shown that extremal value statistics do not contribute greatly to the average time persistence in the linear stability region. These short-lived bonds are not consistent with the time required for TCR signalling, therefore this contribution to knowledge presents a *null hypothesis* of sorts. Many quantitative biological experiments and conclusions are based on singular or at best only a small number of observations. Such lack of statistical information implies that existing probabilistic theories, including previous immunological synapse based models, will be inadequate in dealing with such eventualities. A corollary of this present work is the development of a methodology to avoid having to explicitly deal with statistically large datasets, since at least for immature immunological synapse dynamics, the results clearly indicate that large amplitude fluctuations can be largely neglected in the statistical analysis, thereby limiting the available configuration space to a much smaller size than would otherwise be required.

## 7.3 Future Work

The work presented here is focused on the linearly stable region of the *immature* synapse. There are a number of exciting areas for future work, especially progressing to the nonlinear dynamics describing the onset of the mature synapse. The list below outlines some of the work that follows from this study:

- **Use the time-dependent Fokker-Planck equation to analyse the changing survival probability density profile during synapse formation.** Chapter 3 introduced the steady state Fokker-Planck equation to describe the probability density function of the Langevin equation. The time-dependent solution to the Fokker-Planck equation could be used to analyse the time evolution of the immature synapse. Extended to a non-linear mode, this would also indicate the immature to mature crossover timescale.

- **Analysis of the model parameter space through the use of the nonlinear SA model.** Using boundary values derived from experimental results, the parameter space for the SA model could be analysed. In this case, a set of solutions in the parametric space that lead to the mature synapse formation may be identified, leading to a better understanding of the sensitivity of the model to parameter values.

- **Inclusion of coreceptor, phosphatase and self-pMHC molecules to the SA model.**

Various studies have reproduced and analysed the SA model using the two bonds considered in this work (TCR:pMHC, LFA-1:ICAM-1). None have been identified that include the coreceptor molecules (CD2, CD28, CD4/CD8), the larger molecules (CD43, CD45) or major histocompatibility complex with bound self-peptide (self-pMHC). Numerous biological results exist concerning the dynamics of these molecules and their inclusion may expose interdependencies otherwise overlooked.

- **Introduction of the kinase-phosphatase pathways to the nonlinear model.**

There are a number of recent models analysing the binding kinetics of the Src-kinase signalling pathways, but there are no reports integrating the intracellular signalling with membrane models. In this case, the currently proposed models for signal transduction could be coupled with a nonlinear membrane model, in a way that promotes signal transduction for bound TCRs. The addition of the large phosphatase (CD45) to the membrane bound molecules would also need consideration, since the combination of Src-kinase signalling and large phosphatases appear to maintain the balance of phosphorylation and dephosphorylation required to regulate the intracellular signalling pathways.

- **Extension of the SA model to include the recent TCR microcluster experimental evidence.**

The SA model does not reproduce results consistent with the discovery of TCR microclusters (Yokosuka *et al.*, 2005). A suggestion to incorporate these, would be the inclusion of spatial dependent functions that introduce TCR microclusters in the pSMAC, once the mature synapse patterning is established. The inclusion of terms to model the spreading and contraction phases would also be required and terms to encapsulate the Src-kinase signalling, using a switching mechanism to arrest signalling once the microcluster has crossed the threshold between the pSMAC and cSMAC.

- **Apply the computer code base to alternative systems of coupled equations.**

The numerical methods undertaken in the present work have necessitated the development of a large code base. The routines have been developed in C++ and include

OpenMP functionality, capable of running parallel computations on multiprocessor systems. The design of the computer simulation code contains an object model with 30+ classes, is extensible and scalable, with capabilities of simulating nonlinear coupled equations across multiple processing nodes. In recognition of recent research council funding rules, this code will be made available through the Aston repository for other researchers.

- **Application of the method presented by Sire (2007), using the closed form solution derived in the asymptotic analysis.** The asymptotic solution derived for the large  $\tau$  regime could be combined with the steady state probability distribution derived from the Fokker-Planck equation. Together, they form the two inputs required to implement the method set out by Sire (2007), used to determine analytical results for  $\langle \tau_+ \rangle$  and  $\langle \tau_- \rangle$  for  $\Delta \neq 0$ . This work is currently being prepared for publication.

## Appendix A

# Linearised Steady State Model: Deriving the Langevin Equation for the Local Separation Distance

In this section we show the workings to derive the Langevin equation that arises from a linearisation of the SA model (Qi *et al.*, 2001) about a steady state equilibrium of surface protein concentration levels. We start with the nonlinear coupled equations (2.1) and linearise about fixed concentration levels, at time  $t_0$ , for both the freely diffusing surface proteins and the bond complexes. This leads to the set of steady state equations (A.1) for the cell surface concentration levels, the corresponding energy functional, equation (A.2), and the Langevin equation describing the membrane separation distance, equation (A.3),

$$\frac{\partial C_j}{\partial t} = 0, \quad C_j(\mathbf{x}, t_0) > 0, \quad j = T, Tt, M, Ai, Bi, TM, i \quad (\text{A.1})$$

$$\begin{aligned} F &= \frac{\lambda_T}{2} \int d\mathbf{x} C_{TM}(\mathbf{x}, t_0) \cdot [z(\mathbf{x}, t) - z_{TM}]^2 \\ &\quad + \sum_i \frac{\lambda_i}{2} \int d\mathbf{x} C_i(\mathbf{x}, t_0) \cdot [z(\mathbf{x}, t) - z_i]^2 \\ &\quad + \frac{1}{2} \int d\mathbf{x} \left[ \gamma(\nabla z(\mathbf{x}, t))^2 + \kappa(\nabla^2 z(\mathbf{x}, t))^2 \right] \end{aligned} \quad (\text{A.2})$$

$$\frac{\partial z}{\partial t} = -M \frac{\delta F}{\delta z} + \zeta. \quad (\text{A.3})$$

In such a case we can derive the form of the functional derivative for the free energy with respect to the local separation distance. The functional derivative can be defined as

$$\frac{\delta F}{\delta z(\mathbf{y}, t)} = \lim_{\epsilon \rightarrow 0} \frac{F(z(\mathbf{x}, t) + \epsilon \delta(\mathbf{x} - \mathbf{y})) - F(z(\mathbf{x}, t))}{\epsilon} \quad (\text{A.4})$$

where the use of the  $\delta$  function signifies the variation is only varied at the point  $\mathbf{y}$ . The justification of this lies in the fact this is a homogenous surface, whereupon the variation at

a single point is indicative of the variation at any point on the surface. For our case, the free energy function can be expressed as four separate terms

$$F^{(1)} = \frac{\lambda_T}{2} \int d\mathbf{x} C_{TM}(\mathbf{x}, t_0) \cdot [z(\mathbf{x}, t) - z_{TM}]^2 \quad (\text{A.5a})$$

$$F^{(2)} = \sum_i \frac{\lambda_i}{2} \int d\mathbf{x} C_i(\mathbf{x}, t_0) \cdot [z(\mathbf{x}, t) - z_i]^2 \quad (\text{A.5b})$$

$$F^{(3)} = \frac{1}{2} \int d\mathbf{x} \gamma [\nabla z(\mathbf{x}, t)]^2 \quad (\text{A.5c})$$

$$F^{(4)} = \frac{1}{2} \int d\mathbf{x} \kappa [\nabla^2 z(\mathbf{x}, t)]^2 \quad (\text{A.5d})$$

then

$$F = F^{(1)} + F^{(2)} + F^{(3)} + F^{(4)} \quad (\text{A.6})$$

and

$$\frac{\delta F}{\delta z(\mathbf{y}, t)} = \frac{\delta F^{(1)}}{\delta z(\mathbf{y}, t)} + \frac{\delta F^{(2)}}{\delta z(\mathbf{y}, t)} + \frac{\delta F^{(3)}}{\delta z(\mathbf{y}, t)} + \frac{\delta F^{(4)}}{\delta z(\mathbf{y}, t)} \quad (\text{A.7})$$

Calculating the functional derivative for the first term:

$$\frac{\delta F^{(1)}}{\delta z(\mathbf{y}, t)} = \lim_{\epsilon \rightarrow 0} \frac{F^{(1)}(z(\mathbf{x}, t) + \epsilon \delta(\mathbf{x} - \mathbf{y})) - F^{(1)}(z(\mathbf{x}, t))}{\epsilon} \quad (\text{A.8})$$

with

$$\begin{aligned} & F^{(1)}(z(\mathbf{x}, t) + \epsilon \delta(\mathbf{x} - \mathbf{y})) \\ &= \frac{\lambda_T}{2} \int d\mathbf{x} C_{TM}(\mathbf{x}, t_0) \cdot \left[ (z(\mathbf{x}, t) - z_{TM})^2 + 2\epsilon (z(\mathbf{x}, t) - z_{TM}) \delta(\mathbf{x} - \mathbf{y}) \right] \end{aligned}$$

where  $\epsilon$  orders greater than two have been omitted, then

$$\begin{aligned} \frac{\delta F^{(1)}}{\delta z(\mathbf{y}, t)} &= \lambda_T \int d\mathbf{x} C_{TM}(\mathbf{x}, t_0) \cdot (z(\mathbf{x}, t) - z_{TM}) \delta(\mathbf{x} - \mathbf{y}) \\ &= \lambda_T C_{TM}(\mathbf{y}, t_0) \cdot (z(\mathbf{y}, t) - z_{TM}) \end{aligned} \quad (\text{A.9})$$

and similarly,

$$\frac{\delta F^{(2)}}{\delta z(\mathbf{y}, t)} = \sum_i \lambda_i C_i(\mathbf{y}, t_0) \cdot (z(\mathbf{y}, t) - z_i) \quad (\text{A.10})$$

For the third term, we get

$$\begin{aligned}
\frac{\delta F^{(3)}}{\delta z(\mathbf{y}, t)} &= \lim_{\epsilon \rightarrow 0} \frac{\frac{1}{2} \int d\mathbf{x} \gamma (\nabla (z(\mathbf{x}, t) + \epsilon \delta(\mathbf{x} - \mathbf{y})))^2 - \frac{1}{2} \int d\mathbf{x} \gamma (\nabla z(\mathbf{x}, t))^2}{\epsilon} \\
&= \lim_{\epsilon \rightarrow 0} \frac{\frac{1}{2} \int d\mathbf{x} \gamma \left[ (\nabla z(\mathbf{x}, t))^2 + 2\epsilon \nabla z(\mathbf{x}, t) \cdot \nabla \delta(\mathbf{x} - \mathbf{y}) \right] - \frac{1}{2} \int d\mathbf{x} \gamma (\nabla z(\mathbf{x}, t))^2}{\epsilon} \\
&= \gamma \int d\mathbf{x} \nabla z(\mathbf{x}, t) \cdot \nabla \delta(\mathbf{x} - \mathbf{y}) \\
&= -\gamma \int d\mathbf{x} \nabla^2 z(\mathbf{x}, t) \delta(\mathbf{x} - \mathbf{y}) \\
&= -\gamma \nabla^2 z(\mathbf{y}, t)
\end{aligned} \tag{A.11}$$

where the fourth line is derived from applying integration by parts, and noting the boundary integral cancels for periodic boundary conditions. Similarly, the fourth term is given by

$$\begin{aligned}
\frac{\delta F^{(4)}}{\delta z} &= \lim_{\epsilon \rightarrow 0} \frac{\frac{1}{2} \int d\mathbf{x} \kappa (\nabla^2 (z(\mathbf{x}, t) + \epsilon \delta(\mathbf{x} - \mathbf{y})))^2 - \frac{1}{2} \int d\mathbf{x} \kappa (\nabla^2 z(\mathbf{x}, t))^2}{\epsilon} \\
&= \lim_{\epsilon \rightarrow 0} \frac{\frac{1}{2} \int d\mathbf{x} \kappa \left[ (\nabla^2 z(\mathbf{x}, t))^2 + 2\epsilon \nabla^2 z(\mathbf{x}, t) \cdot \nabla^2 \delta(\mathbf{x} - \mathbf{y}) \right] - \frac{1}{2} \int d\mathbf{x} \kappa (\nabla^2 z(\mathbf{x}, t))^2}{\epsilon} \\
&= \kappa \int d\mathbf{x} \nabla^2 z(\mathbf{x}, t) \cdot \nabla^2 \delta(\mathbf{x} - \mathbf{y}) \\
&= \kappa \int d\mathbf{x} \nabla^4 z(\mathbf{x}, t) \delta(\mathbf{x} - \mathbf{y}) \\
&= \kappa \nabla^4 z(\mathbf{y}, t)
\end{aligned} \tag{A.12}$$

Then the full functional derivative for the potential force is given by

$$\frac{\delta F}{\delta z} = \lambda z(\mathbf{y}, t) - \sigma - \gamma \nabla^2 z(\mathbf{y}, t) + \kappa \nabla^4 z(\mathbf{y}, t) \tag{A.13}$$

where

$$\lambda = \lambda_T C_{TM}(\mathbf{y}, t_0) + \sum_i \lambda_i C_i(\mathbf{y}, t_0) \tag{A.14}$$

and

$$\sigma = \lambda_T C_{TM}(\mathbf{y}, t_0) z_{TM} + \sum_i \lambda_i C_i(\mathbf{y}, t_0) z_i \tag{A.15}$$

Then the time difference formula for the local membrane separation distance is given by

$$\frac{\partial z(\mathbf{x}, t)}{\partial t} = -M [\lambda z(\mathbf{x}, t) - \sigma - \gamma \nabla^2 z(\mathbf{x}, t) + \kappa \nabla^4 z(\mathbf{x}, t)] + \zeta \tag{A.16}$$

Another calculation that is useful is the functional derivative of the free energy with respect

to the concentration level of a surface protein

$$\begin{aligned}
\frac{\delta F}{\delta C_i(\mathbf{y}, t)} &= \lim_{\epsilon \rightarrow 0} \frac{F(C_i(\mathbf{x}, t) + \epsilon \delta(\mathbf{x} - \mathbf{y})) - F(C_i(\mathbf{x}, t))}{\epsilon} \\
&= \lim_{\epsilon \rightarrow 0} \frac{\frac{\lambda_i}{2} \int d\mathbf{x} [C_i(\mathbf{x}, t) + \epsilon \delta(\mathbf{x} - \mathbf{y})] \cdot [z(\mathbf{x}, t) - z_i]^2 - \frac{\lambda_i}{2} \int d\mathbf{x} C_i(\mathbf{x}, t) \cdot [z(\mathbf{x}, t) - z_i]^2}{\epsilon} \\
&= \lim_{\epsilon \rightarrow 0} \frac{\frac{\lambda_i}{2} \int d\mathbf{x} \epsilon \delta(\mathbf{x} - \mathbf{y}) \cdot [z(\mathbf{x}, t) - z_i]^2}{\epsilon} \\
&= \frac{\lambda_i}{2} \int d\mathbf{x} [z(\mathbf{x}, t) - z_i]^2 \delta(\mathbf{x} - \mathbf{y}) \\
&= \frac{\lambda_i}{2} [z(\mathbf{y}, t) - z_i]^2
\end{aligned} \tag{A.17}$$

that is required when analysing the full nonlinear model.

## Appendix B

# Integral Equation Solution to the Langevin Equation

In this section we use a Fourier transform method to develop a solution for the linear stochastic model (cf. equation (2.12))

$$M \frac{\partial z(\mathbf{x}, t)}{\partial t} = -B \nabla^4 z(\mathbf{x}, t) + \gamma \nabla^2 z(\mathbf{x}, t) - \lambda z(\mathbf{x}, t) + \eta(\mathbf{x}, t) \quad (\text{B.1a})$$

$$\langle \eta(\mathbf{x}, t) \rangle = 0 \quad (\text{B.1b})$$

$$\langle \eta(\mathbf{x}, t) \eta(\mathbf{x}', t') \rangle = 2D \delta(\mathbf{x} - \mathbf{x}') \delta(t - t') \quad (\text{B.1c})$$

where the points on the 2 dimensional surface are represented by the vector  $\mathbf{x} = \begin{bmatrix} x & y \end{bmatrix}^T$ . We consider a small spatial region,  $\Omega$ , in the synaptic junction, that is large enough to contain a significant number of surface protein molecules. The full synaptic junction can then be represented by  $N$  simply connected,  $\Omega$  subregions. The subregions at the centre of the synapse, far from the boundary, are surrounded by similar nearest neighbours that are equally far from the boundary. In this case, we use periodic boundary conditions for these central subregions, such that there is zero net flow across the boundary. Then, the corresponding Fourier transform pairs for the membrane separation distance,  $z(\mathbf{x}, t)$ , and the thermal noise  $\eta(\mathbf{x}, t)$  are given by

$$\mathcal{F}\{z(\mathbf{x}, t)\} = \tilde{z}(\mathbf{k}, t) = \frac{1}{2\pi} \int_{\Omega} z(\mathbf{x}, t) e^{-i\mathbf{k}\cdot\mathbf{x}} d\mathbf{x} \quad (\text{B.2a})$$

$$\mathcal{F}^{-1}\{\tilde{z}(\mathbf{k}, t)\} = z(\mathbf{x}, t) = \frac{1}{2\pi} \int_{-\infty}^{\infty} \tilde{z}(\mathbf{k}, t) e^{i\mathbf{k}\cdot\mathbf{x}} d\mathbf{k} \quad (\text{B.2b})$$

$$\mathcal{F}\{\eta(\mathbf{x}, t)\} = \tilde{\eta}(\mathbf{k}, t) = \frac{1}{2\pi} \int_{\Omega} \eta(\mathbf{x}, t) e^{-i\mathbf{k}\cdot\mathbf{x}} d\mathbf{x} \quad (\text{B.2c})$$

$$\mathcal{F}^{-1}\{\tilde{\eta}(\mathbf{k}, t)\} = \eta(\mathbf{x}, t) = \frac{1}{2\pi} \int_{-\infty}^{\infty} \tilde{\eta}(\mathbf{k}, t) e^{i\mathbf{k}\cdot\mathbf{x}} d\mathbf{k} \quad (\text{B.2d})$$

$$(\text{B.3})$$

where  $\mathbf{k} = \begin{bmatrix} k_1 & k_2 \end{bmatrix}^T$ .

Applying the Fourier transforms to equation (B.1)

$$\mathcal{F} \left\{ \frac{\partial z(\mathbf{x}, t)}{\partial t} \right\} = -B\mathcal{F} \{ \nabla^4 z(\mathbf{x}, t) \} + \gamma\mathcal{F} \{ \nabla^2 z(\mathbf{x}, t) \} - \lambda\mathcal{F} \{ z(\mathbf{x}, t) \} + \mathcal{F} \{ \eta(\mathbf{x}, t) \} \quad (\text{B.4})$$

The Laplacian term may be treated like so

$$\begin{aligned} \mathcal{F} \{ \nabla^2 z(\mathbf{x}, t) \} &= \mathcal{F} \{ \nabla^2 z(x, y, t) \} \\ &= \mathcal{F} \{ \nabla \cdot \nabla z(x, y, t) \} \\ &= \mathcal{F} \left\{ \left( \mathbf{i} \frac{\partial}{\partial x} + \mathbf{j} \frac{\partial}{\partial y} \right) \cdot \left( \mathbf{i} \frac{\partial z(x, y, t)}{\partial x} + \mathbf{j} \frac{\partial z(x, y, t)}{\partial y} \right) \right\} \\ &= \mathcal{F} \left\{ \frac{\partial^2 z(x, y, t)}{\partial x^2} + \frac{\partial^2 z(x, y, t)}{\partial y^2} \right\} \\ &= \frac{\partial^2 \mathcal{F} \{ z(x, y, t) \}}{\partial x^2} + \frac{\partial^2 \mathcal{F} \{ z(x, y, t) \}}{\partial y^2} \end{aligned} \quad (\text{B.5})$$

then, using equation (B.2a),

$$\begin{aligned} \mathcal{F} \{ \nabla^2 z(\mathbf{x}, t) \} &= (ik_1)^2 \mathcal{F} \{ z(x, y, t) \} + (ik_2)^2 \mathcal{F} \{ z(x, y, t) \} \\ &= -(k_1^2 + k_2^2) \mathcal{F} \{ z(x, y, t) \} \\ &= -|\mathbf{k}|^2 \mathcal{F} \{ z(x, y, t) \} \end{aligned} \quad (\text{B.6})$$

. Similarly,

$$\begin{aligned} \mathcal{F} \{ \nabla^4 z(\mathbf{x}, t) \} &= \mathcal{F} \{ \nabla^4 z(x, y, t) \} \\ &= \frac{\partial^4 \mathcal{F} \{ z(x, y, t) \}}{\partial x^4} + \frac{\partial^4 \mathcal{F} \{ z(x, y, t) \}}{\partial y^4} + 2 \frac{\partial^4 \mathcal{F} \{ z(x, y, t) \}}{\partial y^2 \partial x^2} \\ &= (ik_1)^4 \mathcal{F} \{ z(x, y, t) \} + (ik_2)^4 \mathcal{F} \{ z(x, y, t) \} + 2(ik_1)^2 (ik_2)^2 \mathcal{F} \{ z(x, y, t) \} \\ &= (k_1^2 + k_2^2)^2 \mathcal{F} \{ z(x, y, t) \} \\ &= |\mathbf{k}|^4 \mathcal{F} \{ z(x, y, t) \} \end{aligned} \quad (\text{B.7})$$

whereupon, equation (B.4) can be written as

$$M \frac{\partial \tilde{z}(\mathbf{k}, t)}{\partial t} = - \left( B|\mathbf{k}|^4 + \gamma|\mathbf{k}|^2 + \lambda \right) \tilde{z}(\mathbf{k}, t) + \tilde{\eta}(\mathbf{k}, t) \quad (\text{B.8})$$

then

$$\frac{\partial \tilde{z}(\mathbf{k}, t)}{\partial t} + \alpha(\mathbf{k}) \tilde{z}(\mathbf{k}, t) = \frac{1}{M} \tilde{\eta}(\mathbf{k}, t) \quad (\text{B.9})$$

where

$$\alpha(\mathbf{k}) = \frac{1}{M} \left( B|\mathbf{k}|^4 + \gamma|\mathbf{k}|^2 + \lambda \right) \quad (\text{B.10})$$

Equation (B.9) can be solved using the integrating factor method, to give

$$\tilde{z}(\mathbf{k}, t) = e^{-\alpha(\mathbf{k})t} \left[ \frac{1}{M} \int_{t_0}^t e^{\alpha(\mathbf{k})t'} \tilde{\eta}(\mathbf{k}, t') dt' + \tilde{z}_0(\mathbf{k}, t_0) \right] \quad (\text{B.11})$$

where the function  $\tilde{z}_0(\mathbf{k}, t_0)$  represents the initial conditions (in the spectral domain) at time  $t_0$ . Finally, applying the inverse Fourier transform, equation B.2b, gives the integral equation solution

$$\begin{aligned} z(\mathbf{x}, t) &= \frac{1}{2\pi} \int_{-\infty}^{\infty} d\mathbf{k} e^{-\alpha(\mathbf{k})t} \left[ \frac{1}{M} \int_{t_0}^t e^{\alpha(\mathbf{k})t'} \tilde{\eta}(\mathbf{k}, t') dt' + \tilde{z}_0(\mathbf{k}, t_0) \right] e^{i\mathbf{k}\cdot\mathbf{x}} \\ z(\mathbf{x}, t) &= \frac{1}{2\pi M} \int_{-\infty}^{\infty} d\mathbf{k} \int_{t_0}^t dt' e^{-\alpha(\mathbf{k})(t-t') + i\mathbf{k}\cdot\mathbf{x}} \tilde{\eta}(\mathbf{k}, t') + z_0(\mathbf{x}, t, t_0) \end{aligned} \quad (\text{B.12})$$

where the initial conditions are embedded in the  $z_0(\mathbf{x}, t, t_0)$  function

$$z_0(\mathbf{x}, t, t_0) = \frac{1}{2\pi} \int_{-\infty}^{\infty} d\mathbf{k} \tilde{z}_0(\mathbf{k}, t_0) e^{-\alpha(\mathbf{k})t} e^{i\mathbf{k}\cdot\mathbf{x}} = \mathcal{F}^{-1} \left\{ \tilde{z}_0(\mathbf{k}, t_0) e^{-\alpha(\mathbf{k})t} \right\} \quad (\text{B.13})$$

## Appendix C

# Temporal Correlation Function

### C.1 Temporal Correlation $\langle z(\mathbf{x}, t_1) z(\mathbf{x}, t_2) \rangle$

The temporal correlation of the fluctuations in the inter-membrane separation distance, at a point in the synaptic junction, is given by

$$\begin{aligned} \langle z(\mathbf{x}, t_1) z(\mathbf{x}, t_2) \rangle = & \left\langle \left[ \frac{1}{(2\pi)^{d/2} M} \int d^d k' \int_{t_0}^{t_1} dt' e^{-\alpha(\mathbf{k}')(t_1-t') + i\mathbf{k}' \cdot \mathbf{x}} \tilde{\eta}(\mathbf{k}', t') + z_0(\mathbf{x}, t_0) \right] \right. \\ & \left. \times \left[ \frac{1}{(2\pi)^{d/2} M} \int d^d k'' \int_{t_0}^{t_2} dt'' e^{-\alpha(\mathbf{k}'')(t_2-t'') + i\mathbf{k}'' \cdot \mathbf{x}} \tilde{\eta}(\mathbf{k}'', t'') + z_0(\mathbf{x}, t_0) \right] \right\rangle \end{aligned} \quad (\text{C.1})$$

Now, only the stochastic noise term,  $\tilde{\eta}(\mathbf{k}, t)$ , has variation in the ensemble. The first two cumulants in the  $k$ - $t$  space are given by <sup>1</sup>

$$\begin{aligned} \langle \tilde{\eta}(\mathbf{k}, t) \rangle &= 0 \\ \langle \tilde{\eta}(\mathbf{k}, t) \tilde{\eta}(\mathbf{k}', t') \rangle &= 2D \delta^d(\mathbf{k} + \mathbf{k}') \delta(t - t') \end{aligned}$$

then equation (C.1) can be written

$$\begin{aligned} \langle z(\mathbf{x}, t_1) z(\mathbf{x}, t_2) \rangle = & \frac{1}{(2\pi)^d M^2} \int d^d k' \int d^d k'' e^{-\alpha(\mathbf{k}')t_1 - \alpha(\mathbf{k}'')t_2 + i(\mathbf{k}' + \mathbf{k}'') \cdot \mathbf{x}} \\ & \times \int_{t_0}^{t_1} dt' \int_{t_0}^{t_2} dt'' e^{\alpha(\mathbf{k}')t' + \alpha(\mathbf{k}'')t''} \langle \tilde{\eta}(\mathbf{k}', t') \tilde{\eta}(\mathbf{k}'', t'') \rangle + z_0 \end{aligned} \quad (\text{C.2})$$

$$\begin{aligned} \langle z(\mathbf{x}, t_1) z(\mathbf{x}, t_2) \rangle = & \frac{2D}{(2\pi)^d M^2} \int d^d k' \int d^d k'' e^{-\alpha(\mathbf{k}')t_1 - \alpha(\mathbf{k}'')t_2 + i(\mathbf{k}' + \mathbf{k}'') \cdot \mathbf{x}} \\ & \times \int_{t_0}^{t_1} dt' \int_{t_0}^{t_2} dt'' e^{\alpha(\mathbf{k}')t' + \alpha(\mathbf{k}'')t''} \delta(\mathbf{k}' + \mathbf{k}'') \delta(t' - t'') + z_0 \end{aligned} \quad (\text{C.3})$$

<sup>1</sup>The transformation from the  $x$ - $t$  space to the  $k$ - $t$  space for the second cumulant is outlined in appendix C.2

where

$$z_0 = z_0^2(\mathbf{x}, t_0) = \frac{1}{(2\pi)^d} \int d^d k' \int d^d k'' \tilde{z}_0(\mathbf{k}', t_0) \tilde{z}_0(\mathbf{k}'', t_0) e^{-(\alpha(\mathbf{k}') + \alpha(\mathbf{k}''))t_0 + i(\mathbf{k}' + \mathbf{k}'') \cdot \mathbf{x}} \quad (\text{C.4})$$

Now,  $\delta(\mathbf{k}' + \mathbf{k}'') = 0$  everywhere except for  $\mathbf{k}' = -\mathbf{k}''$ , where  $\int d^d k' \int d^d k'' \delta(\mathbf{k}' + \mathbf{k}'') = 1$ . We also note that  $\alpha(\mathbf{k}) = \alpha(-\mathbf{k})$ , then equation (C.2) can be written

$$\langle z(\mathbf{x}, t_1) z(\mathbf{x}, t_2) \rangle = \frac{2D}{(2\pi)^d M^2} \int d^d k e^{-\alpha(\mathbf{k})(t_1+t_2)} \int_{t_0}^{t_1} dt' \int_{t_0}^{t_2} dt'' e^{\alpha(\mathbf{k})(t'+t'')} \delta(t' - t'') + z_0 \quad (\text{C.5})$$

Now,  $\delta(t' - t'') = 1$  when  $t'' = t'$  and is zero everywhere else. Therefore, we can use a single integral over the range 0 to  $\min(t_1, t_2)$ , since values above the minimum will fall outside the delta excitation definition. For example, if  $t_1 < t_2$ , then values of  $t''$  greater than  $t_1$  will result in  $\delta(t' - t'') = 0$ , giving

$$\langle z(\mathbf{x}, t_1) z(\mathbf{x}, t_2) \rangle = \frac{2D}{(2\pi)^d M^2} \int d^d k e^{-\alpha(\mathbf{k})(t_1+t_2)} \int_{t_0}^{\min(t_1, t_2)} dt' e^{2\alpha(\mathbf{k})t'} + z_0 \quad (\text{C.6})$$

$$\begin{aligned} \langle z(\mathbf{x}, t_1) z(\mathbf{x}, t_2) \rangle &= \frac{2D}{(2\pi)^d M^2} \int d^d k e^{-\alpha(\mathbf{k})(t_1+t_2)} \left[ \frac{1}{2\alpha(\mathbf{k})} e^{2\alpha(\mathbf{k})t} \right]_{t_0}^{\min(t_1, t_2)} + z_0 \\ &= \frac{D}{(2\pi)^d M^2} \int d^d k e^{-\alpha(\mathbf{k})(t_1+t_2)} \left[ \frac{e^{2\alpha(\mathbf{k})\min(t_1, t_2)} - e^{2\alpha(\mathbf{k})t_0}}{\alpha(\mathbf{k})} \right] + z_0 \\ &= \frac{D}{(2\pi)^d M^2} \int d^d k \frac{e^{-\alpha(\mathbf{k})(\max(t_1, t_2) - \min(t_1, t_2))}}{\alpha(\mathbf{k})} \\ &\quad - \frac{D}{(2\pi)^d M^2} \int d^d k \frac{e^{-\alpha(\mathbf{k})(t_1+t_2-2t_0)}}{\alpha(\mathbf{k})} + z_0 \\ &= \frac{D}{(2\pi)^d M^2} \int d^d k \frac{e^{-\alpha(\mathbf{k})(\max(t_1, t_2) - \min(t_1, t_2))}}{\alpha(\mathbf{k})} \\ &\quad - \frac{D}{(2\pi)^d M^2} \int d^d k \frac{e^{-\alpha(\mathbf{k})(\max(t_1, t_2) - \min(t_1, t_2) + 2(\min(t_1, t_2) - t_0))}}{\alpha(\mathbf{k})} \\ &\quad + z_0 \end{aligned} \quad (\text{C.7})$$

Let  $\tau = \max(t_1, t_2) - \min(t_1, t_2)$  and  $\tau' = t_1 + t_2$ , then

$$\begin{aligned} \langle z(\mathbf{x}, t_1) z(\mathbf{x}, t_2) \rangle &= \frac{D}{(2\pi)^d M^2} \int d^d k \frac{e^{-\alpha(\mathbf{k})\tau}}{\alpha(\mathbf{k})} \\ &\quad - \frac{D}{(2\pi)^d M^2} \int d^d k \frac{e^{-\alpha(\mathbf{k})(\tau' - 2t_0)}}{\alpha(\mathbf{k})} + z_0 \end{aligned} \quad (\text{C.8})$$

Equation C.8 describes the two-point time correlation for all times, given initial condition  $z_0$ .

For models with  $d = 2$ , i.e. membranes with no overhangs, we can express the function by a substitution for  $d$  in equation (C.8) and transform to use polar co-ordinates,  $r$  and  $\theta$ .

Let

$$\mathbf{k} = \begin{bmatrix} k_1 \\ k_2 \end{bmatrix} = \begin{bmatrix} g(r, \theta) \\ h(r, \theta) \end{bmatrix} = \begin{bmatrix} r \cos \theta \\ r \sin \theta \end{bmatrix} \quad (\text{C.9})$$

where  $r$  is the distance from the origin ranging from  $0 < r < \infty$ , satisfying  $r^2 = k_1^2 + k_2^2$ ; and  $\theta$  is the angle made with the  $k_1$  axis, i.e.  $\tan(\theta) = \frac{k_2}{k_1}$  ranging from  $0$  to  $\pi$ . We note

$$\begin{aligned} \mathbf{k}^2 &= \mathbf{k} \cdot \mathbf{k} \\ &= r^2 \cos^2 \theta + r^2 \sin^2 \theta = r^2(\cos^2 \theta + \sin^2 \theta) \\ &= r^2 \end{aligned} \quad (\text{C.10})$$

and

$$\mathbf{k}^4 = \mathbf{k}^2 \cdot \mathbf{k}^2 = r^4 \quad (\text{C.11})$$

whereupon the transformation of  $\alpha(\mathbf{k})$  on to the new co-ordinates gives a function that relies on  $r$  alone

$$\alpha(\mathbf{k}) = \hat{\alpha}(r) = \frac{Br^4 + \gamma r^2 + \lambda}{M} \quad (\text{C.12})$$

We also calculate the determinant of the Jacobian for the transformation pair

$$\begin{aligned} \frac{\partial(g, h)}{\partial(r, \theta)} &= \begin{vmatrix} \frac{\partial g}{\partial r} & \frac{\partial g}{\partial \theta} \\ \frac{\partial h}{\partial r} & \frac{\partial h}{\partial \theta} \end{vmatrix} \\ &= \frac{\partial g}{\partial r} \frac{\partial h}{\partial \theta} - \frac{\partial h}{\partial r} \frac{\partial g}{\partial \theta} \\ &= r \cos^2 \theta + r \sin^2 \theta \\ &= r \end{aligned} \quad (\text{C.13})$$

and then we can transform the integrals in equation C.8 to the new co-ordinate system using

$$\int_{-\infty}^{\infty} \int_{-\infty}^{\infty} f(\mathbf{k}) d\mathbf{k} = \int_{-\pi}^{\pi} \int_0^{\infty} f(g(r, \theta), h(r, \theta)) \frac{\partial(g, h)}{\partial(r, \theta)} dr d\theta \quad (\text{C.14})$$

to give

$$\begin{aligned} \int_{-\infty}^{\infty} \int_{-\infty}^{\infty} \frac{e^{-\alpha(\mathbf{k})\tau}}{\alpha(\mathbf{k})} &= \int_{-\pi}^{\pi} \int_0^{\infty} r \frac{e^{-\hat{\alpha}(r)\tau}}{\hat{\alpha}(r)} dr d\theta \\ &= 2\pi \int_0^{\infty} r \frac{e^{-\hat{\alpha}(r)\tau}}{\hat{\alpha}(r)} dr \end{aligned} \quad (\text{C.15})$$

Then, the two-point correlation function can be expressed as

$$\begin{aligned}\langle z(\mathbf{x}, t_1)z(\mathbf{x}, t_2) \rangle &= \frac{D}{(2\pi)^2 M^2} \left[ \int d\mathbf{k} \frac{e^{-\alpha(\mathbf{k})\tau}}{\alpha(\mathbf{k})} - \int d\mathbf{k} \frac{e^{-\alpha(\mathbf{k})(\tau'-2t_0)}}{\alpha(\mathbf{k})} \right] + z_0 \\ &= \frac{D}{(2\pi) M^2} \left[ \int_0^\infty r \frac{e^{-\hat{\alpha}(r)\tau}}{\hat{\alpha}(r)} dr - \int_0^\infty r \frac{e^{-\hat{\alpha}(r)(\tau'-2t_0)}}{\hat{\alpha}(r)} dr \right] + z_0 \quad (\text{C.16})\end{aligned}$$

## C.2 Spatial Langevin Force in the $k$ -space

Here we show the workings for the  $k$ -space Langevin force. First consider the Fourier transform pair

$$f(\vec{x}) = \frac{1}{(2\pi)^{d/2}} \int_{-\infty}^{\infty} \tilde{f}(\vec{k}) e^{i\vec{k}\cdot\vec{x}} d^d k \quad (\text{C.17})$$

$$\tilde{f}(\vec{k}) = \frac{1}{(2\pi)^{d/2}} \int_{-\infty}^{\infty} f(\vec{x}) e^{-i\vec{k}\cdot\vec{x}} d^d x \quad (\text{C.18})$$

Now,

$$f(\vec{x}, \vec{x}') = \frac{1}{(2\pi)^d} \int_{-\infty}^{\infty} d^d k \int_{-\infty}^{\infty} d^d k' \tilde{f}(\vec{k}, \vec{k}') e^{i\vec{k}\cdot\vec{x}} e^{i\vec{k}'\cdot\vec{x}'} \quad (\text{C.19})$$

$$\tilde{f}(\vec{k}, \vec{k}') = \frac{1}{(2\pi)^d} \int_{-\infty}^{\infty} d^d x \int_{-\infty}^{\infty} d^d x' f(\vec{x}, \vec{x}') e^{-i\vec{k}\cdot\vec{x}} e^{-i\vec{k}'\cdot\vec{x}'} \quad (\text{C.20})$$

when  $f(\vec{x}, \vec{x}') = \delta^d(\vec{x} - \vec{x}')$  then

$$\tilde{f}(\vec{k}, \vec{k}') = \frac{1}{(2\pi)^d} \int_{-\infty}^{\infty} d^d x \int_{-\infty}^{\infty} d^d x' \delta^d(\vec{x} - \vec{x}') e^{-i(\vec{k}\cdot\vec{x} + \vec{k}'\cdot\vec{x}')} \quad (\text{C.21})$$

then  $\delta^d(\vec{x} - \vec{x}') = 1$  when  $\vec{x} = \vec{x}'$ , giving

$$\begin{aligned}\tilde{f}(\vec{k}, \vec{k}') &= \frac{1}{(2\pi)^d} \int_{-\infty}^{\infty} d^d x' e^{-i(\vec{k} + \vec{k}')\cdot\vec{x}'} \\ &= \delta(\vec{k} + \vec{k}')\end{aligned} \quad (\text{C.22})$$

## Appendix D

# Residue Theorem “Null” Solution of the Temporal Correlation Function

The analysis below was used as an attempt to determine a closed form solution of the temporal correlation function describe by equation (3.21) by using the residue theorem for complex integration with poles. For demonstration purposes we consider the just the Gaussian Stationary Process related integral term

$$C_{12}(\tau) \sim \int_0^\infty r \frac{e^{-\alpha(r)\tau}}{\alpha(r)} dr \quad (\text{D.1})$$

where

$$\alpha(r) = \frac{Br^4 + \gamma r^2 + \lambda}{M} \quad (\text{D.2})$$

As we shall see, the method fails for the type of equation above. We begin by defining the poles of the  $1/\alpha(r)$ , and these exist when

$$\alpha(r) = 0 \quad (\text{D.3})$$

It is clear to see at this point that the exponential term is 1 at the poles, and therefore the  $\tau$  dependency is lost. However, we proceed with the full calculation, as this was not initially well understood. Let  $r_0$  be a pole such that

$$\frac{Br_0^4 + \gamma r_0^2 + \lambda}{M} = 0 \quad (\text{D.4})$$

then the poles exist at

$$r_0 = \pm \sqrt{\frac{-\gamma \pm \sqrt{\gamma^2 - 4B\lambda}}{2B}} \quad (\text{D.5})$$

Given the problem parameter values specified in Chattopadhyay and Burroughs (2007) [28] ( $M = 4.7 \times 10^6 K_B T$ ,  $B = 11.8 K_B T$ ,  $\gamma = 5650 K_B T \mu\text{m}^{-2}$  and  $\lambda = 6 \times 10^5 K_B T \mu\text{m}^{-4}$ ), we can evaluate the terms in equation (D.5) to give the four purely imaginary roots, that are two sets of complex conjugates

$$\begin{aligned} r_0^{(1)} &= iC_1, & r_0^{(2)} &= iC_2 \\ r_0^{(3)} &= -iC_1, & r_0^{(4)} &= -iC_2 \end{aligned}$$

with  $C_1 = 12.609 \mu\text{m}^{-1}$  and  $C_2 = 17.884 \mu\text{m}^{-1}$ . Then using repeated partial fraction decomposition we can rearrange

$$\begin{aligned} \frac{1}{\alpha(r)} &= \frac{M}{B} \left[ \frac{1}{(r - r_0^{(1)})(r - r_0^{(2)})(r - r_0^{(3)})(r - r_0^{(4)})} \right] \\ &= \frac{M}{B} \left[ \frac{1}{(r - iC_1)(r - iC_2)(r + iC_1)(r + iC_2)} \right] \\ &= \frac{M}{B} \left( \frac{1}{(C_1 - C_2)^2} \left[ \frac{1}{(r - iC_1)(r + iC_1)} - \frac{1}{(r - iC_2)(r + iC_2)} \right. \right. \\ &\quad \left. \left. - \frac{1}{(r - iC_1)(r + iC_2)} + \frac{1}{(r - iC_2)(r + iC_1)} \right] \right) \\ &= \frac{M}{B(C_1 - C_2)^2} \left( \frac{1}{i2C_1} - \frac{1}{i(C_1 + C_2)} \right) \frac{1}{(r - iC_1)} \\ &\quad + \frac{M}{B(C_1 - C_2)^2} \left( \frac{1}{i(C_1 + C_2)} - \frac{1}{i2C_1} \right) \frac{1}{(r + iC_1)} \\ &\quad + \frac{M}{B(C_1 - C_2)^2} \left( \frac{1}{i2C_2} - \frac{1}{i(C_1 + C_2)} \right) \frac{1}{(r - iC_2)} \\ &\quad + \frac{M}{B(C_1 - C_2)^2} \left( \frac{1}{i(C_1 + C_2)} - \frac{1}{i2C_2} \right) \frac{1}{(r + iC_2)} \end{aligned}$$

and finally

$$\frac{1}{\alpha(r)} = \frac{iA_1}{(r - iC_1)} + \frac{iA_2}{(r - iC_2)} - \frac{iA_3}{(r + iC_1)} - \frac{iA_4}{(r + iC_2)} \quad (\text{D.6})$$

where

$$\begin{aligned} A_1 &= A_3 = \frac{M}{2BC_1(C_2^2 - C_1^2)} = 98.196 \mu\text{m}^3 \\ A_2 &= A_4 = \frac{M}{2BC_2(C_2^2 - C_1^2)} = 69.232 \mu\text{m}^3 \end{aligned}$$

We can now calculate the integral term in equation (D.1) by using the residue theorem on the simple poles in the upper half of the complex plane<sup>1</sup>

$$\int_0^\infty r \frac{e^{-\alpha(r)\tau}}{\alpha(r)} dr = \int_0^\infty \frac{iA_1 r e^{-\alpha(r)\tau}}{(r - iC_1)} dr + \int_0^\infty \frac{iA_2 r e^{-\alpha(r)\tau}}{(r - iC_2)} dr \quad (\text{D.7})$$

<sup>1</sup>Check this in Churchill and Brown

For the first integral on the r.h.s. of equation (D.7) we calculate the residue by using the functional representation

$$\frac{p(r)}{q(r)} = \frac{iA_1 r e^{-\hat{\alpha}(r)\tau}}{(r - iC_1)} \quad (\text{D.8})$$

then  $p(r_0^{(1)}) = iA_1 r_0^{(1)} \neq 0$ ,  $q(r_0^{(1)}) = 0$  and  $q'(r_0^{(1)}) = 1 \neq 0$ , giving the residue

$$b_1 = \frac{p(r_0^{(1)})}{q'(r_0^{(1)})} = -A_1 C_1 \quad (\text{D.9})$$

and similarly we calculate the residue for the second integral as  $b_2 = -A_2 C_2$ . Then, using the Cauchy integral formula

$$f(z_0) = \frac{1}{2\pi i} \int \frac{f(z)}{z - z_0} dz \quad \Longrightarrow \quad \int \frac{f(z)}{z - z_0} dz = 2\pi i f(z_0)$$

to evaluate the integrals in equation (D.7) to give

$$\begin{aligned} \int_0^\infty r \frac{e^{-\hat{\alpha}(r)\tau}}{\hat{\alpha}(r)} dr &= -2\pi i (A_1 C_1 + A_2 C_2) \\ &= \frac{-2\pi i M}{B(C_2^2 - C_1^2)} \end{aligned} \quad (\text{D.10})$$

which can be used to give a solution for equation (D.1)

$$C_{12}(\tau) \sim \frac{-2\pi i M}{B(C_2^2 - C_1^2)} \quad (\text{D.11})$$

This does not represent a solution as it is purely imaginary and there is no  $\tau$  dependency. We suspect this is due to the simultaneous presence of the  $\nabla^4 z$  and  $\nabla^2 z$  terms in the Langevin equation.

## Appendix E

# Clipped Correlator For a Gaussian Stationary Process

This appendix shows the calculation of the “clipped” correlator for any Gaussian process, as shown in Majumdar, Sire, Bray and Cornell (1996). We start with the random Gaussian process  $z(\mathbf{x}, t)$  with the two-point time correlation function

$$c_{12}(t_1, t_2) = \langle z(\mathbf{x}, t_1)z(\mathbf{x}, t_2) \rangle \quad (\text{E.1})$$

and the autocorrelation function  $c_{11}(t) = \langle [z(\mathbf{x}, t)]^2 \rangle$ . If  $z(\mathbf{x}, t)$  is a Gaussian Stationary Process, then the process is time translation invariant and  $c_{11}(t) = c_{11}$  is constant for all  $t$ , and  $c_{12}(t_1, t_2) = c_{12}(\tau)$ , where  $\tau = |t_2 - t_1|$ .

Following the method set out by Majumdar, Sire, Bray and Cornell (1996), we introduce the normalised variable

$$X(t) = \frac{z(\mathbf{x}, t)}{\sqrt{\langle [z(\mathbf{x}, t)]^2 \rangle}} \quad (\text{E.2})$$

with the two-point time correlation function

$$C_{12}(t_1, t_2) = \langle X(t_1)X(t_2) \rangle = \left\langle \frac{z(\mathbf{x}, t_1)z(\mathbf{x}, t_2)}{\sqrt{\langle [z(\mathbf{x}, t_1)]^2 \rangle}\sqrt{\langle [z(\mathbf{x}, t_2)]^2 \rangle}} \right\rangle = \frac{c_{12}(\tau)}{c_{11}} = C_{12}(\tau) \quad (\text{E.3})$$

The covariance matrix is given by

$$\mathbf{C} = \begin{bmatrix} 1 & C_{12}(\tau) \\ C_{12}(\tau) & 1 \end{bmatrix} \quad (\text{E.4})$$

with inverse

$$\mathbf{C}^{-1} = \frac{1}{\det \mathbf{C}} \begin{bmatrix} 1 & -C_{12}(\tau) \\ -C_{12}(\tau) & 1 \end{bmatrix} \quad (\text{E.5})$$

where  $\det \mathbf{C} = 1 - [C_{12}(\tau)]^2$ .

For two variables  $X_1 = X(t_1)$  and  $X_2 = X(t_2)$ , the joint probability distribution has probability density function

$$P(X_1, X_2) = N e^{-\frac{1}{2} \mathbf{X}^T \mathbf{C}^{-1} \mathbf{X}} \quad (\text{E.6})$$

where  $\mathbf{X} = [X_1 \quad X_2]^T$  and  $N$  is the normalisation constant, ensuring

$$\int_{-\infty}^{\infty} dX_1 \int_{-\infty}^{\infty} dX_2 P(X_1, X_2) = 1 \quad (\text{E.7})$$

## E.1 Calculate Normalisation Constant

In order that

$$\int_{-\infty}^{\infty} dX_1 \int_{-\infty}^{\infty} dX_2 P(X_1, X_2) = 1 \quad (\text{E.8})$$

we require

$$1 = \int_{-\infty}^{\infty} dX_1 \int_{-\infty}^{\infty} dX_2 N e^{-\frac{1}{2} \mathbf{X}^T \mathbf{C}^{-1} \mathbf{X}} \quad (\text{E.9})$$

$$= N \int_{-\infty}^{\infty} dX_1 \int_{-\infty}^{\infty} dX_2 e^{-\frac{1}{2 \det \mathbf{C}} (X_1^2 + X_2^2 - 2C_{12}(\tau) X_1 X_2)} \quad (\text{E.10})$$

$$= N \int_{-\infty}^{\infty} dX_1 \int_{-\infty}^{\infty} dX_2 e^{-\frac{1}{2 \det \mathbf{C}} ((X_2 - C_{12}(\tau) X_1)^2 + (1 - [C_{12}(\tau)]^2) X_1^2)} \quad (\text{E.11})$$

$$= N \int_{-\infty}^{\infty} dX_1 e^{-\frac{1}{2} X_1^2} \int_{-\infty}^{\infty} dX_2 e^{-\frac{1}{2 \det \mathbf{C}} (X_2 - C_{12}(\tau) X_1)^2} \quad (\text{E.12})$$

Change of variables, let  $u = X_2 - C_{12}(\tau) X_1$ , then  $du = dX_2$ , and the limits remain unchanged ( $X_2 = -\infty, u = -\infty; X_2 = \infty, u = \infty$ ), giving

$$1 = N \int_{-\infty}^{\infty} dX_1 e^{-\frac{1}{2} X_1^2} \int_{-\infty}^{\infty} du e^{-\frac{1}{2 \det \mathbf{C}} u^2} \quad (\text{E.13})$$

$$= N \sqrt{2\pi \det \mathbf{C}} \int_{-\infty}^{\infty} dX_1 e^{-\frac{1}{2} X_1^2} \quad (\text{E.14})$$

$$= N \sqrt{2\pi \det \mathbf{C}} \sqrt{2\pi} \quad (\text{E.15})$$

then

$$N = \frac{1}{2\pi \sqrt{\det \mathbf{C}}} \quad (\text{E.16})$$

## E.2 Clipped Correlator

Introducing the ‘‘clipped’’ variable  $\sigma(X) = \text{sgn}(X)$ , we define the ‘‘clipped’’ correlator

$$A(t_1, t_2) = \langle \sigma(X_1)\sigma(X_2) \rangle \quad (\text{E.17})$$

$$= \int_{-\infty}^{\infty} dX_1 \int_{-\infty}^{\infty} dX_2 \sigma(X_1)\sigma(X_2) P(X_1, X_2) \quad (\text{E.18})$$

$$= \int_{-\infty}^0 dX_1 \int_{-\infty}^0 dX_2 P(X_1, X_2) - \int_{-\infty}^0 dX_1 \int_0^{\infty} dX_2 P(X_1, X_2) \\ - \int_0^{\infty} dX_1 \int_{-\infty}^0 dX_2 P(X_1, X_2) + \int_0^{\infty} dX_1 \int_0^{\infty} dX_2 P(X_1, X_2) \quad (\text{E.19})$$

$$= N \int_{-\infty}^0 dX_1 e^{-\frac{1}{2}X_1^2} \int_{-\infty}^0 dX_2 e^{-\frac{1}{2\det \mathbf{C}}(X_2 - C_{12}(\tau)X_1)^2} \\ - N \int_{-\infty}^0 dX_1 e^{-\frac{1}{2}X_1^2} \int_0^{\infty} dX_2 e^{-\frac{1}{2\det \mathbf{C}}(X_2 - C_{12}(\tau)X_1)^2} \\ - N \int_0^{\infty} dX_1 e^{-\frac{1}{2}X_1^2} \int_{-\infty}^0 dX_2 e^{-\frac{1}{2\det \mathbf{C}}(X_2 - C_{12}(\tau)X_1)^2} \\ + N \int_0^{\infty} dX_1 e^{-\frac{1}{2}X_1^2} \int_0^{\infty} dX_2 e^{-\frac{1}{2\det \mathbf{C}}(X_2 - C_{12}(\tau)X_1)^2} \quad (\text{E.20})$$

Change of variables, let  $u = X_2 - C_{12}(\tau)X_1$ , then  $du = dX_2$ , and the limits change to  $(X_2 = -\infty, u = -\infty; X_2 = \infty, u = \infty; X_2 = 0, u = -C_{12}(\tau)X_1)$ , giving

$$A(t_1, t_2) = N \int_{-\infty}^0 dX_1 e^{-\frac{1}{2}X_1^2} \int_{-\infty}^{-C_{12}(\tau)X_1} du e^{-\frac{1}{2\det \mathbf{C}}u^2} \\ - N \int_{-\infty}^0 dX_1 e^{-\frac{1}{2}X_1^2} \int_{-C_{12}(\tau)X_1}^{\infty} du e^{-\frac{1}{2\det \mathbf{C}}u^2} \\ - N \int_0^{\infty} dX_1 e^{-\frac{1}{2}X_1^2} \int_{-\infty}^{-C_{12}(\tau)X_1} du e^{-\frac{1}{2\det \mathbf{C}}u^2} \\ + N \int_0^{\infty} dX_1 e^{-\frac{1}{2}X_1^2} \int_{-C_{12}(\tau)X_1}^{\infty} du e^{-\frac{1}{2\det \mathbf{C}}u^2} \quad (\text{E.21})$$

$$A(t_1, t_2) = N \int_{-\infty}^0 dX_1 e^{-\frac{1}{2}X_1^2} \left[ \int_{-\infty}^0 du e^{-\frac{1}{2\det \mathbf{C}}u^2} + \int_0^{-C_{12}(\tau)X_1} du e^{-\frac{1}{2\det \mathbf{C}}u^2} \right] \\ - N \int_{-\infty}^0 dX_1 e^{-\frac{1}{2}X_1^2} \left[ \int_{-C_{12}(\tau)X_1}^0 du e^{-\frac{1}{2\det \mathbf{C}}u^2} + \int_0^{\infty} du e^{-\frac{1}{2\det \mathbf{C}}u^2} \right] \\ - N \int_0^{\infty} dX_1 e^{-\frac{1}{2}X_1^2} \left[ \int_{-\infty}^0 du e^{-\frac{1}{2\det \mathbf{C}}u^2} + \int_0^{-C_{12}(\tau)X_1} du e^{-\frac{1}{2\det \mathbf{C}}u^2} \right] \\ + N \int_0^{\infty} dX_1 e^{-\frac{1}{2}X_1^2} \left[ \int_{-C_{12}(\tau)X_1}^0 du e^{-\frac{1}{2\det \mathbf{C}}u^2} + \int_0^{\infty} du e^{-\frac{1}{2\det \mathbf{C}}u^2} \right] \quad (\text{E.22})$$

$$\begin{aligned}
A(t_1, t_2) &= \frac{1}{2\sqrt{2\pi}} \int_{-\infty}^0 dX_1 e^{-\frac{1}{2}X_1^2} + N \int_{-\infty}^0 dX_1 e^{-\frac{1}{2}X_1^2} \int_0^{-C_{12}(\tau)X_1} du e^{-\frac{1}{2\det \mathbf{C}}u^2} \\
&\quad - N \int_{-\infty}^0 dX_1 e^{-\frac{1}{2}X_1^2} \int_{-C_{12}(\tau)X_1}^0 du e^{-\frac{1}{2\det \mathbf{C}}u^2} - \frac{1}{2\sqrt{2\pi}} \int_{-\infty}^0 dX_1 e^{-\frac{1}{2}X_1^2} \\
&\quad - \frac{1}{2\sqrt{2\pi}} \int_{-\infty}^0 dX_1 e^{-\frac{1}{2}X_1^2} - N \int_0^{\infty} dX_1 e^{-\frac{1}{2}X_1^2} \int_0^{-C_{12}(\tau)X_1} du e^{-\frac{1}{2\det \mathbf{C}}u^2} \\
&\quad + N \int_0^{\infty} dX_1 e^{-\frac{1}{2}X_1^2} \int_{-C_{12}(\tau)X_1}^0 du e^{-\frac{1}{2\det \mathbf{C}}u^2} + \frac{1}{2\sqrt{2\pi}} \int_0^{\infty} dX_1 e^{-\frac{1}{2}X_1^2} \quad (\text{E.23})
\end{aligned}$$

$$\begin{aligned}
A(t_1, t_2) &= N \int_{-\infty}^0 dX_1 e^{-\frac{1}{2}X_1^2} \int_0^{-C_{12}(\tau)X_1} du e^{-\frac{1}{2\det \mathbf{C}}u^2} \\
&\quad - N \int_{-\infty}^0 dX_1 e^{-\frac{1}{2}X_1^2} \int_{-C_{12}(\tau)X_1}^0 du e^{-\frac{1}{2\det \mathbf{C}}u^2} \\
&\quad - N \int_0^{\infty} dX_1 e^{-\frac{1}{2}X_1^2} \int_0^{-C_{12}(\tau)X_1} du e^{-\frac{1}{2\det \mathbf{C}}u^2} \\
&\quad + N \int_0^{\infty} dX_1 e^{-\frac{1}{2}X_1^2} \int_{-C_{12}(\tau)X_1}^0 du e^{-\frac{1}{2\det \mathbf{C}}u^2} \quad (\text{E.24})
\end{aligned}$$

$$\begin{aligned}
A(t_1, t_2) &= 4N\sqrt{\det \mathbf{C}} \tan^{-1} \left( \frac{C_{12}(\tau)}{\det \mathbf{C}} \right) \\
&= \frac{2}{\pi} \tan^{-1} \left( \frac{C_{12}(\tau)}{\det \mathbf{C}} \right) \\
&= \frac{2}{\pi} \sin^{-1} (C_{12}(\tau)) \quad (\text{E.25})
\end{aligned}$$

## Appendix F

# Clipped Correlator Derivation

This chapter shows the derivation of the “clipped” correlator used to define the bonding events that persist at a distance  $\Delta$  from the mean separation distance for the Langevin equation (2.12). We start with the random Gaussian process  $z(\mathbf{x}, t)$  with the two-point time correlation function

$$c_{12}(t_1, t_2) = \langle z(\mathbf{x}, t_1)z(\mathbf{x}, t_2) \rangle \quad (\text{F.1})$$

and the autocorrelation function  $c_{11}(t) = \langle [z(\mathbf{x}, t)]^2 \rangle$ . If  $z(\mathbf{x}, t)$  is a Gaussian Stationary Process, then the process is time translation invariant and  $c_{11}(t) = c_{11}$  is constant for all  $t$ , and  $c_{12}(t_1, t_2) = c_{12}(\tau)$ , where  $\tau = |t_2 - t_1|$ .

Following the method set out by Majumdar, Sire, Bray and Cornell (1996), we introduce the normalised variable

$$X(t) = \frac{z(\mathbf{x}, t)}{\sqrt{\langle [z(\mathbf{x}, t)]^2 \rangle}} \quad (\text{F.2})$$

with the two-point time correlation function

$$C_{12}(t_1, t_2) = \langle X(t_1)X(t_2) \rangle = \left\langle \frac{z(\mathbf{x}, t_1)z(\mathbf{x}, t_2)}{\sqrt{\langle [z(\mathbf{x}, t_1)]^2 \rangle}\sqrt{\langle [z(\mathbf{x}, t_2)]^2 \rangle}} \right\rangle = \frac{c_{12}(\tau)}{c_{11}} = C_{12}(\tau) \quad (\text{F.3})$$

The covariance matrix is given by

$$\mathbf{C} = \begin{bmatrix} 1 & C_{12}(\tau) \\ C_{12}(\tau) & 1 \end{bmatrix} \quad (\text{F.4})$$

with inverse

$$\mathbf{C}^{-1} = \frac{1}{\det \mathbf{C}} \begin{bmatrix} 1 & -C_{12}(\tau) \\ -C_{12}(\tau) & 1 \end{bmatrix} \quad (\text{F.5})$$

where  $\det \mathbf{C} = 1 - [C_{12}(\tau)]^2$ .

For two variables  $X_1 = X(t_1)$  and  $X_2 = X(t_2)$ , the joint probability distribution has probability density function

$$P(X_1, X_2) = N e^{-\frac{1}{2} \mathbf{X}^T \mathbf{C}^{-1} \mathbf{X}} \quad (\text{F.6})$$

where  $\mathbf{X} = [X_1 \ X_2]^T$  and  $N$  is the normalisation constant, ensuring

$$\int_{-\infty}^{\infty} dX_1 \int_{-\infty}^{\infty} dX_2 P(X_1, X_2) = 1 \quad (\text{F.7})$$

## F.1 Calculate Normalisation Constant

In order that

$$\int_{-\infty}^{\infty} dX_1 \int_{-\infty}^{\infty} dX_2 P(X_1, X_2) = 1 \quad (\text{F.8})$$

we require

$$1 = \int_{-\infty}^{\infty} dX_1 \int_{-\infty}^{\infty} dX_2 N e^{-\frac{1}{2} \mathbf{X}^T \mathbf{C}^{-1} \mathbf{X}} \quad (\text{F.9})$$

$$= N \int_{-\infty}^{\infty} dX_1 \int_{-\infty}^{\infty} dX_2 e^{-\frac{1}{2 \det \mathbf{C}} (X_1^2 + X_2^2 - 2C_{12}(\tau) X_1 X_2)} \quad (\text{F.10})$$

$$= N \int_{-\infty}^{\infty} dX_1 \int_{-\infty}^{\infty} dX_2 e^{-\frac{1}{2 \det \mathbf{C}} ((X_2 - C_{12}(\tau) X_1)^2 + (1 - [C_{12}(\tau)]^2) X_1^2)} \quad (\text{F.11})$$

$$= N \int_{-\infty}^{\infty} dX_1 e^{-\frac{1}{2} X_1^2} \int_{-\infty}^{\infty} dX_2 e^{-\frac{1}{2 \det \mathbf{C}} (X_2 - C_{12}(\tau) X_1)^2} \quad (\text{F.12})$$

Change of variables, let  $u = X_2 - C_{12}(\tau) X_1$ , then  $du = dX_2$ , and the limits remain unchanged ( $X_2 = -\infty, u = -\infty; X_2 = \infty, u = \infty$ ), giving

$$1 = N \int_{-\infty}^{\infty} dX_1 e^{-\frac{1}{2} X_1^2} \int_{-\infty}^{\infty} du e^{-\frac{1}{2 \det \mathbf{C}} u^2} \quad (\text{F.13})$$

$$= N \sqrt{2\pi \det \mathbf{C}} \int_{-\infty}^{\infty} dX_1 e^{-\frac{1}{2} X_1^2} \quad (\text{F.14})$$

$$= N \sqrt{2\pi \det \mathbf{C}} \sqrt{2\pi} \quad (\text{F.15})$$

then

$$N = \frac{1}{2\pi \sqrt{\det \mathbf{C}}} \quad (\text{F.16})$$

## F.2 Clipped Correlator

We begin defining the ‘‘clipped’’ variable that is 1 for close contact patches and 0 otherwise. Now, the condition  $z(\mathbf{x}, t) \geq \Delta$  translates as  $X(t) \geq \frac{\Delta}{\sqrt{c_{11}}}$  for our normalised variable, so we

introduce the ‘‘clipped’’ variable

$$\sigma(X) = \begin{cases} 1 & \text{for } X \geq \frac{\Delta}{\sqrt{c_{11}}} \\ 0 & \text{for } X < \frac{\Delta}{\sqrt{c_{11}}} \end{cases} \quad (\text{F.17})$$

Then the ‘‘clipped’’ correlator is given as

$$\begin{aligned} A(t_1, t_2) &= \langle \sigma(X_1)\sigma(X_2) \rangle \\ &= \int_{-\infty}^{\infty} dX_1 \int_{-\infty}^{\infty} dX_2 \sigma(X_1)\sigma(X_2)P(X_1, X_2) \\ &= N \int_{\frac{\Delta}{\sqrt{c_{11}}} }^{\infty} dX_1 \int_{\frac{\Delta}{\sqrt{c_{11}}} }^{\infty} dX_2 e^{-\frac{1}{2\det \mathbf{C}}(X_1^2 + X_2^2 - 2C_{12}(\tau)X_1X_2)} \\ &= N \int_{\frac{\Delta}{\sqrt{c_{11}}} }^{\infty} dX_1 e^{-\frac{1}{2}X_1^2} \int_{\frac{\Delta}{\sqrt{c_{11}}} }^{\infty} dX_2 e^{-\frac{1}{2\det \mathbf{C}}(X_2 - C_{12}(\tau)X_1)^2} \end{aligned}$$

Change of variables, let  $u = X_2 - C_{12}(\tau)X_1$ , then  $du = dX_2$ , and the limits are changed ( $X_2 = \frac{\Delta}{\sqrt{c_{11}}}$ ,  $u = \frac{\Delta}{\sqrt{c_{11}}} - C_{12}(\tau)X_1$ ;  $X_2 = \infty$ ,  $u = \infty$ ), giving

$$A(t_1, t_2) = N \int_{\frac{\Delta}{\sqrt{c_{11}}} }^{\infty} dX_1 e^{-\frac{1}{2}X_1^2} \int_{\frac{\Delta}{\sqrt{c_{11}}} - C_{12}(\tau)X_1}^{\infty} du e^{-\frac{1}{2\det \mathbf{C}}u^2} \quad (\text{F.18})$$

### F.2.1 $\frac{\partial A(\tau)}{\partial \tau}$ Calculation

Here we present the calculation steps to determine an expression for  $\frac{\partial A(\tau)}{\partial \tau}$ , where  $A(\tau)$  is given by equation F.18. The  $\tau$  dependency is realised through  $C_{12}(\tau)$ , therefore we can calculate the derivative using the chain rule

$$\frac{\partial A(\tau)}{\partial \tau} = \frac{\partial A(\tau)}{\partial C_{12}(\tau)} \frac{\partial C_{12}(\tau)}{\partial \tau} \quad (\text{F.19})$$

### $\frac{\partial A(\tau)}{\partial C_{12}(\tau)}$ Calculation

We wish to calculate

$$\begin{aligned} \frac{\partial A(\tau)}{\partial C_{12}(\tau)} &= \frac{\partial}{\partial C_{12}(\tau)} \left\{ N \int_{\frac{\Delta}{\sqrt{c_{11}}} }^{\infty} dX_1 e^{-\frac{1}{2}X_1^2} \int_{\frac{\Delta}{\sqrt{c_{11}}} - C_{12}(\tau)X_1}^{\infty} du e^{-\frac{1}{2\det \mathbf{C}}u^2} \right\} \\ &= \frac{\partial}{\partial C_{12}(\tau)} \{N\} \int_{\frac{\Delta}{\sqrt{c_{11}}} }^{\infty} dX_1 e^{-\frac{1}{2}X_1^2} \int_{\frac{\Delta}{\sqrt{c_{11}}} - C_{12}(\tau)X_1}^{\infty} du e^{-\frac{1}{2\det \mathbf{C}}u^2} \\ &\quad + N \frac{\partial}{\partial C_{12}(\tau)} \left\{ \int_{\frac{\Delta}{\sqrt{c_{11}}} }^{\infty} dX_1 e^{-\frac{1}{2}X_1^2} \int_{\frac{\Delta}{\sqrt{c_{11}}} - C_{12}(\tau)X_1}^{\infty} du e^{-\frac{1}{2\det \mathbf{C}}u^2} \right\} \end{aligned} \quad (\text{F.20})$$

Now,

$$\begin{aligned}
\frac{\partial}{\partial C_{12}(\tau)} \{N\} &= \frac{\partial}{\partial C_{12}(\tau)} \left\{ \frac{1}{2\pi\sqrt{\det \mathbf{C}}} \right\} \\
&= \frac{\partial}{\partial C_{12}(\tau)} \left\{ \frac{1}{2\pi\sqrt{1 - [C_{12}(\tau)]^2}} \right\} \\
&= \frac{1}{2\pi} \frac{\partial}{\partial C_{12}(\tau)} \left\{ (1 - [C_{12}(\tau)]^2)^{-\frac{1}{2}} \right\} \\
&= \frac{1}{2\pi} \times -\frac{1}{2} (1 - [C_{12}(\tau)]^2)^{-\frac{3}{2}} \times -2C_{12}(\tau) \\
&= \frac{C_{12}(\tau)}{2\pi (\det \mathbf{C})^{\frac{3}{2}}}
\end{aligned} \tag{F.21}$$

and to solve the second partial derivative in equation (F.25) we first move the derivative under the first integral sign, since there is no  $C_{12}(\tau)$  dependency, to give

$$\begin{aligned}
\frac{\partial}{\partial C_{12}(\tau)} \left\{ \int_{\frac{\Delta}{\sqrt{e_{11}}}}^{\infty} dX_1 e^{-\frac{1}{2}X_1^2} \int_{\frac{\Delta}{\sqrt{e_{11}} - C_{12}(\tau)X_1}}^{\infty} du e^{-\frac{1}{2\det \mathbf{C}}u^2} \right\} \\
= \int_{\frac{\Delta}{\sqrt{e_{11}}}}^{\infty} dX_1 e^{-\frac{1}{2}X_1^2} \frac{\partial}{\partial C_{12}(\tau)} \left\{ \int_{\frac{\Delta}{\sqrt{e_{11}} - C_{12}(\tau)X_1}}^{\infty} du e^{-\frac{1}{2\det \mathbf{C}}u^2} \right\}
\end{aligned} \tag{F.22}$$

then applying the Leibnitz differentiation rule

$$\begin{aligned}
\frac{\partial}{\partial C_{12}} \left\{ \int_{a(C_{12})}^{b(C_{12})} f(X_1, C_{12}) dX_1 \right\} &= \int_{a(C_{12})}^{b(C_{12})} \frac{\partial}{\partial C_{12}} \{f(X_1, C_{12})\} dX_1 \\
&+ f(b(C_{12}), C_{12}) \frac{\partial}{\partial C_{12}} \{b(C_{12})\} \\
&- f(a(C_{12}), C_{12}) \frac{\partial}{\partial C_{12}} \{a(C_{12})\}
\end{aligned} \tag{F.23}$$

we get

$$\begin{aligned}
\frac{\partial}{\partial C_{12}(\tau)} \left\{ \int_{\frac{\Delta}{\sqrt{e_{11}} - C_{12}(\tau)X_1}}^{\infty} du e^{-\frac{1}{2\det \mathbf{C}}u^2} \right\} \\
= X_1 e^{-\frac{C_{12}(\tau)}{2\det \mathbf{C}} \left( X_1 - \frac{\Delta}{C_{12}(\tau)\sqrt{e_{11}}} \right)^2} - \int_{\frac{\Delta}{\sqrt{e_{11}} - C_{12}(\tau)X_1}}^{\infty} du \frac{u^2 C_{12}(\tau)}{(\det \mathbf{C})^2} e^{-\frac{1}{2\det \mathbf{C}}u^2}
\end{aligned} \tag{F.24}$$

Then, using equations (F.21) and (F.24) we can write the full form for equation (F.25) as

$$\begin{aligned}
\frac{\partial A(\tau)}{\partial C_{12}(\tau)} &= \frac{C_{12}(\tau)}{2\pi (\det \mathbf{C})^{\frac{3}{2}}} \int_{\frac{\Delta}{\sqrt{e_{11}}} - C_{12}(\tau)X_1}^{\infty} dX_1 e^{-\frac{1}{2}X_1^2} \int_{\frac{\Delta}{\sqrt{e_{11}} - C_{12}(\tau)X_1}}^{\infty} du e^{-\frac{1}{2\det \mathbf{C}}u^2} \\
&+ N \int_{\frac{\Delta}{\sqrt{e_{11}}} - C_{12}(\tau)X_1}^{\infty} dX_1 e^{-\frac{1}{2}X_1^2} X_1 e^{-\frac{C_{12}(\tau)}{2\det \mathbf{C}} \left( X_1 - \frac{\Delta}{C_{12}(\tau)\sqrt{e_{11}}} \right)^2} \\
&- N \int_{\frac{\Delta}{\sqrt{e_{11}}} - C_{12}(\tau)X_1}^{\infty} dX_1 e^{-\frac{1}{2}X_1^2} \int_{\frac{\Delta}{\sqrt{e_{11}} - C_{12}(\tau)X_1}}^{\infty} du \frac{u^2 C_{12}(\tau)}{(\det \mathbf{C})^2} e^{-\frac{1}{2\det \mathbf{C}}u^2}
\end{aligned} \tag{F.25}$$

$\frac{\partial c_{12}(\tau)}{\partial \tau}$  **Calculation**

The approximation for the two-point time correlation function, in the large time limit, for  $z(\mathbf{x}, t)$  is given by

$$c_{12}(\tau) = \frac{D}{2\pi M^2} \int_0^\infty \frac{r}{\alpha(r)} e^{-\alpha(r)\tau} \quad (\text{F.26})$$

where  $\alpha(r) = \frac{Br^4 + \gamma r^2 + \lambda}{M}$ . Then, the first derivative of  $C_{12}(\tau)$ , equation (F.3), with respect to  $\tau$  is given by

$$\frac{\partial C_{12}(\tau)}{\partial \tau} = \frac{\partial}{\partial \tau} \left\{ \frac{D}{2\pi c_{11} M^2} \int_0^\infty r \frac{e^{-\alpha(r)\tau}}{\alpha(r)} dr \right\} = \frac{-D}{2\pi c_{11} M^2} \int_0^\infty r e^{-\alpha(r)\tau} dr \quad (\text{F.27})$$

$\frac{\partial A(\tau)}{\partial \tau}$  **Calculation**

Using equations (F.25) and (F.27) we can rearrange to get the full form for the derivative of  $A(\tau)$  with respect to  $\tau$

$$\begin{aligned} \frac{\partial A(\tau)}{\partial \tau} = & \left[ \frac{C_{12}(\tau)}{2\pi (\det \mathbf{C})^{\frac{3}{2}}} \int_{\frac{\Delta}{\sqrt{e_{11}}}}^\infty dX_1 e^{-\frac{1}{2}X_1^2} \int_{\frac{\Delta}{\sqrt{e_{11}}} - C_{12}(\tau)X_1}^\infty du e^{-\frac{1}{2\det \mathbf{C}}u^2} \right. \\ & + \frac{1}{2\pi \sqrt{\det \mathbf{C}}} \int_{\frac{\Delta}{\sqrt{e_{11}}} }^\infty dX_1 e^{-\frac{1}{2}X_1^2} X_1 e^{-\frac{C_{12}(\tau)}{2\det \mathbf{C}} \left( X_1 - \frac{\Delta}{C_{12}(\tau)\sqrt{e_{11}}} \right)^2} \\ & \left. - \frac{C_{12}(\tau)}{2\pi (\det \mathbf{C})^{\frac{5}{2}}} \int_{\frac{\Delta}{\sqrt{e_{11}}} }^\infty dX_1 e^{-\frac{1}{2}X_1^2} \int_{\frac{\Delta}{\sqrt{e_{11}}} - C_{12}(\tau)X_1}^\infty du u^2 e^{-\frac{1}{2\det \mathbf{C}}u^2} \right] \\ & \times \frac{-D}{2\pi c_{11} M^2} \int_0^\infty r e^{-\alpha(r)\tau} dr \quad (\text{F.28}) \end{aligned}$$

## Appendix G

# Steady State Fokker-Planck Equation

In this appendix, the steady state Fokker-Planck equation is used to derive an expression for the probability density distribution for the local intermembrane separation distance. Section G.1 shows steps required to express the Langevin equation as a Fokker-Planck equation, that describes the time evolution of the probability density distribution. The steady state, equilibrium, probability density distribution is then calculated for the Fourier transformed variable, of the intermembrane separation distance. Then, in section G.2, the conversion from the Fourier space to the cartesian space is shown.

### G.1 Langevin Equation to Steady State Fokker-Planck Equation

In this section, we use the Fokker-Planck equation to study the steady state probability density distribution for the local mean separation distance, where it can be shown the steady state probability density distribution admits of a Gaussian form. We begin with the Langevin equation in the Fourier  $k - t$  space, equation (3.4), that may be expressed in the form

$$\frac{\partial \tilde{z}(\mathbf{k}, t)}{\partial t} = f(\tilde{z}(\mathbf{k}, t), t) + g(\tilde{z}(\mathbf{k}, t), t)\zeta(\mathbf{k}, t) \quad (\text{G.1})$$

where  $\zeta$  has zero mean and unit variance. The linear IS model is mapped to equation (G.1) through the functions

$$f(\tilde{z}(\mathbf{k}, t), t) = -\alpha(\mathbf{k})\tilde{z}(\mathbf{k}, t) \quad (\text{G.2})$$

$$g(\tilde{z}(\mathbf{k}, t), t) = \frac{\sqrt{2D}}{M} \quad (\text{G.3})$$

where we have a constant function  $g(\tilde{z}(\mathbf{k}, t), t)$  that is independent of time and the separation distance, that we will call  $g$ . In the form presented in equation (G.1), it can be shown that the Langevin equation is equivalent to the forward Fokker-Planck equation for the probability distribution  $P(\tilde{z}_k, k, t)$ , that is the probability the system is at the separation distance in the  $k - t$  space,  $\tilde{z}_k$ , at time  $t$  (Risken, 1989). Using the probability density definition

$$P(\tilde{z}_k, \mathbf{k}, t) = \langle \delta(\tilde{z}_k - \tilde{z}(\mathbf{k}, t)) \rangle \quad (\text{G.4})$$

resulting in the Fokker-Planck equation

$$\frac{\partial}{\partial t} P(\tilde{z}_k, \mathbf{k}, t) = -\frac{\partial}{\partial \tilde{z}_k} [f(\tilde{z}_k) P(\tilde{z}_k, \mathbf{k}, t)] + \frac{\partial^2}{\partial \tilde{z}_k^2} \left[ \frac{g^2}{2} P(\tilde{z}_k, \mathbf{k}, t) \right] \quad (\text{G.5})$$

The steady state solution occurs when  $\frac{\partial P(\tilde{z}_k, \mathbf{k}, t)}{\partial t} = 0$  and we call the steady state probability distribution  $P_s(\tilde{z}_k, \mathbf{k})$ , then

$$\frac{\partial}{\partial \tilde{z}_k} \left[ -f(\tilde{z}_k) P_s(\tilde{z}_k, \mathbf{k}) + \frac{g^2}{2} \frac{\partial}{\partial \tilde{z}_k} P_s(\tilde{z}_k, \mathbf{k}) \right] = 0 \quad (\text{G.6})$$

A solution exists when the term inside brackets is constant, that we can set to 0 without loss of generality, then

$$\frac{g^2}{2} \frac{\partial}{\partial \tilde{z}_k} P_s(\tilde{z}_k, \mathbf{k}) - f(\tilde{z}_k) P_s(\tilde{z}_k, \mathbf{k}) = 0 \quad (\text{G.7})$$

that for our case is

$$\frac{\partial}{\partial \tilde{z}_k} P_s(\tilde{z}_k, \mathbf{k}) + \frac{M^2 \alpha(\mathbf{k})}{D} \tilde{z}_k P_s(\tilde{z}_k, \mathbf{k}) = 0 \quad (\text{G.8})$$

Using the integrating factor method, we can solve equation (G.8)

$$P_s(\tilde{z}_k, \mathbf{k}) = C e^{-\frac{M^2 \alpha(\mathbf{k})}{D} \tilde{z}_k^2} \quad (\text{G.9})$$

where  $P_s$  is a function of  $\mathbf{k}$  and  $\tilde{z}_k$ , and  $C$  is the normalisation factor

$$C = \left( \frac{M^2 \alpha(\mathbf{k})}{\pi D} \right)^{\frac{1}{2}} \quad (\text{G.10})$$

## G.2 Relation to $P(z(\mathbf{x}, t), \mathbf{x}, t)$

Consider

$$P(Z, \mathbf{x}, t) = \langle \delta(Z - z(\mathbf{x}, t)) \rangle \quad (\text{G.11})$$

$$= \int dq \langle e^{iq(Z - z(\mathbf{x}, t))} \rangle \quad (\text{G.12})$$

$$= \int dq e^{iqZ} \langle e^{-\frac{iq}{2\pi} \sum_{\mathbf{k}} \tilde{z}(\mathbf{k}, t) e^{i\mathbf{k} \cdot \mathbf{x}}} \rangle \quad (\text{G.13})$$

$$= \int dq e^{iqZ} \prod_{\mathbf{k}} \langle e^{-\frac{iq}{2\pi} \tilde{z}(\mathbf{k}, t) e^{i\mathbf{k} \cdot \mathbf{x}}} \rangle \quad (\text{G.14})$$

then we use equation (G.9) to find an expression for the statistical ensemble

$$\langle e^{-\frac{iq}{2\pi} \tilde{z}(\mathbf{k}, t) e^{i\mathbf{k} \cdot \mathbf{x}}} \rangle = C \int d\tilde{z}_{\mathbf{k}} e^{-\frac{iq}{2\pi} \tilde{z}_{\mathbf{k}} e^{i\mathbf{k} \cdot \mathbf{x}}} e^{-\frac{M^2 \alpha(\mathbf{k})}{D} \tilde{z}_{\mathbf{k}}^2} \quad (\text{G.15})$$

$$= C \int d\tilde{z}_{\mathbf{k}} e^{-\left[ \frac{iq}{2\pi} \tilde{z}_{\mathbf{k}} e^{i\mathbf{k} \cdot \mathbf{x}} + \frac{M^2 \alpha(\mathbf{k})}{D} \tilde{z}_{\mathbf{k}}^2 \right]} \quad (\text{G.16})$$

$$= C \int d\tilde{z}_{\mathbf{k}} e^{-\frac{M^2 \alpha(\mathbf{k})}{D} \left[ \frac{iqD}{2\pi M^2 \alpha(\mathbf{k})} \tilde{z}_{\mathbf{k}} e^{i\mathbf{k} \cdot \mathbf{x}} + \tilde{z}_{\mathbf{k}}^2 \right]} \quad (\text{G.17})$$

$$= C \int d\tilde{z}_{\mathbf{k}} e^{-\frac{M^2 \alpha(\mathbf{k})}{D} \left[ \left( \tilde{z}_{\mathbf{k}} + \frac{iqD}{4\pi M^2 \alpha(\mathbf{k})} e^{i\mathbf{k} \cdot \mathbf{x}} \right)^2 - \left( \frac{iqD}{4\pi M^2 \alpha(\mathbf{k})} \right)^2 e^{2i\mathbf{k} \cdot \mathbf{x}} \right]} \quad (\text{G.18})$$

$$= C e^{-\frac{q^2}{(4\pi)^2} \frac{D}{M^2 \alpha(\mathbf{k})} e^{2i\mathbf{k} \cdot \mathbf{x}}} \int d\tilde{z}_{\mathbf{k}} e^{-\frac{M^2 \alpha(\mathbf{k})}{D} \left[ \left( \tilde{z}_{\mathbf{k}} + \frac{iqD}{4\pi M^2 \alpha(\mathbf{k})} e^{i\mathbf{k} \cdot \mathbf{x}} \right)^2 \right]} \quad (\text{G.19})$$

$$= C \left( \frac{\pi D}{M^2 \alpha(\mathbf{k})} \right)^{\frac{1}{2}} e^{-\frac{q^2}{(4\pi)^2} \frac{D}{M^2 \alpha(\mathbf{k})} e^{2i\mathbf{k} \cdot \mathbf{x}}} \quad (\text{G.20})$$

then using equation (??) we get the final expression

$$\langle e^{-\frac{iq}{2\pi} \tilde{z}(\mathbf{k}, t) e^{i\mathbf{k} \cdot \mathbf{x}}} \rangle = e^{-\frac{q^2}{(4\pi)^2} \frac{D}{M^2 \alpha(\mathbf{k})} e^{2i\mathbf{k} \cdot \mathbf{x}}} \quad (\text{G.21})$$

that we substitute in to equation (??) to give

$$P(Z, \mathbf{x}, t) = \int dq e^{iqZ} \prod_{\mathbf{k}} e^{-\frac{q^2}{(4\pi)^2} \frac{D}{M^2 \alpha(\mathbf{k})} e^{2i\mathbf{k} \cdot \mathbf{x}}} \quad (\text{G.22})$$

$$(\text{G.23})$$

Let  $A(\mathbf{k}, \mathbf{x}) = \frac{D}{2\pi^2 M^2 \alpha(\mathbf{k})} e^{2i\mathbf{k}\cdot\mathbf{x}}$ , then

$$P(Z, \mathbf{x}, t) = \int dq e^{iqZ} \prod_{\mathbf{k}} e^{-\frac{A(\mathbf{k}, \mathbf{x})}{2} q^2} \quad (\text{G.24})$$

$$= \int dq e^{iqZ} e^{-\frac{\sum_{\mathbf{k}} A(\mathbf{k}, \mathbf{x})}{2} q^2} \quad (\text{G.25})$$

$$= \int dq e^{-\frac{\sum_{\mathbf{k}} A(\mathbf{k}, \mathbf{x})}{2} \left( q^2 - \frac{2iqZ}{\sum_{\mathbf{k}} A(\mathbf{k}, \mathbf{x})} \right)} \quad (\text{G.26})$$

$$= \int dq e^{-\frac{\sum_{\mathbf{k}} A(\mathbf{k}, \mathbf{x})}{2} \left[ \left( q - \frac{iZ}{\sum_{\mathbf{k}} A(\mathbf{k}, \mathbf{x})} \right)^2 + \left( \frac{Z}{\sum_{\mathbf{k}} A(\mathbf{k}, \mathbf{x})} \right)^2 \right]} \quad (\text{G.27})$$

$$= e^{-\frac{Z^2}{2\sum_{\mathbf{k}} A(\mathbf{k}, \mathbf{x})}} \int dq e^{-\frac{\sum_{\mathbf{k}} A(\mathbf{k}, \mathbf{x})}{2} \left( q - \frac{iZ}{\sum_{\mathbf{k}} A(\mathbf{k}, \mathbf{x})} \right)^2} \quad (\text{G.28})$$

then, using substitution of variables

$$P(Z, \mathbf{x}, t) = e^{-\frac{Z^2}{2\sum_{\mathbf{k}} A(\mathbf{k}, \mathbf{x})}} \int du e^{-\frac{\sum_{\mathbf{k}} A(\mathbf{k}, \mathbf{x})}{2} u^2} \quad (\text{G.29})$$

$$= \left( \frac{2\pi}{\sum_{\mathbf{k}} A(\mathbf{k}, \mathbf{x})} \right)^{\frac{1}{2}} e^{-\frac{Z^2}{2\sum_{\mathbf{k}} A(\mathbf{k}, \mathbf{x})}} \quad (\text{G.30})$$

where

$$\sum_{\mathbf{k}} A(\mathbf{k}, \mathbf{x}) = \frac{D}{2\pi^2 M^2} \int d\mathbf{k} \frac{e^{2i\mathbf{k}\cdot\mathbf{x}}}{\alpha(\mathbf{k})} \quad (\text{G.31})$$

In order for  $P(Z, \mathbf{x}, t)$  to be a Gaussian,  $\sum_{\mathbf{k}} A(\mathbf{k}, \mathbf{x})$  must be positive definite. This is true, if

$$\frac{D}{2\pi^2 M^2} \int d\mathbf{k} \frac{e^{2i\mathbf{k}\cdot\mathbf{x}}}{\alpha(\mathbf{k})} > 0 \quad (\text{G.32})$$

Now,  $D, M > 0$ ,  $\alpha(\mathbf{k}) > 0$  for all  $\mathbf{k}$ , and

$$\int d\mathbf{k} e^{2i\mathbf{k}\cdot\mathbf{x}} = \int d\mathbf{k} \left( e^{i\mathbf{k}\cdot\mathbf{x}} \right)^2 \quad (\text{G.33})$$

$$= \int d\mathbf{k} \left( \cos(\mathbf{k}\cdot\mathbf{x}) + i \sin(\mathbf{k}\cdot\mathbf{x}) \right)^2 \quad (\text{G.34})$$

$$= \int d\mathbf{k} \cos^2(\mathbf{k}\cdot\mathbf{x}) - \sin^2(\mathbf{k}\cdot\mathbf{x}) + 2i \cos(\mathbf{k}\cdot\mathbf{x}) \sin(\mathbf{k}\cdot\mathbf{x}) \quad (\text{G.35})$$

and

$$\int d\mathbf{k} 2i \cos(\mathbf{k}\cdot\mathbf{x}) \sin(\mathbf{k}\cdot\mathbf{x}) = 0 \quad (\text{G.36})$$

therefore, we require

$$\int d\mathbf{k} \cos^2(\mathbf{k}\cdot\mathbf{x}) - \sin^2(\mathbf{k}\cdot\mathbf{x}) \geq 0 \quad (\text{G.37})$$

$$\int d\mathbf{k} \frac{1}{2} (1 + \cos(2\mathbf{k}\cdot\mathbf{x})) - \frac{1}{2} (1 - \cos(2\mathbf{k}\cdot\mathbf{x})) \geq 0 \quad (\text{G.38})$$

$$\int d\mathbf{k} \cos(2\mathbf{k}\cdot\mathbf{x}) \geq 0 \quad (\text{G.39})$$

$$(\text{G.40})$$

and this equality holds when

$$-\frac{\pi}{2} < 2\mathbf{k} \cdot \mathbf{x} < \frac{\pi}{2} \quad (\text{G.41})$$

$$-\frac{\pi}{4} < \mathbf{k} \cdot \mathbf{x} < \frac{\pi}{4} \quad (\text{G.42})$$

$$(\text{G.43})$$

therefore,  $\sum_{\mathbf{k}} A(\mathbf{k}, \mathbf{x}) \geq 0$  and  $P(Z, \mathbf{x}, t)$  is Gaussian distributed.

To normalise the probability over  $-\infty < Z < \infty$ ,

$$1 = \int_{-\infty}^{\infty} N P(Z, \mathbf{x}, t) dZ \quad (\text{G.44})$$

$$= N \int_{-\infty}^{\infty} \left( \frac{2\pi}{\sum_{\mathbf{k}} A(\mathbf{k}, \mathbf{x})} \right)^{\frac{1}{2}} e^{-\frac{Z^2}{2\sum_{\mathbf{k}} A(\mathbf{k}, \mathbf{x})}} dZ \quad (\text{G.45})$$

$$= N \left( \frac{2\pi}{\sum_{\mathbf{k}} A(\mathbf{k}, \mathbf{x})} \right)^{\frac{1}{2}} \int_{-\infty}^{\infty} e^{-\frac{Z^2}{2\sum_{\mathbf{k}} A(\mathbf{k}, \mathbf{x})}} dZ \quad (\text{G.46})$$

$$= N \left( \frac{2\pi}{\sum_{\mathbf{k}} A(\mathbf{k}, \mathbf{x})} \right)^{\frac{1}{2}} \left( 2\pi \sum_{\mathbf{k}} A(\mathbf{k}, \mathbf{x}) \right)^{\frac{1}{2}} \quad (\text{G.47})$$

$$\frac{1}{2\pi} = N \quad (\text{G.48})$$

whereupon, the final form for the probability density distribution of the local membrane separation distance is given by

$$P(Z, \mathbf{x}, t) = \left( \frac{1}{2\pi \sum_{\mathbf{k}} A(\mathbf{k}, \mathbf{x})} \right)^{\frac{1}{2}} e^{-\frac{Z^2}{2\sum_{\mathbf{k}} A(\mathbf{k}, \mathbf{x})}} . \quad (\text{G.49})$$

# Bibliography

- [1] Abramowitz, M. and Stegun, I. A. (1972). Handbook of mathematical functions with formulas, graphs, and mathematical tables. Eds(Abramowitz, Stegun), Washington DC
- [2] Allenspach, E. J., Cullinan, P., Tong, J., Tang, Q., Tesciuba, A. G., Cannon, J. L., Takahashi, S. M., Morgan, R., Burkhardt, J. K. & Sperling, A. I. (2001). ERM-dependent movement of CD43 defines a novel protein complex distal to the immunological synapse. *Immunity*, 15, 739-750.
- [3] Barabasi, A.-L. & Stanley, H. E. (1995). Fractal Concepts In Surface Growth. Cambridge University Press: Cambridge.
- [4] Barclay, A. N., Brown, M. H., Law, S. K. A., McKnight, A. J., Tomlinson, M. G., & van der Merwe, P. A. (1997). *The Leucocyte Antigen Factsbook. 2nd ed. Factsbook Series.* London: Academic Press Ltd.
- [5] Bayly, P. V. and Wilson, K. S. (2014). Equations of Interdoublet Separation during Flagella Motion Reveal Mechanisms of Wave Propagation and Instability. *Biophysical Journal*, 107, 1756-1772. doi: 10.1016/j.bpj.2014.07.064
- [6] Beemiller, P., Jacobelli, J., & Krummel, M. F. (2012) Integration of the movement of signalling microclusters with cellular motility in immunological synapses. *Nature Immunology*, 13, 787-795. doi:10.1038/ni.2364
- [7] Bell, G. I. (1978). Models of specific adhesion of cells to cells. *Science*, 200, 618-627.
- [8] Bell, G. I., Dembo, M., & Bongrand, P. (1984). Cell Adhesion. Competition Between Nonspecific Repulsion and Specific Bonding. *Biophysical Journal*, 45, 1051-1064.
- [9] Bhakta, N. R., Oh, D. Y., & Lewis, R. S. (2005). Calcium oscillations regulate thymocyte motility during positive selection in the three-dimensional thymic environment. *Nature Immunology*, 6, 143-151. doi:10.1038/ni1161
- [10] Bray, A. J., Majumdar, S. N., & Schehr, G. (2013). Persistence and First-Passage Properties in Non-Equilibrium Systems. *Advances in Physics*, 62(3), 225-361. doi: 10.1080/00018732.2013.803819

- [11] Brossard, C., Feuillet, V., Schmitt, A., Randriamampita, C., Romao, M., Raposo, G., & Trautmann, A. (2005). Multifocal structure of the T cell - dendritic cell synapse. *European Journal of Immunology*, *35*, 1741-1753.
- [12] Bunnell, S. C., Hong, D. I., Kardon, J. R., Yamasuki, T., McGlade, C. J., Barr, V. A., & Samelson, L. E. (2002). T cell receptor ligation induces the formation of dynamically regulated signalling assemblies. *Journal of Cellular Biology*, *158*, 1263-1275.
- [13] Bunnell, S. C., Singer, A. L., Hong, D. I., Jaque, B. H., Jordan, M. S., Seminario, M. C., Barr, V. A., Koretzky, G. A., & Samelson, L. E. (2006). Persistence of Cooperatively Stabilized Signaling Clusters Drives T-Cell Activation. *Molecular and Cellular Biology*, *26*(19), 7155-7166. doi: 10.1128/MCB.00507-06
- [14] Bunnell, S. C. (2010). Multiple Microclusters: Diverse Compartments Within the Immune Synapse. *Immunological Synapse*, Eds(Saito, Batista), Springer: London
- [15] Burroughs, N. J. & Wülfing, C. (2002). Differential Segregation in a Cell-Cell Contact Interface: The Dynamics of the Immunological Synapse. *Biophysical Journal*, *83*, 1784-1796. doi: 10.1016/S0006-3495(02)73944-1
- [16] Burroughs, N. J., Lazic, Z., & van der Merwe, P. A. (2006). Ligand Detection and Discrimination by Spatial Relocalization: A Kinase-Phosphatase Segregation Model of TCR Activation. *Biophysical Journal*, *91*, 1619-1629. doi: 10.1529/biophysj.105.080044
- [17] Burroughs, N. J. & van der Merwe, P. A. (2007). Stochasticity and spatial heterogeneity in T-cell activation. *Immunological Reviews*, *216*, 69-80.
- [18] Burroughs, N. J., Köhler, K., Miloserdov, V., Dustin, M. L., van der Merwe, P. A., & Davis, D. M. (2011). Boltzmann Energy-based Image Analysis Demonstrates that Extracellular Domain Size Differences Explain Protein Segregation at Immune Synapses. *PLoS Computational Biology*, *7*(8), e1002076. doi: 10.1371/journal.pcbi.1002076
- [19] Bush, D. R. & Chattopadhyay, A. K. (2014). Contact time periods in immunological synapse. *Physical Review E*, *90* (4), 042706. doi: 10.1103/PhysRevE.90.042706
- [20] Bush, D. R. & Chattopadhyay, A. K. (2015). Temporal dynamics in immunological synapse: Role of thermal fluctuations in signaling. *Physical Review E*, *92*, 012706. doi: 10.1103/PhysRevE.92.012706.
- [21] Bush, D. R. & Chattopadhyay, A. K. (2016). Asymptotic analysis of the immunological synapse dynamics: A saddle point method based approach. *Manuscript under preparation*.

- [22] Campi, G., Varma, R., & Dustin, M. L. (2005). Actin and agonist MHC-peptide complex-dependent T cell receptor microclusters as scaffolds for signaling. *The Journal of Experimental Medicine*, *202*(8), 1031-1036. doi: 10.1084/jem.20051182
- [23] Cannon, J. L., Labno, C. M., Bosco, G., Seth, A., McGavin, M. H. K., Siminovitch, K. A., Rosen, M. K., & Burkhardt, J. K. (2001). WASp Recruitment to the T Cell:APC Contact Site Occurs Independently of Cdc42 Activation. *Immunity*, *15* 249-259.
- [24] Čemerski, S., Das, J., Giurisato, E., Markiewicz, M. A., Allen, P. M., Chakraborty, A. K., & Shaw, A. S. (2008). The Balance between T Cell Receptor Signaling and Degradation at the Center of the Immunological Synapse Is Determined by Antigen Quality. *Immunity*, *29*(3), 414-422. doi: 10.1016/j.immuni.2008.06.014
- [25] Chakraborty, D. & Bhattacharjee, J. K. (2007). Finite-Size Effect in Persistence in Random Walk. *Physical Review E*, *75*(1), 1 - 5. doi: 10.1103/PhysRevE.75.011111
- [26] Chan, C., George, A. J. T., & Stark, J. (2001). Cooperative enhancement of specificity in a lattice of T cell receptors. *PNAS*, *98* (10), 5758-5763 doi: 10.1073/pnas.101113698
- [27] Chan, C., Stark, J., & George, A. J. T. (2004). Feedback control of T-cell receptor activation. *Proc. R. Soc. Lond. B*, *271*, 931-939 doi: 10.1098/rspb.2003.2587
- [28] Chattopadhyay, A. K. & Burroughs, N. J. (2007). Close contact fluctuations: The seeding of signalling domains in the immunological synapse. *European Physics Letters*, *77*, 48003. doi: 10.1209/0295-5075/77/48003
- [29] Chattopadhyay, A. K. (2011). Role of fluctuations in membrane models: thermal versus non-thermal. *European Physics Letters*, *84*, 03219. Retrieved from [www.arxiv.org](http://www.arxiv.org)
- [30] Chiam, K.-H. (2007). Oscillations in intracellular signaling cascades. *Physical Review E*, *75*, 061901 (1-7) doi: 10.1103/PhysRevE.75.061901
- [31] Choudhuri K., Llodrá, J., Roth, E. W., Tsai, J., Gordo, S., Wucherpfennig, K. W., Kam, L. C., Stokes, D. L., & Dustin, M. L. (2014). Polarized release of T-cell-receptor-enriched microvesicles at the immunological synapse. *Nature*, *507*, 118-123. doi: 10.1038/nature12951
- [32] Cordoba, S.-P., Choudhuri, K., Zhang, H., Bridge, M., Basat, A. B., Dustin, M. L., & van der Merwe, P. A. (2013). The large ectodomains of CD45 and CD148 regulate their segregation from and inhibition of ligated T-cell receptor. *Blood*, *121*(21), 4295-4302. doi: 10.1182/blood-2012-07-442251

- [33] Cyster, J. G., Shotten, D. M., & Williams, A. F. (1991). The dimensions of the T lymphocyte glycoprotein leukosialin and identification of linear protein epitopes that can be modified by glycosylation. *EMBO Journal*, *10*(4), 893-902.
- [34] Davis, S. J. & van der Merwe, P. A. (1996). The structure and ligand interactions of CD2: implications for T-cell function. *Immunology Today*, *17*(4), 177-187.
- [35] Davis, S. J. & van der Merwe, P. A. (2006). The kinetic segregation model: TCR triggering and beyond. *Nature Immunology*, *7*(8), 803-809. doi: 10.1038/ni1369
- [36] Davis, S. J. & van der Merwe, P. A. (2011). Lck and the nature of the T cell receptor trigger. *Trends in Immunology*, *32*(1), 1-5. doi: 10.1016/j.it.2010.11.003
- [37] Day, C. L., Seth, N. P., Lucas, M., Appel, H., Gauthier, L., Lauer, G. M., Robbins, G. K., Szczepiorkowski, Z. M., Casson, D. R., Chung, R. T., Bell, S., Harcourt, G., Walker, B. D., Klenerman, P., & Wucherpfennig, K. W. (2003). Ex vivo analysis of human memory CD4 T cells specific for hepatitis C virus using MHC class II tetramers. *The Journal of Clinical Investigation*, *112*(6), 831-842. doi: 10.1172/JCI200318509
- [38] Delon, J., Bercovici, N., Liblau, R., & Trautmann, A. (1998). Imaging antigen recognition by naive CD4+ T cells: compulsory cytoskeletal alterations for the triggering of an intracellular calcium response. *European Journal of Immunology*, *28*, 716-729.
- [39] Delon, J., Kaibuchi, K., & Germain, R. N. (2001). Exclusion of CD43 from the Immunological Synapse is Mediated by Phosphorylation-Regulated Relocation of the Cytoskeletal Adapter Moesin. *Immunity*, *15*, 691-701.
- [40] Douglass, A. D. & Vale, R. D. (2005). Single-Molecule Microscopy Reveals Plasma Membrane Microdomains Created by Protein-Protein Networks that Exclude or Trap Signaling Molecules in T Cells. *Cell*, *121*, 937-950. doi: 10.1016/j.cell.2005.04.009
- [41] Dustin, M., Sanders, M. E., Shaw, S., & Springer, T. A. (1987). Purified Lymphocyte Function-Associated Antigen 3 Binds to CD2 and Mediates T Lymphocyte Adhesion. *The Journal of Experimental Medicine*, *165*, 677-692.
- [42] Dustin, M. L., Bromley, S. K., Kan, Z., Peterson, D. A., & Unanue, E. R. (1997). Antigen receptor engagement delivers a stop signal to migrating T lymphocytes. *Proceedings of the National Academy of Sciences*, *94*, 3909-3913.
- [43] Dustin, M. L., Olszowy, M. W., Holdorf, A. D., Li, J., Bromley, S., Desai, N.,...Shaw, A. S. (1998). A Novel Adaptor Protein Orchestrates Receptor Patterning and Cytoskeletal Polarity in T-cell Contacts. *Cell*, *94*, 667-677.

- [44] Dustin, M. L. (2008). T-cell activation through immunological synapses and kinapses. *Immunological Reviews*, 221, 77-89.
- [45] Edwards, S. F. & Wilkinson, D. R. (1982). The Surface Statistics of a Granular Aggregate. *Proceedings of the Royal Society of London. Series A, Mathematical and Physical Sciences*, 381 (1780), 17-31.
- [46] Falahati, R. & Leitenberg, D. (2008). Selective Regulation of TCR Signalling Pathways by the CD45 Protein Tyrosine Phosphatase during Thymocyte Development. *The Journal of Immunology*, 181, 6082-6091.
- [47] Favier, B., Burroughs, N. J., Wedderburn, L., & Valitutti, S. (2001) TCR dynamics on the surface of living T cells. *International Immunity*, 13(12), 1525-1532. doi: 10.1093/intimm/13.12.1525
- [48] Finco, T. S., Kadlecsek, T., Zhang, W., Samelson, L. E., & Weiss, A. (1998). LAT is required for TCR-mediated activation of PLC $\gamma$ 1 and the Ras pathway. *Immunity*, 9, 617-626
- [49] Freudenthal, P. S. & Steinman, R. M. (1990). The distinct surface of human blood dendritic cells, as observed after an improved isolation method. *Proc. Natl. Acad. Sci. USA*, 87, 7698-7702.
- [50] Grakoui, A., Bromley, S. K., Sumen, C., Davis, M. M., Shaw, A. S., Allen, P. M., & Dustin, M. L. (1999). The Immunological Synapse: A Molecular Machine Controlling T Cell Activation. *Science*, 285, 221-227.
- [51] Gunzer, M., Schäfer, A., Borgmann, S., Grabbe, S., Zänker, K. S., Bröcker, E.-B.,...Friedl, P. (2000). Antigen Presentation in Extracellular Matrix: Interactions of T Cells with Dendritic Cells Are Dynamic, Short Lived, and Sequential. *Immunity*, 13, 323-332.
- [52] Heinrich, R., Neel, B. G., & Rapoport, T. A. (2002). Mathematical Models of Protein Kinase Signal Transduction. *Molecular Cell*, 9, 957-970.
- [53] Henrickson, S. E., Mempel, T. R., Mazo, I. B., Liu, B., Artyomov, M. N., Zheng, H., Peixoto, A., Flynn, M., Senman, B., Junt, T., Wong, H. C., Chakraborty, A. K., & von Andrian, U. H. (2008). T cell sensing of antigen dose governs interactive behavior with dendritic cells and sets a threshold for T cell activation. *Nature Immunology*, 9(3), 282-291. doi: 10.1038/ni1559
- [54] Hilfinger, A., Chattopadhyay, A. K., & Jülicher, F. (2009) Nonlinear dynamics of cilia and flagella. *Physical Review E*, 79, 051918. doi: 10.1103/PhysRevE.79.051918

- [55] Hogan, P. G., Chen, L., Nardone, J., & Rao, A. (2003). Transcriptional regulation by calcium, calcineurin, and NFAT. *Genes & Development*, *17*, 2205-2232. doi:10.1101/gad.1102703
- [56] Hori, Y., Raychaudhuri, S., & Chakraborty, A. K. (2002). Analysis of pattern formation and phase separation in the immunological synapse. *Journal of Chemical Physics*, *117*(20), 9491-9501. doi: 10.1063/1.1512642
- [57] Houtman, J. C. D., Houghtling, R. A., Barda-Saad, M., Todo, Y. & Samelson, L. E. (2005) Early Phosphorylation Kinetics of Proteins Involved in Proximal TCR-Mediated Signaling Pathways. *Journal of Immunology*, *175*(4), 2449-2458.
- [58] Huppa, J. B., Axmann, M., Mörtelmaier, M. A., Lillemeier, B. F., Newell, E. W., Brameshuber, M., ...Davis, M. M. (2010). TCR-peptide-MHC interactions in situ show accelerated kinetics and increased affinity. *Nature*, *463*, 963-967.
- [59] Huse, M., Klein, L. O., Girvin, A. T., Faraj, J. M., Li, Q.-J., Kuhns, M. S., & Davis, M. M. (2007). Spatial and Temporal Dynamics of T Cell receptor Signaling with a Photoactivatable Agonist. *Immunity*, *27*, 76-88. doi: 10.1016/j.immuni.2007.05.017
- [60] Ingulli, E., Mondino, A., Khoruts, A., & Jenkins, M. K. (1997). In Vivo Detection of Dendritic Cell Antigen Presentation to CD<sup>+</sup> T Cells. *The Journal of Experimental Medicine*, *185*(12), 2133-2141.
- [61] Johnson, K. G., Bromley, S. K., Dustin, M. L., & Thomas, M. L. (2000). A supramolecular basis for CD45 tyrosine phosphatase regulation in sustained T cell activation. *Proceedings of the National Academy of Sciences*, *97*(18), 10138-10143.
- [62] <sup>1</sup> Kaizuka, Y., Douglass, A. D., Vardhana, S., Dustin, M. L., & Vale, R. D. (2009) The coreceptor CD2 uses plasma membrane microdomains to transduce signals in T cells. *Journal of Cell Biology*, *185*(3), 521-534. doi:10.1083/jcb.200809136
- [63] Košmrlj, A., Kardar, M. & Chakraborty, A. K., (2013). Statistical Physics of T-Cell Development and Pathogen Specificity. *Ann. Rev. Cond. Mat. Phys*, *4*(1), 339-360. doi: 10.1146/annurev-conmatphys-030212-184325
- [64] Krug, j., Kallabis, H., Majumdar, S. N., Cornell, S. J., Bray, A. J., & Sire, C. (1997). Persistence exponents for fluctuating interfaces. *Physical Review E*, *56*(3), 2702-2712.
- [65] Krummel, M. F., Sjaastad, M. D., Wülfing, C., & Davis, M. M. (2000). Differential Clustering of CD4 and CD3 $\zeta$  During T Cell Recognition. *Science*, *289*, 1349-1352.

---

<sup>1</sup>Read

- [66] Kuhn, J. R. & Poenie, M. (2002). Dynamic Polarization of the Microtubule Cytoskeleton during CTL-Mediated Killing. *Immunity*, *16*, 111-121.
- [67] Lee, K. H., Holdorf, A. D., Dustin, M. L., Chan, A. C., Allen, P. M., & Shaw, A. S. (2002). T cell Receptor Signaling Precedes Immunological Synapse Formation. *Science*, *295*, 1539-1542.
- [68] Lee, K. H., Dinner, A. R., Tu, C., Campi, G., Raychaudhuri, S., Varma, R., ...Shaw, A. S. (2003). The Immunological Synapse Balances T Cell Receptor Signaling and Degradation. *Science*, *302*, 1212-1222.
- [69] Lee, S.-J. E., Hori, Y., Groves, J. T., Dustin, M. L., & Chakraborty, A. K. (2002). Correlation of a dynamic model for immunological synapse formation with effector functions: two pathways to synapse formation. *Trends in Immunology*, *23*(10), 492-499.
- [70] Lewis, R. S. (2003). Calcium oscillations in T-cells: mechanisms and consequences for gene expression. *Biochem. Soc. Trans.*, *31*, 925-929.
- [71] Lipsky, P. E. & Rosenthal, A. S. (1975). Macrophage-Lymphocyte Interaction. *The Journal of Experimental Medicine*, *141*, 138.
- [72] Littman, D. R. (Ed.) (1996). *The CD4 Molecule. Roles in T Lymphocytes and HIV Disease..* Springer: London.
- [73] Lollo, B. A., Chan, K. W. H., Hanson, E. M., Moy, V. T., & Brian, A. A. (1993). Direct Evidence for Two Affinity States for Lymphocyte Function-associated Antigen 1 on Activated T Cells. *The Journal of Biological Chemistry*, *268*(29), 21693-21700
- [74] Macián, F., López-Rodríguez, C., & Rao, A. (2001). Partners in transcription: NFAT and AP-1. *Oncogene*, *20*, 2476-2489.
- [75] Majumdar, S. N. & Sire, C. (1996). Survival probability of a Gaussian non-Markovian process: Application to the T=0 dynamics of the Ising model. *Physical Review Letters*, *77*(8), 1420-1423. doi: 10.1103/PhysRevLett.77.1420
- [76] Majumdar, S. N., Sire, C., Bray, A. J., & Cornell, S. J. (1996). Nontrivial Exponent for Simple Diffusion. *Physical Review Letters*, *77*(14), 2867-2870.
- [77] Manjunath, N., Correa, M., Ardman, M., & Ardman, B. (1995). Negative regulation of T-cell adhesion and activation by CD43. *Nature*, *377*, 535-538.
- [78] Manz, B. N., Jackson, B. L., Petit, R. S., Dustin, M. L., & Groves, J. (2011). T-cell triggering thresholds are modulated by the number of antigen within individual T-cell

- receptor clusters. *Proceedings of the National Academy of Sciences*, 108(22), 9089-9094.  
doi: 10.1073/pnas.1018771108
- [79] Matsui, K., Boniface, J. J., Steffner, P., Reay, P., & Davis, M. M. (1994). Kinetics of T-cell receptor binding to peptide/I-E<sup>k</sup> complexes: Correlation of the dissociation rate with T-cell responsiveness. *Proc. Natl. Acad. Sci. USA*, 91, 12862-12866.
- [80] McKeithan, T. W. (1995). Kinetic proofreading in T-cell receptor signal transduction. *Proc. Natl. Acad. Sci. USA*, 92, 5042-5046.
- [81] Mempel, T. R., Henrickson, S. E., & von Andrian, U. H. (2004). T-cell priming by dendritic cells in lymph nodes occurs in three distinct phases. *Nature*, 427, 154-159.
- [82] Meuer, S., Hussey, R. E., Fabbi, M., Fox, D., Acuto, O., Fitzgerald, K. A., Hodgdon, J. C., Protentis, J. P., Schlossman, S. F., & Reinherz, E. L. (1984). An alternative pathway of T-cell activation: A functional role for the 50 kd T11 sheep erythrocyte receptor protein. *Cell*, 36(4), 897-906. doi: 10.1016/0092-8674(84)90039-4
- [83] Miller, J., Knorr, R., Ferrone, M., Houdei, R., Carron, C. P., & Dustin, M. L. (1995). Intercellular Adhesion Molecule-1 Dimerization and Its Consequences for Adhesion Mediated by Lymphocyte Function Associated-1. *The Journal of Experimental Medicine*, 182, 1231-1241.
- [84] Monks, C. R. F., Frieberg, B. A., Kupfer, H., Sciaky, N., & Kupfer, A. (1998). Three-dimensional segregation of supramolecular activation clusters in T cells. *Nature*, 395, 82-86.
- [85] Mossman, K. D., Campi, G., Groves, J. T. & Dustin, M. L. (2005). Altered TCR Signalling from Geometrically Repatterned Immunological Synapses. *Science*, 310(5751), 1191-1193. doi: 10.1126/science.1119238
- [86] Murphy, K., Travers, P. & Walport, M. (2008). *Janeways: Immunobiology* (7th ed.). London: Garland Science, Taylor & Francis Group, LLC
- [87] Murray, J. D. (1974). *Asymptotic Analysis* Oxford University Press
- [88] Nabavi, N., Freeman, G. J., Gault, A., Godfrey, D., Nadler, L. M. & Glimcher, L. H. (1992). Signalling through the MHC class II cytoplasmic domain is required for antigen presentation and induces B7 expression. *Nature*, 360, 266-268. doi: 10.1038/360266a0
- [89] Nika, K., Soldani, C., Salek, M., Paster, W., Gray, A., Etzensperger, R., Fugger, L., Polzella, P., Cerundolo, V., Dushek, O., Höfer, T., Viola, A., & Acuto, O. (2010). Constitutively Active Lck Kinase in T Cells Drives Antigen Receptor Signal Transduction. *Immunity*, 32, 766-777. doi: 10.1016/j.immuni.2010.05.011

- [90] Norcross, M. A., Smith, R. T., & Shimizu, S. (1984). Regulation of TCGF Production in T Cells. II. Early Membrane Events After Anti-Thy-1 Binding by the TCGF-producing T Lymphoma EL-4 G-12. *The Journal of Immunology*, *132*(2), 833-838.
- [91] Northrop, J. P., Ho, S. N., Chen, L., Thomas, D. J., Timmerman, L. A., Nolan, G. P., Admon, A., & Crabtree, G. R. (1994). NF-AT components define a family of transcription factors targeted in T-cell activation. *Nature*, *369*, 497-502.
- [92] Poenie, M., Kuhn, J., & Combs, J. (2004). Real-time visualization of the cytoskeleton and effector functions in T cells. *Current Opinion in Cell Biology*, *16*, 428-438. doi: 10.1016/j.coi.2004.05.016
- [93] Poo, W. J., Conrad, L., & Janeway, C. A. Jr. (1988). Receptor-directed focusing of lymphokine release by helper T cells. *Nature*, *332*, 378-380. doi: 10.1038/332378a0
- [94] Press, W. H., Teukolsky, S. A., Vetterling, W. T., & Flannery, B. P. (2005) Numerical Recipes in C++. The Art of Scientific Computing. Second Edition. Cambridge University Press: Cambridge.
- [95] Qi, S. Y., Groves, J. T., & Chakraborty, A. (2001). Synaptic pattern formation during cellular recognition. *PNAS: Proceedings of the National Academy of Sciences (USA)*, *98*(12), 6548-6553. doi: 10.1073/pnas.111536798
- [96] Qi, S., Krogsgaard, M., Davis, M. M., & Chakraborty, A. (2006). Molecular flexibility can influence the stimulatory ability of receptor-ligand interactions at cell-cell junctions. *PNAS: Proceedings of the National Academy of Sciences (USA)*, *103*(12), 4416-4421. doi: 10.1073/pnas.0510991103
- [97] Raychaudhuri, S., Chakraborty, A. K., & Kardar, M. (2003). Effective Membrane Model of the Immunological Synapse. *Physical Review Letters*, *91*(20), 208101. doi: 10.1103/PhysRevLett.91.208101
- [98] Rice, S. O. (1944). Mathematical analysis of random noise. *Bell Systems Technical Journal*, *23*, 282-332.
- [99] Rice, S. O. (1945). Mathematical analysis of random noise. *Bell Systems Technical Journal*, *24*, 46-156.
- [100] Risken, H. (1989). *The Fokker-Planck Equation* (2nd ed.). London: Springer-Verlag
- [101] Rosenstein, Y., Park, J. K., Hahn, W. C., Rosen, F. S., Bierer, B. E., & Burakoff, S. J. (1991). CD43, a molecule defective in Wiskott-Aldrich syndrome, binds ICAM-1. *Nature*, *354*, 233-235.

- [102] Sabatos, C. A., Doh, J., Chakravarti, S., Friedman, R. S., Pandurang, P. G., Tooley, A. J. & Krummel, M. F. (2008). A Synaptic Basis for Paracrine Interleukin-2 Signaling during Homotypic T Cell Interaction. *Immunity*, *29*(2), 238-248. doi: 10.1016/j.immuni.2008.05.017
- [103] Safran, S. A. (2003). *Frontiers in Physics: Statistical Thermodynamics of Surfaces, Interfaces, and Membranes*. Westview Press.
- [104] Saito, T. & Yokosuka, T. (2006). Immunological synapse and microclusters: the site for recognition and activation of T cells. *Current Opinion in Immunology*, *18*, 305-313. doi: 10.1016/j.coi.2006.03.014
- [105] Saito, T. & Batista, F. D. (2010). *Current Topics in Microbiology and Immunology: Immunological Synapse*. Eds(Saito, Batista), Springer: London
- [106] Savage, N. D. L., Kimzey, S. L., Bromley, S. K., Johnson, K. G., Dustin, M. L., & Green, J. M. (2002). Polar Redistribution of the Sialoglycoprotein CD43: Implications for T Cell Function. *The Journal of Immunology*, *168*, 3740-3746.
- [107] Schwabl, F (2006). *Statistical Mechanics*, 2nd Edition. *Springer*
- [108] Sechi, A. S. & Wehland, J. (2004). Interplay between TCR signalling and actin cytoskeleton dynamics. *Trends in Immunology*, *25*(5), 257-265.
- [109] Selvaraj, P., Plunkett, M. L., Dustin, M., Sanders, M. E., Shaw, S., & Springer, T. A. (1987). The T lymphocyte glycoprotein CD2 binds the cell surface ligand LFA-3. *Nature*, *326*, 400-403.
- [110] Shen, K., Thomas, V. K., Dustin, M. L., & Kam, L. C. (2008). Micropatterning of costimulatory ligands enhances CD4<sup>+</sup> T cell function. *Proceedings of the National Academy of Sciences*, *105*(22), 7791-7796. doi: 10.1073/pnas.0710295105
- [111] Shiroo, M., Goff, L., Biffen, M., Shivnan, E., & Alexander, D. (1992). CD45 tyrosine phosphatase-activated p59<sup>lyn</sup> couples the T cell antigen receptor to pathways of diacylglycerol production, protein kinase C activation and calcium influx. *EMBO Journal*, *11*(12), 4887-4897.
- [112] Sims T. N., Soos, T. J., Xenias, H. S., Dubin-Thaler, B., Hofman, J. M., Waite, J. C., Cameron, T. O., Thomas, V. K., Varma, R., Wiggins, C. H., Sheetz, M. P., Littman, D. R., & Dustin, M. L. (2007). Opposing effects of PKC- $\theta$  and WASp on symmetry breaking and relocation of the immunological synapse. *Cell*, *129*, 773-785. doi: 10.1016/j.cell.2007.03.037

- [113] Sire, C. (2007). Probability Distribution of the Maximum of a Smooth Temporal Signal. *Physical Review Letters*, *98*(2). doi: 10.1103/PhysRevLett.98.020601.
- [114] Sperling, A. I., Sedy, J. R., Manjunath, N., Kupfer, A., Ardman, B., & Burkhardt, J. K. (1998). TCR signaling induces selective exclusion of CD43 from the T cell-APC contact site. *The Journal of Immunology*, *161*, 6459-6462.
- [115] Springer, T. A., Dustin, M. L., Kishimoto, T. K., & Marlin, S. D. (1987). THE LYMPHOCYTE FUNCTION-ASSOCIATED LFA-1, CD2, and LFA-3 MOLECULES: Cell Adhesion Receptors of the Immune System. *Annual Review Immunology*, *5*, 223-252.
- [116] Springer, T. A. & Dustin, M. L. (2012). Integrin inside-out signaling and the immunological synapse. *Current Opinion in Cell Biology*, *24*, 107-115. doi: 10.1016/j.ceb.2011.10.004
- [117] Stinchcombe, J. C., Bossi, G., Booth, S., & Griffiths, G. M. (2001). The Immunological Synapse of CTL Contains a Secretory Domain and Membrane Bridges. *Immunity*, *15*, 751-761.
- [118] Stoll, S., Delon, J., Brotz, T. M., & Germain, R. N. (2002). Dynamic imaging of T-cell-dendritic cell interactions in lymph nodes. *Science*, *296*, 1873-1876.
- [119] Stone, J. D. & Kranz, D. M. (2013). Role of T cell receptor affinity in the efficacy and specificity of adoptive T cell therapies. *Frontiers in Immunology*, *4*(244). doi: 10.3389/fimmu.2013.00244
- [120] Taloni, A., Checkkin, A., & Klafter, J. (2012). Generalized Elastic Model: thermal vs non-thermal initial conditions. Universal scaling, roughening, ageing and ergodicity. *European Physics Letters*, *97*, 30001. Retrieved from <http://www.arXiv.org:1203.3297v2>
- [121] Tominaga, Y., Kita, Y., Satoh, A., Asai, S., Kato, K., Ishikawa, K., Horiuchi, T. & Takashi, T. (1998). Affinity and kinetic analysis of the molecular interaction of ICAM-1 and Leukocyte Function-Associated Antigen-1. *Journal of Immunology*, *161*, 4016-4022.
- [122] Valitutti, S., Müller, S., Cella, M., Padovan, E., & Lanzavecchia, A. (1995). Serial triggering of many T-cell receptors by a few peptide-MHC complexes. *Nature*, *375*, 148-151.
- [123] Valitutti, S. & Lanzavecchia, A. (1997). Serial triggering of TCRs: a basis for the sensitivity and specificity of antigen recognition. *Immunology Today*, *18*(6), 299-304.
- [124] van der Merwe, P. A., Bodian, D. L., Daenke, S., Linsley, P., & Davis, S. J. (1997). CD80 (B7-1) Binds Both CD28 and CTLA-4 with Low Affinity and Very Fast Kinetics. *The Journal of Experimental Medicine*, *185*(3), 393-403.

- [125] van Kampen, N. G. (1987). *Stochastic Processes in Chemistry and Physics*. Amsterdam:North-Holland Personal Library
- [126] Varma, R., Campi, G., Yokosuka, T., Saito, T., & Dustin, M. L. (2006). T Cell Receptor-Proximal Signals Are Sustained in Peripheral Microclusters and Terminated in the Central Supramolecular Activation Cluster. *Immunity*, *25*, 117-127. doi: 10.1016/j.immunity.2006.04.010
- [127] Viola & Lanzavecchia (1996). T cell activation determined by T cell receptor number and tunable thresholds. *Science*, *273*, 104-106
- [128] Waldmann, T. A. (1989). The Multi-Subunit Interleukin-2 Receptor. *Annual Review of Biochemistry*, *58*, 875-911.
- [129] Watson, N. G. (19188). The harmonic functions associated with the parabolic cylinder. *Proceedings of the London Mathematical Society*, *2* (17), 116148. doi:10.1112/plms/s2-17.1.116
- [130] Wedagedera, J. R. & Burroughs, N. J. (2006). T-Cell Activation: A Queuing Theory Analysis at Low Agonist Density. *Biophysical Journal*, *91*, 1604-1618. doi: 10.1529/biophysj.105.066001
- [131] Weiss, A., Wiskocil, R. L. & Stobo, J. D. (1984). The role of T3 Surface Molecules in the Activation of Human T Cells: A Two-Stimulus Requirement of IL 2 Production Reflects Events Occuring at a Pre-Translational Level. *The Journal of Immunology*, *133*(1), 123-128.
- [132] Wild, M. K., Cambiaggi, A., Brown, M. H., Davies, E. A., Ohno, H., Saito, T., & van der Merwe, A. P. (1999). Dependence of T Cell Antigen Recognition on the Dimensions of an Accessory Receptor-Ligand Complex. *The Journal of Experimental Medicine*, *190*(1), 31-41.
- [133] Wülfing, C., Rabinowitz, J. D., Beeson, C., Sjaastad, M. D., McConnell, H. M., & Davis, M. M. (1997). Kinetics and Extent of T Cell Activation as Measured with Calcium Signal. *The Journal of Experimental Medicine*, *185*(10), 1815-1825.
- [134] Wülfing, C. & Davis, M. M. (1998). A receptor/cytoskeletal movement triggered by costimulation during T cell activation. *Science*, *282*, 2266-2269.
- [135] Wyer, J. R., Wilcox, B. E., Gao, G. F., Gerth, U. C., Davis, S. J., Bell, J. I., van der Merwe, P. A., & Jakobsen, B. K. (1999). T Cell Receptor and Coreceptor CD8 $\alpha\alpha$  Bind Peptide-MHC Independently and with Distinct Kinetics. *Immunity*, *10*, 219-225.

- [136] Yokosuka, T., Sakata-Sogawa, K., Kobayashi, W., Hiroshima, M., Hashimoto-Tane, A., Tokunaga, M., Dustin, M. L., & Saito, T. (2005). Newly generated T cell receptor microclusters initiate and sustain T cell activation activation by recruitment of Zap70 and SLP-76. *Nature Immunology*, *6*(12), 1253-1262. doi: 10.1038/ni1272
- [137] Yokosuka, T., Kobayashi, W., Sakata-Sogawa, K., Takamatsu, M., Hashimoto-Tane, Dustin, M. L., A., Tokunaga, M., & Saito, T. (2008). Spatiotemporal Regulation of T Cell Costimulation by TCR-CD28 Microclusters and Protein Kinase C  $\theta$  Translocation. *Immunity*, *29*, 589-601. doi: 10.1016/j.immuni.2008.08.011
- [138] Zheng, H., Jin, B., Henrickson, S. E., Perelson, A. S., von Adrian, U. H., & Chakraborty, A. K. (2008). How Antigen Quantity and Quality Determine T-Cell Decisions in Lymphoid Tissue. *Molecular and Cellular Biology*, *28*(12), 4040-4051. doi: 10.1128/MCB.00136-08